

2005

The impact of iron on the macrosegregation of oxygen in Ti-6Al-4V

Sarah Lynn Knisley
University of Dayton

Follow this and additional works at: https://ecommons.udayton.edu/graduate_theses

Recommended Citation

Knisley, Sarah Lynn, "The impact of iron on the macrosegregation of oxygen in Ti-6Al-4V" (2005). *Graduate Theses and Dissertations*. 3971.
https://ecommons.udayton.edu/graduate_theses/3971

This Thesis is brought to you for free and open access by the Theses and Dissertations at eCommons. It has been accepted for inclusion in Graduate Theses and Dissertations by an authorized administrator of eCommons. For more information, please contact mschlangen1@udayton.edu, ecommons@udayton.edu.

**THE IMPACT OF IRON ON THE
MACROSEGREGATION OF OXYGEN IN Ti-6Al-4V**

Thesis

Submitted to

**The School of Engineering of the
UNIVERSITY OF DAYTON**

in Partial Fulfillment of the Requirements for

The Degree

Master of Chemical Engineering

by

Sarah Lynn Knisley

UNIVERSITY OF DAYTON

Dayton, Ohio

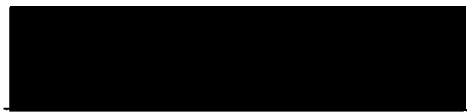
December 2005

THE IMPACT OF IRON ON THE MACROSEGREGATION OF OXYGEN IN TI-6AL-4V

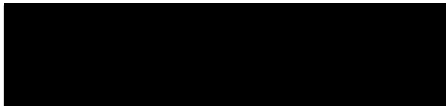
APPROVED BY:



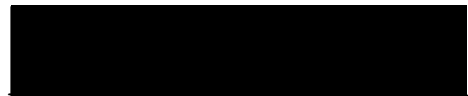
Tony E. Saliba, Ph.D.
Advisory Committee Chairman
Professor and Chairman, Chemical
and Materials Engineering Department



Pamela A. Kobryn, Ph.D.
Committee Member
Materials Engineer,
Acquisition Systems Support Branch
Materials & Manufacturing Directorate
Air Force Research Laboratory



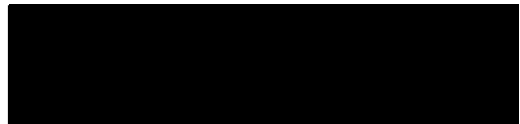
S. Lee Semiatin, Ph.D.
Committee Member
Senior Scientist,
Materials Processing/Processing Science
Materials & Manufacturing Directorate
Air Force Research Laboratory



Andrey A. Voevodin, Ph.D.
Committee Member
Senior Materials Engineer,
Nonstructural Materials Branch
Materials & Manufacturing Directorate
Air Force Research Laboratory



Donald L. Moon, Ph.D.
Associate Dean
Graduate Engineering Programs & Research
School of Engineering



Joseph E. Saliba, Ph.D., P.E.
Dean, School of Engineering

ABSTRACT

**Title: THE IMPACT OF IRON ON THE MACROSEGREGATION OF OXYGEN IN
Ti-6Al-4V4V**

**Knisley, Sarah, Lynn
University of Dayton**

Advisor: Dr. Tony Saliba

The effect of iron content on the macrosegregation of oxygen in Ti-6Al-4V castings was investigated. The focus was on three main areas; characterization, production-scale investigation, and segregation modeling. For the characterization portion, differential thermal analysis was utilized to determine the freezing range of Ti-6Al-4V alloys having different iron and oxygen contents. Scanning electron microscopy, energy-dispersive spectrometry, wavelength-dispersive spectrometry, and microindentation hardness testing were completed to confirm that specimens were not contaminated during thermal analysis. Ti-6Al-4V ingot slabs and small-scale ingots were examined in the production-scale analysis. Wet chemical analysis was performed on slabs from the center of a vacuum-arc remelted ingot to determine the chemical distribution of various solutes across the ingot radius. Chemical distribution of several solutes was investigated in small-scale induction-skull melted ingots via electron probe microanalysis. Segregation modeling was completed using two simple microsegregation models, the lever rule and Scheil equation, and several limiting cases of the local solute redistribution equation, a macrosegregation model.

Results indicated that the freezing range was different for alloys of different iron and oxygen contents. Definitive trends in chemical distribution could not be established

for the ingot slabs or small-scale ingots. Segregation modeling revealed that accurate values of the partition coefficients and the length of the mushy zone were critical for quantifying segregation of titanium ingots.

ACKNOWLEDGEMENTS

I would like to sincerely thank my advisors, Pam Kobryn and Lee Semiatin, for their guidance. I would like to thank the other members of my committee, Tony Saliba and Andrey Voevodin for reviewing my thesis. I am very grateful for the assistance of John Perepezko, Jeff Werner, Jeff Waters, and Joe Hamman with thermal analysis measurements and training at the University of Wisconsin-Madison. I would like to thank Oscar Yu of RMI Titanium for providing the button melts and technical advice. I would like to thank Austin Chang and CompuTherm, LLC for providing the thermodynamic calculations. I would like to thank Glessna LeBaron for her invaluable assistance through all stages of this research. I would like to thank Doug Barker for the financial backing for my research. I would like to thank Mike Glavicic, Jon Miller, Dave Mahaffey, and Don Weaver for helpful comments. Finally, I wish to thank my family and friends for their love and support.

TABLE OF CONTENTS

<u>Title</u>	<u>Page</u>
ABSTRACT.....	iii
ACKNOWLEDGEMENTS.....	v
LIST OF FIGURES.....	xi
LIST OF TABLES.....	xviii
LIST OF SYMBOLS.....	xix
CHAPTER	
1. INTRODUCTION.....	1
2. BACKGROUND INFORMATION.....	5
2.1 Titanium Alloys.....	5
2.2 Casting of Titanium Alloys.....	7
2.2.1 Ingot Casting.....	7
2.2.2 Other Casting Methods.....	8
2.3 Solidification Theory.....	8
2.4 Types of Segregation.....	11
2.5 Segregation Modeling.....	12
2.5.1 Microsegregation Models.....	12
2.5.2 Macrosegregation Models.....	18
2.5.2.1 Binary Alloy Solidification Models.....	19
2.5.2.2 Extension to Multi-Component Alloys.....	22
2.5.2.3 Coupled Micro-Macro Models.....	24
2.5.2.4 State of the Art.....	26
2.6 Phase Equilibria.....	27
2.7 Pandat™ Software for Thermodynamic Calculations.....	29

2.8 Experimental Techniques for Investigation of Segregation.....	30
2.8.1 Thermal Analysis.....	30
2.8.1.1 Interpretation of Thermal Analysis Curves	34
2.8.2 Electron Probe Microanalysis	36
2.8.3 Microindentation Hardness Measurements.....	36
2.9 Research Issues/Objectives.....	36
 3. MATERIALS AND EXPERIMENTAL PROCEDURES	 39
3.1 Button Melts and Baseline Material.....	39
3.1.1 Starting Material	40
3.1.2 Wet Chemical Analysis.....	40
3.1.3 Differential Thermal Analysis.....	40
3.1.4 Metallographic Preparation.....	42
3.1.5 Scanning Electron Microscopy	42
3.1.6 Energy-Dispersive Spectrometry	42
3.1.7 Electron Probe Microanalysis	42
3.1.8 Microindentation Hardness Measurements.....	43
3.1.9 Thermodynamic Modeling	43
3.2 Production-Scale Ingots.....	43
3.2.1 Material and Sectioning.....	44
3.2.2 Wet Chemical Analysis.....	44
3.3 Small-Scale Ingots.....	44
3.3.1 Material and Sectioning.....	44
3.3.2 Metallographic Preparation.....	45
3.3.3 Electron Probe Microanalysis	45
 4. CHARACTERIZATION RESULTS AND DISCUSSION	 46
4.1 Wet Chemical Analysis	46
4.2 Differential Thermal Analysis	47
4.3 Scanning Electron Microscopy.....	51
4.4 Energy-Dispersive Spectrometry.....	52
4.5 Electron Probe Microanalysis.....	52

4.6 Microindentation Hardness Measurements	52
4.7 Thermodynamic Modeling.....	53
4.7.1 Initial Calculations	53
4.7.2 Effect of Aluminum Evaporative Losses on Freezing Range Calculations.....	55
4.8 Conclusions	56
 5. INGOT INVESTIGATION RESULTS	 57
5.1 Wet Chemical Analysis	57
5.2 Ingot Solute Distribution Plots.....	59
5.2.1 Aluminum Distribution.....	59
5.2.2 Vanadium Distribution	62
5.2.3 Iron Distribution	64
5.2.4 Oxygen Distribution.....	66
5.2.5 Comparison of Iron and Oxygen Distribution	68
5.3 Small-Scale Ingot Solute Distribution	68
5.3.1 Aluminum Distribution.....	68
5.3.2 Vanadium Distribution	70
5.3.3 Iron Distribution	71
5.4 Conclusions	73
 6. SEGREGATION MODELING	 74
6.1 Procedures	74
6.1.1 Equations and Assumptions.....	74
6.1.1.1 Microsegregation Models.....	74
6.1.1.2 Macrosegregation Models.....	75
6.1.2 Thermophysical Data	77
6.1.2.1 Partition Coefficients.....	77
6.1.2.2 Solidification Shrinkage.....	78
6.1.2.3 Additional Parameters	78
6.1.3 Sensitivity Analysis.....	79
6.1.4 Segregation Calculations for Ingots.....	80

6.2 Results of Sensitivity Analysis.....	81
6.2.1 Partition Coefficients	81
6.2.2 Primary Dendrite Arm Spacing	84
6.2.3 Pressure Drop across the Mushy Zone	86
6.2.4 Mushy Zone Length.....	89
6.2.5 Temperature Gradients and Cooling Rates	92
6.3 Results of Segregation Calculations for Ingots.....	95
6.4 Conclusions	100
 7. CONCLUSIONS AND FUTURE WORK	 101
7.1 Conclusions	101
7.2 Future Work.....	102
 APPENDICES	 103
A. Casting of Titanium Alloys.....	103
A.1 Ingot Casting	103
A.1.1 Vacuum Arc Remelting	103
A.1.2 Electron Beam Melting and Casting	105
A.1.3 Plasma Arc Melting	106
A.1.4 Induction Skull Melting	107
A.2 Investment Casting.....	109
A.3 Button Melting	110
B. Netzsch Instrument Model STA 409 CD.....	112
B.1 Instrument Overview.....	112
B.2 Operating Procedures	113
C. Example DTA Heating Scheme	115
D. Differential Thermal Analysis Plots.....	116
E. SEM Backscattered Electron Images	125
F. Electron Probe Microanalysis.....	136
G. Microindentation Hardness Measurements.....	137
H. Initial Thermodynamic Calculations.....	138
I. Segregation Modeling	139
J. Additional Sensitivity Analysis Plots.....	140

REFERENCES.....	145
VITA.....	150

LIST OF FIGURES

<u>Figure</u>	<u>Page</u>
1. Solidification sequence of ingots and large castings.	11
2. Equilibrium solidification, (a) binary phase diagram; (b) composition profile across the interface.	13
3. Segregation modeling using the Scheil equation with the assumptions of no solid diffusion and complete liquid diffusion. a) beginning of solidification, b) at temperature T^* , c) end of solidification d) binary phase diagram.....	16
4. Small volume element contained in the mushy zone.....	17
5. Small volume element contained in the mushy zone incorporating interdendritic fluid flow.....	20
6. Utilization of Gibbs energy curves to develop a phase diagram for a binary system.....	28
7. Schematic of a differential thermal analyzer.....	31
8. DTA trace for the melting of zinc in argon atmosphere, heated at a rate of $10^\circ\text{C}/\text{min}$	32
9. Schematic of a power-compensated differential scanning calorimeter.	33
10. Sample DTA trace upon heating.	34
11. Sample DTA trace upon cooling. The solid line indicates complete melting (at a temperature above the liquidus), and the dotted line indicates incomplete melting (at a temperature below the liquidus). The actual liquidus temperature falls between the two cooling curves.	35
12. Measured freezing range as a function of iron content for Ti-6Al-4V alloys having different concentrations of iron and oxygen.	48
13. Measured freezing range as a function of oxygen content for Ti-6Al-4V alloys having different concentrations of iron and oxygen.....	49
14. Solidus temperatures as functions of iron content for Ti-6Al-4V alloys having different concentrations of iron and oxygen.....	49

15.	Liquidus temperature as functions of iron content for Ti-6Al-4V alloys having different concentrations of iron and oxygen.	50
16.	Comparison of present and traditional methods of determining the freezing onset or liquidus as a function of iron content.....	51
17.	Comparison of measured and predicted freezing range as a function of iron content.	54
18.	Comparison of measured and predicted freezing range as a function of oxygen content.	54
19.	Aluminum radial distribution in Ti-6Al-4V ingot slab "A" as measured via wet chemical analysis.....	60
20.	Aluminum radial distribution in Ti-6Al-4V ingot slab "C" as measured via wet chemical analysis.....	61
21.	Aluminum radial distribution in Ti-6Al-4V ingot slab "E" as measured via wet chemical analysis.....	61
22.	Vanadium radial distribution in Ti-6Al-4V ingot slab "A" as measured via wet chemical analysis.....	62
23.	Vanadium radial distribution in Ti-6Al-4V ingot slab "C" as measured via wet chemical analysis.....	63
24.	Vanadium radial distribution in Ti-6Al-4V ingot slab "E" as measured via wet chemical analysis.....	63
25.	Iron radial distribution in Ti-6Al-4V ingot slab "A" as measured via wet chemical analysis.....	64
26.	Iron radial distribution in Ti-6Al-4V ingot slab "C" as measured via wet chemical analysis.....	65
27.	Iron radial distribution in Ti-6Al-4V ingot slab "E" as measured via wet chemical analysis.....	65
28.	Oxygen radial distribution in Ti-6Al-4V ingot slab "A" as measured via wet chemical analysis.....	66
29.	Oxygen radial distribution in Ti-6Al-4V ingot slab "C" as measured via wet chemical analysis.....	67
30.	Oxygen radial distribution in Ti-6Al-4V ingot slab "E" as measured via wet chemical analysis.....	67
31.	Aluminum radial distribution, just above mid-height, in a Ti-6Al-4V laboratory-scale ingot.....	69

32.	Aluminum radial distribution, just below mid-height, in a Ti-6Al-4V laboratory-scale ingot.....	69
33.	Vanadium radial distribution, just above mid-height, in a Ti-6Al-4V laboratory-scale ingot.....	70
34.	Vanadium radial distribution, just below mid-height, in a Ti-6Al-4V laboratory-scale ingot.....	71
35.	Iron radial distribution, just above mid-height, in a Ti-6Al-4V laboratory-scale ingot.....	72
36.	Iron radial distribution, just below mid-height, in a Ti-6Al-4V laboratory-scale ingot.....	72
37.	Predicted aluminum segregation, from the LSRE, using partition coefficients from the literature and thermodynamic calculations.....	82
38.	Predicted vanadium segregation, from the LSRE, using partition coefficients from the literature and thermodynamic calculations.....	82
39.	Predicted iron segregation, from the LSRE, using partition coefficients from the literature and thermodynamic calculations.....	83
40.	Predicted oxygen segregation, from the LSRE, using partition coefficients from the literature and thermodynamic calculations.....	83
41.	Predicted aluminum segregation, from the LSRE, using minimum and maximum values of primary dendrite arm spacing.	84
42.	Predicted vanadium segregation, from the LSRE, using minimum and maximum values of primary dendrite arm spacing.	85
43.	Predicted iron segregation, from the LSRE, using minimum and maximum values of primary dendrite arm spacing.	85
44.	Predicted oxygen segregation, from the LSRE, using minimum and maximum values of primary dendrite arm spacing.	86
45.	Predicted aluminum segregation, from the LSRE, using varied mushy zone pressure drops.	87
46.	Predicted vanadium segregation, from the LSRE, using varied mushy zone pressure drops.	87
47.	Predicted iron segregation, from the LSRE, using varied mushy zone pressure drops.	88
48.	Predicted oxygen segregation, from the LSRE, using varied mushy zone pressure drops.	88

49.	Predicted aluminum segregation, from the LSRE, using varied mushy zone pressure drops.	89
50.	Predicted aluminum segregation, from the LSRE, using varied mushy zone lengths.	90
51.	Predicted vanadium segregation, from the LSRE, using varied mushy zone lengths.	90
52.	Predicted iron segregation, from the LSRE, using varied mushy zone lengths.	91
53.	Predicted oxygen segregation, from the LSRE, using varied mushy zone lengths.	91
54.	Predicted aluminum segregation, from the LSRE, using varied mushy zone lengths.	92
55.	Predicted aluminum segregation, from the LSRE, using varied temperature gradients (G) and cooling rates (ϵ).	93
56.	Predicted vanadium segregation, from the LSRE, using varied temperature gradients (G) and cooling rates (ϵ).	93
57.	Predicted iron segregation, from the LSRE, using varied temperature gradients (G) and cooling rates (ϵ).	94
58.	Predicted iron segregation, from the LSRE, using varied temperature gradients (G) and cooling rates (ϵ).	94
59.	Predicted aluminum segregation for slab "C" using Lever rule and Scheil equation.	96
60.	Predicted aluminum segregation for slab "C" using the LSRE.....	96
61.	Predicted vanadium segregation for slab "C" using Lever rule and Scheil equation.	97
62.	Predicted vanadium segregation for slab "C" using the LSRE.....	97
63.	Predicted iron segregation for slab "C" using Lever rule and Scheil equation.	98
64.	Predicted iron segregation for slab "C" using the LSRE.	98
65.	Predicted oxygen segregation for slab "C" using Lever rule and Scheil equation.	99

66.	Predicted oxygen segregation for slab "C" using the LSRE.....	99
67.	Schematic of a vacuum arc remelting (VAR) furnace.....	104
68.	Schematic of the electron beam melting process.....	105
69.	Schematic of a plasma arc furnace.....	107
70.	Schematic of a water-cooled crucible used for induction skull melting of investment castings.....	108
71.	DTA trace used for solidus determination for alloy XB3040, trial 4.	116
72.	DTA trace used for liquidus determination for alloy XB3040, trial 4.	117
73.	DTA trace used for solidus determination for alloy XB3041, trial 1.	117
74.	DTA trace used for liquidus determination for alloy XB3041, trial 1.	118
75.	DTA trace used for solidus determination for alloy XB3041, trial 2.....	118
76.	DTA trace used for liquidus determination for alloy XB3041, trial 2.	119
77.	DTA trace used for solidus determination for alloy XB3043, trial 1.....	119
78.	DTA trace used for solidus determination for alloy XB3043, trial 2.....	120
79.	DTA trace used for liquidus determination for alloy XB3043, trial 2.	120
80.	DTA trace used for solidus determination for alloy XB3045, trial 1.....	121
81.	DTA trace used for liquidus determination of alloy XB3045, trial 1.....	121
82.	DTA trace used for solidus determination for alloy XB3045, trial 3.....	122
83.	DTA trace used for liquidus determination of alloy XB3045, trial 3.	122
84.	DTA trace used for solidus determination for alloy XB3048, trial 4.....	123
85.	DTA trace used for liquidus determination of alloy XB3048, trial 4.	123
86.	DTA trace used for solidus determination for alloy XB3049, trial 5.....	124
87.	DTA trace used for liquidus determination of alloy XB3049, trial 5.	124
88.	Microstructures of as-received (a) and post thermal analysis (b, c) samples of the baseline material. Images were taken at center (b) and edge (c) locations for baseline trial 3.	125

89.	Microstructures of post-thermal analysis baseline samples. Images of trial 6 were taken at center (a) and edge (b) locations. Images of trial 7 were taken at center (c) and edge (d) locations.	126
90.	Microstructures of as received (a) and post-thermal analysis (b, c) samples of alloy XB3040. Images of trial 4 were taken at center (b) and edge (c) locations.	127
91.	Microstructures of as-received (a) and post-thermal analysis (b, c) samples of alloy XB3041. Images were taken at center (b) and edge (c) locations for trial 1.....	128
92.	Microstructures of post-thermal analysis XB3041 alloy sample, trial 2. Images were taken at center (a) and edge (b) locations.....	129
93.	Microstructures of as-received (a) and post-thermal analysis (b, c) samples of alloy XB3043. Images were taken at center (b) and edge (c) locations for trial 1.....	130
94.	Microstructures of post-thermal analysis XB3043 alloy sample, trial 2. Images were taken at center (a) and edge (b) locations.....	131
95.	Microstructures of as-received (a) and post-thermal analysis (b, c) samples of alloy XB3045. Images were taken at center (b) and edge (c) locations for trial 1.....	132
96.	Microstructures of post-thermal analysis XB3045 alloy sample, trial 3. Images were taken at center (a) and edge (b) locations.....	133
97.	Microstructures of as-received (a) and post-thermal analysis (b, c) samples of alloy XB3048. Images were taken at center (b) and edge (c) locations for trial 4.....	134
98.	Microstructures of as-received (a) and post-thermal analysis (b, c) samples of alloy XB3049. Images were taken at center (b) and edge (c) locations for trial 5.....	135
99.	Predicted aluminum segregation, from the LSRE, using varied temperature gradients (G) and cooling rates (ϵ) for conditions of a fully columnar float-zone directionally-solidified casting.	140
100.	Predicted vanadium segregation, from the LSRE, using varied temperature gradients (G) and cooling rates (ϵ) for conditions of a fully columnar float-zone directionally-solidified casting.	141
101.	Predicted iron segregation, from the LSRE, using varied temperature gradients (G) and cooling rates (ϵ) for conditions of a fully columnar float-zone directionally-solidified casting.	141

102.	Predicted oxygen segregation, from the LSRE, using varied temperature gradients (G) and cooling rates (ϵ) for conditions of a fully columnar float-zone directionally-solidified casting.	142
103.	Predicted aluminum segregation, from the LSRE, using varied temperature gradients (G) and cooling rates (ϵ) for conditions of a fully equiaxed cylindrical casting.	142
104.	Predicted vanadium segregation, from the LSRE, using varied temperature gradients (G) and cooling rates (ϵ) for conditions of a fully equiaxed cylindrical casting.	143
105.	Predicted iron segregation, from the LSRE, using varied temperature gradients (G) and cooling rates (ϵ) for conditions of a fully equiaxed cylindrical casting.	143
106.	Predicted oxygen segregation, from the LSRE, using varied temperature gradients (G) and cooling rates (ϵ) for conditions of a fully equiaxed cylindrical casting.	144

LIST OF TABLES

<u>Table</u>	<u>Page</u>
1. Results of wet chemical analysis on as-received material. All values reported in weight percent except hydrogen. Hydrogen data reported in parts per million.	47
2. Results of the aluminum evaporative loss calculations.	55
3. Wet chemical analysis results for the top ingot slab (slab "A"). All values are given in weight percent, except hydrogen which is given in parts per million.	58
4. Wet chemical analysis results for the middle ingot slab (slab "C"). All values are given in weight percent, except hydrogen which is given in parts per million.	58
5. Wet chemical analysis results for the bottom ingot slab (slab "E"). All values are given in weight percent, except hydrogen which is given in parts per million.	59
6. Partition coefficients taken from the literature (binary) and calculated for alloy XB3043.	70
7. Input parameters for the sensitivity analysis using the LSRE.	80
8. Example DTA heating scheme.....	115
9. Results of electron probe microanalysis of selected post-thermal analysis samples.....	136
10. Results of microindentation hardness testing.....	137
11. Results of initial thermodynamic calculations for the Ti-6Al-4V alloys.	138
12. Input parameters for segregation calculations for Ti-6Al-4V ingot slab "C" using the LSRE.	139

LIST OF SYMBOLS

SYMBOL	DEFINITION
k	equilibrium partition coefficient
C_s^*	concentration of solute in solid phase at the solid/liquid interface
C_L^*	concentration of solute in liquid phase at the solid/liquid interface
C_0	initial solute concentration
T^*	temperature at which solidification occurs
a_s	activity of a solute in the solid phase
a_L	activity of a solute in the liquid phase
T_L	liquidus temperature
C_s	concentration of solute in the solid phase
C_L	concentration of solute in the liquid phase
f_s	fraction solid
f_L	fraction liquid
C_1	concentration of solute in the liquid phase
β	solidification shrinkage
\mathbf{v}	interdendritic fluid velocity vector
T	temperature
ε	temperature gradient

ρ_s	solid phase density
ρ_L	liquid phase density
K	permeability of the medium (mushy zone permeability)
P	pressure
g_r	acceleration due to gravity
μ	viscosity
C_2	permeability constant
d_1	primary dendrite arm spacing
ΔT_x	temperature gradient in the x-direction
Δx	mushy zone length
ΔP	pressure drop across the mushy zone

CHAPTER I

INTRODUCTION

Segregation, a type of chemical inhomogeneity, is one of the main causes of defects in all types of cast alloys. Both ingots and cast parts have been rejected from various aerospace applications due to segregation-related defects. Macrosegregation, chemical inhomogeneity on the macroscopic level, occurs in almost all casting processes for almost all types of metals and their alloys [1]. For example, single crystal superalloy turbine engine blades have been rejected due to freckles, one type of macrosegregation [2]. Also, a quaternary aluminum alloy, Al-Zn-Mg-Cu, exhibits a high level of segregation following ingot casting [3]. The alloying elements become heavily concentrated at the surface of the cast ingot, resulting in a relatively thick segregation zone. A very expensive scalping operation must be added to the post-processing procedures in order to remove this segregation zone. Additionally, the chemical inhomogeneity over the cross section of an as-cast ingot affects the resulting mechanical properties of the final alloy products [3]. For very large diameter ingots (up to 4.1 m.), the overall solidification rate is very slow and, as such, results in a significant level of macrosegregation. This segregation is most prominent in the center of the ingot [4], and the ingot must be scrapped.

Accurate prediction of macrosegregation is essential to preventing the large expense of scrapped material. The conditions leading to macrosegregation must be very well-understood in order to develop effective models. Modeling macrosegregation, however, can become very complex because the models need to account for every

parameter in the solidification process simultaneously. Also, simulations are time-consuming and require alloy-specific and casting specific parameters, which are often difficult to obtain.

Titanium-Specific Challenges

Improving Ti-6Al-4V ingot homogeneity is not a straightforward task due to the nature of the vacuum arc remelting (VAR) process used to produce most titanium and titanium alloy ingots. For instance, both the start-up and the hot-topping step of the process are transient, and solidification defects are most likely to occur in these locations. The melting process is not the only factor that influences segregation. Ingot size is another parameter that affects the resulting segregation. There are limitations, however, on the improvements that can be made to the production of larger-scale ingots, one meter and greater in diameter, because of the possibility that segregation increases with increasing ingot size [5].

One cause of chemical non-homogeneity in titanium alloy ingots is macrosegregation. Macrosegregation is the separation of the elements contained in an alloy on the macroscopic level (over the range of millimeters to centimeters to meters depending on the casting size). Macrosegregation in titanium ingots is not well understood due to various thermodynamic and transport parameters involved in solidification. Macrosegregation changes the composition distribution of an ingot, which, in turn, changes the freezing range of an alloy and the solid-state phase transformation temperatures.

A solidified Ti-6Al-4V ingot may not meet specifications due to the macrosegregation of oxygen (i.e. non-uniform distribution of oxygen), which affects the beta transus temperature. As a result, the forging temperature relative to the beta transus temperature varies. Thus, titanium ingot producers have a specified range of

oxygen allowed in their products. For most titanium aerospace applications, oxygen ranges from 0.16 to 0.20% by weight, however, some applications allow up to 0.25% oxygen by weight [6]. Mechanical and physical properties are affected if the oxygen content lies outside the allowable range. If the cast ingot does not meet chemistry specifications, the material must be scrapped or the grade (quality) lowered. Both of these measures result in a significant profit loss.

The freezing range of the alloy largely affects macrosegregation of Ti-6Al-4V. It is believed that oxygen segregates to the growing dendrites. Thus, oxygen depleted metal at the center of the ingot may be the last to solidify. Iron content is thought to contribute to the macrosegregation of oxygen. It is difficult to control the iron content in a titanium alloy ingot because the iron is present in the ore in varying amounts.

Other elements that might be present in the Ti-6Al-4V alloy include: carbon, nickel, copper, lead, yttrium, zirconium, nitrogen, hydrogen, chromium, and silicon.

To predict macrosegregation phenomena, the thermodynamics of solidification (e.g. phase diagrams, chemical activity) and the diffusion in both the β phase and the $\alpha + \beta$ phase, must all be determined and understood. The thermal conditions during casting must also be determined.

One challenge of macrosegregation prediction is the lack of phase equilibria data for Ti-6Al-4V. Titanium has a high melting point and is very reactive. As a result, it is difficult to experimentally examine the melting and solidifying processes. Also, the liquidus line on a phase diagram for pure titanium is almost always higher than that for a titanium alloy. With each small change in alloy composition, the phase diagram changes. If only one alloying element has a significant affect on the resulting phase diagram, macrosegregation prediction becomes straightforward. Phase diagrams, however, can become very complex when multiple elements have a significant effect on the results.

The decomposition of the alloy from the β phase to the $\alpha + \beta$ phase during ingot casting masks solidification phenomena like dendrite growth. Finally the short-range diffusion occurs very quickly in the β -phase field [7].

Organization of the thesis revolves around three focal areas, the laboratory-scale investigation, the production-scale investigation, and segregation modeling. Background information on the project including casting, solidification theory, segregation modeling, and thermal analysis is presented in chapter two. The materials used and procedures employed are outlined in chapter three. The results of the characterization study are presented in chapter four. Results of the production-scale investigation are contained in chapter five, and segregation modeling is discussed in chapter six. Conclusions and future work are presented in chapter seven.

CHAPTER II

BACKGROUND INFORMATION

Background information; including titanium alloys, casting, solidification theory, and types of segregation, is covered in this chapter. Segregation modeling, phase equilibria, PandatTM software, and experimental techniques are also discussed. The research objectives and complications are outlined.

2.1 Titanium Alloys

The importance of titanium to the aerospace industry is illustrated in this section. The general structure of titanium and titanium alloys is covered including the effects that varying alloying elements have on that structure.

Ti-6Al-4V is a very important titanium alloy to the aerospace industry due to its excellent properties and wide range of uses. These properties include high strength, low density, high melting point, low coefficient of thermal expansion, and high service temperatures. In 1994, production/purchase of titanium was estimated to range from 40 to 50 million kilograms per year with the aerospace market (both defense and commercial) accounting for the majority of the applications [8]. Commercially, Ti-6Al-4V is available in the following forms: ingot, bar, billet, plate, sheet, seamless pipe, seamless tubing, wire, and foil [5].

Metallic compounds exhibit a crystalline structure. The atoms align themselves in the most energetically favorable structure, generally cubic for metals. For pure titanium and

titanium alloys, two structures are energetically favorable, hexagonal close packed and body-centered cubic. In titanium, the hexagonal close packed structure is termed the alpha phase, and the body-centered cubic structure is termed the beta phase [9]. In pure titanium, the alpha phase is stable from room temperature to approximately 882°C (1620°F), while the beta phase is stable in the approximate range of 882°C (1620°F) to 1668°C (3040°F), which is the melting point. The transition from a completely beta phase alloy to an entirely alpha phase alloy and vice-versa occurs at a temperature known as the beta transus temperature. The beta transus temperature for pure titanium is 882°C (1620°F).

Three categories of titanium alloys exist at room temperature. These are termed alpha, beta, and alpha-beta (α/β) alloys. Ti-6Al-4V is an α/β alloy, exhibiting both the hexagonal close packed and the body-centered cubic structures at room temperature. As an α/β alloy, Ti-6Al-4V exhibits traits of each phase [9]. The average beta transus temperature for Ti-6Al-4V is approximately 996°C (1825°F), and the melting range is 1605 to 1670°C (2920 to 3040°F).

An alloying element will exhibit one of three effects when added to titanium. The element is termed an alpha phase stabilizer if it stabilizes the alpha phase at higher temperatures. The element is a beta phase stabilizer if it maintains the beta phase at lower temperatures. Other elements are considered neutral additives because they do not have a significant influence on the stabilization of either phase [9]. Important alpha stabilizers for titanium are aluminum and oxygen. Important beta stabilizers are vanadium and iron. Other trace elements including hydrogen, nitrogen, and carbon are found in alloys since titanium is very reactive. Essentially, Ti-6Al-4V is a three-component system; however, iron and oxygen also impact the phase equilibria.

2.2 Casting of Titanium Alloys

The typical processing path of α/β titanium alloys is outlined in this section with emphasis on the specific casting procedures. The industrial casting procedures that are discussed are vacuum arc remelting, electron beam melting and casting, plasma arc melting, and induction skull melting. Investment casting and button melting are also discussed briefly.

2.2.1 Ingot Casting

The typical industrial processing path for α/β titanium alloy ingots comprises four steps. The steps include production, breakdown, recrystallization annealing, and secondary processing. The ingot is first produced via vacuum arc remelting (VAR), electron beam melting and casting, or plasma arc melting (PAM). Titanium and titanium alloys ingots are typically produced via the VAR process [10]; however, all three methods are discussed. Breakdown, usually preheating and then forging or upsetting, of the ingot is done in the beta phase field, usually ending below beta transus temperature. Then the ingot undergoes recrystallization annealing in the beta phase field. The purpose of recrystallization annealing is to improve the mechanical properties of the material. Finally secondary processing (rolling, forging, extruding, etc.) is performed in the α/β phase field [11]. Only the extraction of the ore and the ingot production steps are discussed in detail because macrosegregation arises during ingot solidification.

The process for producing a titanium alloy ingot begins with production of the titanium sponge from the extracted titanium ore. Two main techniques are currently employed in industry to extract titanium from its ores. These methods, named for their creators, are the Kroll process and the Hunter process, and they reduce the titanium ore to titanium metal [12]. The unrefined material is termed titanium 'sponge' due to its

porous features. After reduction, the sponge undergoes several purification steps, with the resultant purity depending on both the initial ore and the extraction process [13].

For VAR and some PAM processes, the purified sponge and desired alloying elements are then combined and pressed into briquettes. These briquettes are welded together, forming a “consumable” electrode. Thus, the consumable electrode is then ready to be melted for ingot production.

The VAR, PAM, and electron beam cold hearth melting processes are used to cast production-scale ingots. The VAR process uses a consumable electrode for the feedstock. PAM can be used to create a consumable electrode. The feedstock for plasma arc remelting can be a consumable electrode. Electron beam cold hearth melting does not require a consumable electrode, and induction skull melting is most often used for casting of parts or small ingots. Refer to Appendix A: Casting of Titanium Alloys for detailed descriptions of each casting process.

2.2.2 Other Casting Methods

Other titanium alloy casting methods include investment casting and button melting. Investment casting is used to make complex aircraft components. Button melts are used to evaluate production-scale material properties in a laboratory setting. Refer to Appendix A for detailed descriptions of these casting processes.

2.3 Solidification Theory

The transformations that occur during solidification of a metallic alloy are discussed in this section.

In order for solidification to occur, energy must be transferred from the system (the molten alloy) to the surroundings. This energy transfer changes the free energies of the components in the system, which in turn, changes the thermodynamic stability of the

existing phases. In order to transform from one phase to another (liquid to solid) the system must rearrange on the atomic level. This rearrangement may occur over a very short range with atoms moving only a very short distance from their starting place, or the rearrangement may happen over a somewhat larger scale, the microscopic level [14]. "Microscopic" indicates movement on the order of microns. The rearrangement is also able to occur over an even larger scale, the "macroscopic" scale. The term "macroscopic" indicates the segregation is large compared to the spacing of the dendrite arms [15], or is on the order of millimeters, centimeters, or larger. Since equilibrium is the most stable state, a driving force is required to change the liquid to solid irreversibly. Irreversibly means that the system will not spontaneously return to the liquid phase. The driving force for this process is the minimization of the Gibbs free energy of the system. Two major stages of solidification are nucleation and growth.

Nucleation, the formation of the dendrite nuclei, begins at a specific temperature that is below the equilibrium liquidus temperature for the system. This temperature is often referred to as the degree of undercooling or supercooling. For metals, the degree of undercooling necessary to initiate nucleation is often very small [14]. Homogeneous nucleation occurs when solid forms without the aid of foreign material [16]. This type of nucleation requires a very large driving force and, thus, is not common in normal casting. Heterogeneous nucleation occurs when solid forms on foreign material like impurity particles or the mold walls. Unlike homogeneous nucleation, heterogeneous nucleation requires only a small degree of undercooling, sometimes only approximately 1 K [17].

After nucleation occurs, solutes or alloy components must transform from the liquid phase to the solid phase in order for the grains to grow and the crystallographic structure to develop [14]. The number of grains stays approximately the same during the growth stage; however, the grains begin to expand. First the grains lengthen until they touch one another, and then they thicken. Growth is limited by the kinetics of solid/liquid

interface atom attachment, capillarity, and diffusion of heat and mass [14]. The factor most influencing growth depends on both the material and the solidification conditions [14]. The nucleation rate, as well as the growth rate, decreases with an increase in the degree of undercooling to a point.

For large ingots and castings, nucleation and grain growth begin immediately after the molten metal touches the cool mold walls [18]. Heterogeneous nucleation begins with formation of nuclei on the mold walls. The type of grains that form depends on the pouring temperature [17]. A low pouring temperature leads to detachment of the small solid particles. These particles move into the liquid pool where rapid solidification occurs, resulting in a completely equiaxed structure.

A high pouring temperature leads to remelting of any particles that detach from the mold walls. Particles that remain attached, the chill grains, begin to grow. The temperature gradient between the mold walls and solidifying metal decreases, and the chill grains grow inward, dendritically. Grains, with fast growth direction (e.g. 001 in cubic metals), in the most favorable orientation (close to the direction of the heat flow) grow the quickest [17]. Finally, equiaxed grains, having a random orientation, comprise the center of the casting (Figure 1).

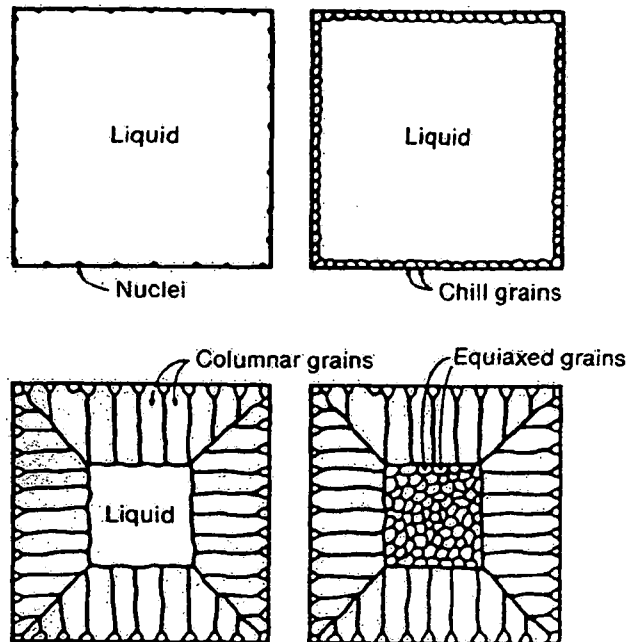


Figure 1. Solidification sequence of ingots and large castings [18].

During solidification, three zones develop in the pure metal or alloy. The solid zone contains material that has solidified, and the liquid zone contains the molten metal. The mushy zone is comprised of both solid and liquid as the molten liquid solidifies. The solid portion of the mushy zone contains the growing dendrites (grains). The liquid portion of the mushy zone is referred to as the interdendritic liquid because it flows between the growing dendrites.

2.4 Types of Segregation

The types of segregation and their differences are defined in this section.

There are two types of segregation, microsegregation and macrosegregation. Microsegregation is the variation of alloying elements over a microscopic distance, approximately 10-100 μm . The cause of microsegregation is the solubility differences of the solutes in the solid and liquid phases of an alloy system at a specific temperature [1]. Macrosegregation is the separation of the elements contained in an alloy on the

macroscopic level (over the range of millimeters to centimeters to meters depending on the casting size). Macrosegregation is caused by the movement of the liquid and solid phases during the solidification process [2]. Positive macrosegregation refers to an area of a casting in which the concentration of a specific solute is greater than the average alloy composition, while negative segregation refers to an area of a casting in which the concentration of a specific solute is less than the average alloy composition.

In titanium ingot casting, diffusion occurs quickly when the material exists in the beta phase field [7]. Microsegregation effects are considered negligible relative to those resulting from macrosegregation because microsegregation is a diffusion-controlled process. Additionally, the negative effects of microsegregation can be reversed in later processing steps, which is not true for macrosegregation [19]. Understanding microsegregation, however, is essential to developing macrosegregation theories [20].

2.5 Segregation Modeling

The types of models are discussed in this section as well as their usefulness with regard to experimental findings.

Modeling of segregation began on the simplest system, a binary alloy undergoing equilibrium dendritic solidification. As time went on, model complexity increased as a larger number of solidification parameters could be considered simultaneously. Microsegregation models were developed initially and then extended to account for macrosegregation.

2.5.1 Microsegregation Models

The earliest model considered equilibrium solidification of a binary alloy. The equilibrium partition ratio k is an important factor in solidification models and is based on

the equilibrium phase diagram for a specific alloy. The value of k is dependent on temperature.

$$k = \frac{C_s^*}{C_L^*} \quad (1)$$

C_s^* , the composition of a solute (in weight percent) in the solid phase at the interface, and C_L^* , the composition (in weight percent) of a solute in the liquid phase at the interface, are determined from the equilibrium phase diagram for constant temperature (Figure 2). This value is unique for each solute.

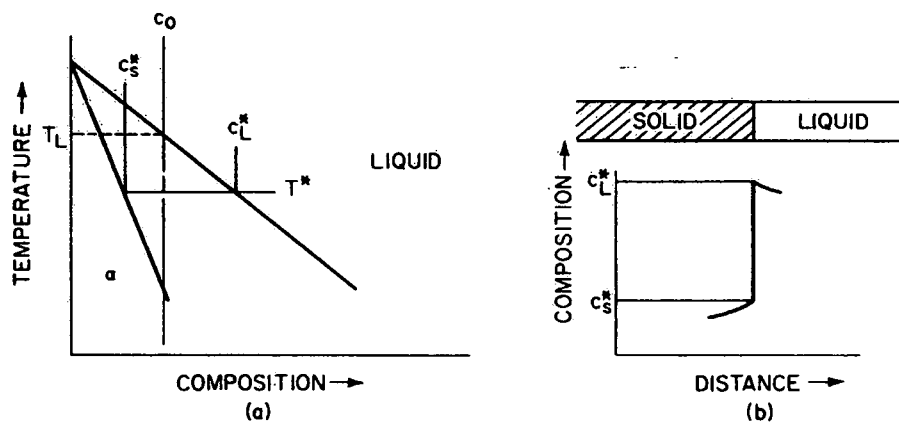


Figure 2. Equilibrium solidification, a) binary phase diagram; b) composition profile across the interface [16].

If the solidus and liquidus lines are straight, the value of k remains constant. When the solidus and liquidus lines are very close together, k is close to one. If the lines are far apart, then k becomes small.

The equilibrium partition ratio can also be determined via thermodynamics [19],

$$k = \frac{a_s}{a_L} \quad (2)$$

where a_s and a_L are the activity of a solute i in the solid and liquid phases, respectively, at a specified temperature. For a dilute binary alloy, the partition ratio is determined via Henry's Law. Note that this form of the partition ratio does not account for interactions between alloying elements.

An early analysis, the equilibrium lever rule, assumed k constant, at a given temperature, to simplify the mathematics. The physical basis for the model was a molten alloy contained in a crucible of defined length solidifying from one end [16]. As established by the equilibrium phase diagram, the first drop of liquid solidifies at the liquidus temperature, T_L , with a composition kC_0 . This solidified droplet is lower in solute concentration than that of the initial liquid, as depicted on an equilibrium phase diagram. Thus, some of the solute is rejected into the liquid, where complete diffusion is assumed. The assumption of complete liquid phase diffusion when combined with the assumption of complete solid-phase diffusion results in a uniform concentration in each phase, with $C_s^* = C_s$ and $C_L^* = C_L$ [16]. A mass balance written at temperature T^* , the temperature at which solidification occurs, is

$$C_s f_s + C_L f_L = C_0 \quad (3)$$

C_0 is the initial alloy concentration, f_s , is the fraction solid, and f_L is the fraction liquid.

The assumptions of the lever rule include complete diffusion in the solid and the liquid phase, liquid-solid interface equilibrium, and no significant degree of undercooling prior to the onset of nucleation [16]. Thus, the lever rule is a physics-based model that is solved analytically.

The first advancement to the lever rule was to assume that there was no diffusion in the solid phase (Figure 3). To include this assumption, the same basis is utilized as that used to determine the equilibrium lever rule. A molten alloy is again contained in a crucible of defined length [16]. When solidification begins at the liquidus temperature, T_L ,

the first drop of liquid will solidify with a composition kC_0 , identical to that formed in equilibrium solidification. Similar to equilibrium solidification, the liquid becomes enriched with solute, as different alloying elements freeze at different temperatures over the course of solidification. Due to the assumption of no solid diffusion, the composition of the solid formed initially does not change over the course of solidification. A mass balance is performed over the solute by equating the amount of solute rejected from the solid phase to the amount of solute added to the liquid phase. The resulting mass balance is

$$(C_L - C_s^*)df_s = (1 - f_s)dC_L \quad (4)$$

The fraction solid is represented by f_s . After substitution of k

$$(C_L - kC_L)df_s = (1 - f_s)dC_L \quad (5)$$

and integration with $C_L = C_0$ at $f_L = 0$, the relation for the composition of the liquid at the interface becomes

$$C_L = C_0 f_L^{(k-1)} \quad (6)$$

The solid phase solute concentration is determined via the partition coefficient,

$$C_s^* = kC_0 (1 - f_s)^{(k-1)} \quad (7)$$

where f_L is the fraction of liquid phase and concentrations are in units of weight percent.

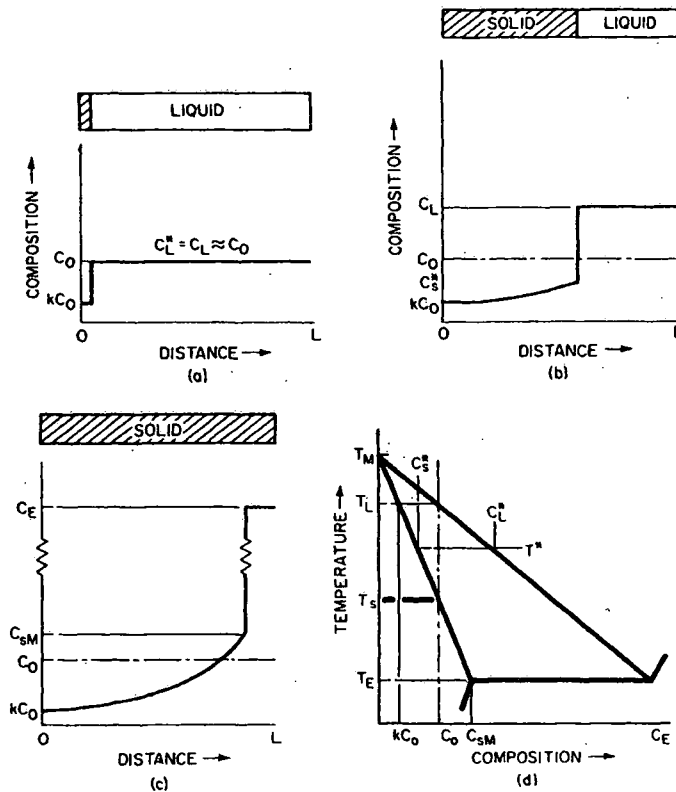


Fig 3. Segregation modeling using the Scheil equation with the assumptions of no solid diffusion and complete liquid diffusion. a) beginning of solidification, b) at temperature T^* , c) end of solidification d) binary phase diagram [16].

As the slope of the liquidus and solidus lines become less constant, the validity of the lever rule and the previous equations, called the nonequilibrium lever rule or the Scheil equation, decreases. Scheil developed this equation in the late 1930's, using the work of Gulliver as a basis for his research [20]. Similar to the lever rule, the basis of the Scheil model is physics, and the solution is analytical in nature.

The Scheil equation can be explained with use of a small volume element contained in the mushy zone [20]. This volume element contains a portion of a dendrite and is described by the volume fraction solid, f_s [21]. Over the course of solidification, f_s ranges from 0 (at the beginning) to 1 (at the end). If the initial component concentration and equilibrium partition coefficient are known, then f_s can be selected and the

concentration in the solid phase determined. Plots can be developed that show how the solid phase concentration of a component changes over the course of solidification.

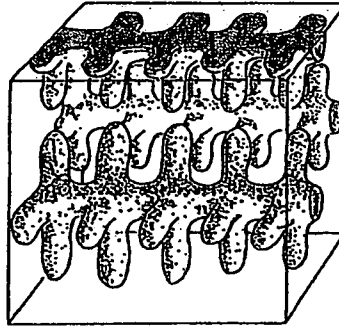


Figure 4. Small volume element contained in the mushy zone [20].

The assumptions for the Scheil model are the same as those for the equilibrium lever rule, with one exception. The Scheil equation assumes no solid-phase diffusion. If a value is chosen for the fraction solidified, then the composition of that solid phase can be determined via the Scheil equation. Differences between the Scheil model predictions and experimental observations are attributed to the fact that a degree of solid diffusion is observed in numerous alloy systems [16].

The next advancement to the lever rule was to change the assumption of complete liquid-phase diffusion to that of limited liquid diffusion, without considering convection [16]. The assumption of no solid-phase diffusion held for this model. Solidification was assumed to begin in a similar fashion to that outlined previously, in which the initial solid formed will have composition kC_0 . An enriched "solute boundary layer" forms due to the solute movement via diffusion in the liquid [16].

Steady-state solute transport is achieved if the casting has adequate length (Figure 3). Once steady state has been established, solid that forms has the same composition as the initial molten alloy [16]. Assuming that equilibrium occurs at the solid-

liquid interface, the equilibrium partition ratio can be used to determine the composition of the liquid phase at the interface. If C_s^* equals C_o , then C_L^* will equal C_o/k . It follows that the solidification occurs at the solidus temperature.

Other early extensions to the Scheil equation include coarsening, undercooling before nucleation, and application to multi-component alloys [20]. Note that heat flow was not directly considered in the development of these microsegregation models. Collectively, the various equations are termed the "local solute redistribution equation" or LSRE. This set of equations for microsegregation prediction is the basis of present macrosegregation modeling efforts [20] (i.e. Present modeling begins with the use of one of these equations developed from the Scheil model for microsegregation.). Additional equations, however, are required for macrosegregation modeling. These microsegregation equations represent analytical and empirical modeling.

The validity of the Scheil equation for various applications was studied heavily in the 1950's and early 1960's. In the late 1960's, it was established that the Scheil and its modifications were valid for microsegregation modeling in normal castings [20].

Convection in both liquid and solid phases can cause microsegregation to turn into macrosegregation. After casting, microsegregation can be eliminated via further processing like soaking and hot working [19]. Macrosegregation, however, is a quality control issue because subsequent processing cannot eliminate it, and the material must be scrapped.

2.5.2 Macrosegregation Models

Macrosegregation is a complex phenomenon. As such, many parameters influence macrosegregation in a cast product. The main cause of macrosegregation is movement of solid and liquid within the mushy zone [1]. The major factors that affect

movement of solid and liquid are the size of the casting, the solidification rate, method used to extract heat, material composition, and superheat [19].

In order to accurately model macrosegregation, the solidification process must be well understood. Due to different freezing points, alloying elements (solutes) solidify at different conditions. During solidification, some of the solutes are rejected into the interdendritic liquid [19]. Solute rejection leads to the development of a concentration gradient within the liquid portion of the casting. As a result, a density gradient also develops. This situation is referred to as solutal buoyancy, which can be positive or negative [19]. Solutal buoyancy causes natural convection, which is termed solutal convection.

2.5.2.1 Binary Alloy Solidification Models

Macrosegregation modeling began with the simplest model, an extension of the Scheil equation for macrosegregation, and became increasingly complex as time passed. The developing field of computer technology allowed researchers to account for more solidification parameters in their models and to reduce the number of assumptions used.

The simplest macrosegregation models were developed in the late 1950's through the early 1970's by J.S. Kirkaldy and W.V. Youdelis (1958), M.C. Flemings and G.E. Nereo (1967), and R. Mehrabian, M. Keane, and M.C. Flemings (1970) as discussed elsewhere [1]. Similar to the microsegregation model, a volume element was employed. For macrosegregation, interdendritic fluid flow in the mushy zone was considered.

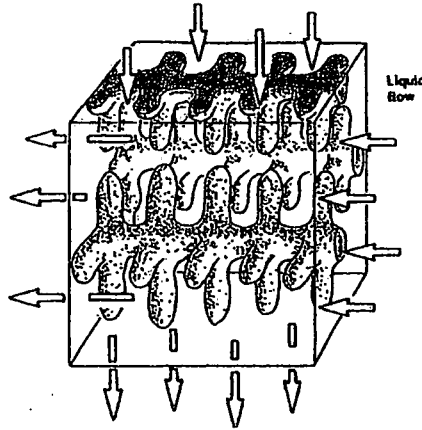


Figure 5. Small volume element in the mushy zone incorporating interdendritic fluid flow [20].

The volume element contained a portion of a dendrite that was immobile. Liquid was allowed to flow in between the dendrites as well as in and out of the volume element. Flow in the bulk liquid phase and solid deformation were not directly considered for this model [1]. The resulting extension to the Scheil equation was the LSRE [2].

$$\frac{df_L}{dC_L} = -\frac{(1-\beta)}{(1-k)} \left[1 + \frac{\mathbf{v} \cdot \nabla T}{\varepsilon} \right] \frac{f_L}{C_L} \quad (8)$$

where f_L = fraction liquid

C_L = concentration of solute in the liquid phase (in weight percent)

β = solidification shrinkage

k = equilibrium partition coefficient

\mathbf{v} = interdendritic fluid velocity vector

T = temperature

ε = temperature gradient

The composition of the solid phase (in weight percent) is determined via the partition coefficient after integration. The integrated form of the equation, assuming all parameters constant except f_L and C_L is as follows

$$C_S = kC_O (1 - f_S)^{\frac{-\varepsilon(1-k)}{(1-\beta)(\varepsilon + (\mathbf{v} \cdot \nabla T))}} \quad (9)$$

The solidification shrinkage, β , is defined in terms of the liquid (L) and solid (S) densities.

$$\beta = \frac{(\rho_s - \rho_L)}{\rho_s} \quad (10)$$

The LSRE describes the effect of interdendritic fluid flow on the concentration of the components in the liquid and solid phases for a desired volume fraction solid. The equation also provides a means of calculating an average composition at any part of a solidified ingot.

When the LSRE is combined with Darcy's law, which describes the flow between the dendrites, the two provide quantitative macrosegregation information for a particular casting. Darcy's law is valid for flow through a porous medium, and the mushy zone is a porous medium. For the condition of macrosegregation, Darcy's law provides a means for determination of the average interdendritic flow velocity v [16].

$$v = -\frac{K}{\mu f_L} (\nabla P + \rho_L g_r) \quad (11)$$

where K = permeability of the medium (mushy zone permeability)
 μ = viscosity
 f_L = fraction liquid
 P = pressure
 ρ_L = liquid phase density
 g_r = acceleration due to gravity

Using both the LSRE and Darcy's Law in their models, researchers were able to make predictions about macrosegregation and verify them through experimentation for a variety of alloys and types of casting processes/pieces [2]. Thus heat flow and fluid flow (in the mushy zone) were combined to predict macrosegregation. These methods are empirical in nature since the permeability value can be changed to make predicted macrosegregation more closely match experimental data.

2.5.2.2 Extension to Multi-Component Alloys

By the mid to late seventies, Fujii, Poirier, and Flemings extended the LSRE and Darcy's flow model to multicomponent alloys, specifically, a low alloy steel in ingot form [22]. Heat and momentum transport equations were solved simultaneously for the first time in macrosegregation modeling history. A computer program was utilized to solve the transport equations using finite difference methods. Several assumptions were made to simplify calculations. These assumptions included no solid diffusion and constant solid-phase density [22]. Similar to previous macrosegregation models, temperature data were obtained from experimental measurements.

This model accounted for some of the main parameters that impact macrosegregation, however, it did not directly account for flow in the bulk liquid phase [1]. The results established that the value chosen for the permeability had a significant impact on the accuracy macrosegregation predictions. Fujii et al. were able to predict channel-type segregation patterns if the value chosen for the permeability was "suitable" [22]. The equations were solved numerically; however, the model was empirical in nature due to permeability variance.

Flow in the bulk liquid was first considered in macrosegregation modeling in the late 1970s by Ridder, Kou, and Mehrabian [23]. The research was aimed at predicting macrosegregation in binary ingots produced via ESR, VAR, and continuous casting processes. Darcy's law, the LSRE, and heat transfer equations were used to model the mushy zone. A variable permeability coefficient was used to account for the difference in permeability with changing dendrite arm spacing. Both momentum and energy equations were used to model flow in the liquid phase [2]. Forced convection was not considered in the all-liquid zone. Steady state conditions, constant density, constant thermal conductivity, no viscous dissipation, and axi-symmetric flow were all assumptions made for the bulk liquid phase [23].

The equations for the mushy zone were coupled with those for the liquid zone and solved numerically using a computer program. Temperature data were obtained experimentally as in the earlier macrosegregation models. The results showed good agreement between predicted and measured macrosegregation patterns. Ridder and colleagues [23] concluded that natural convection in the liquid pool does not significantly affect macrosegregation when using temperature data obtained experimentally.

Macrosegregation modeling experienced much growth throughout the mid-1980s and early nineties with an increasing number of modifications made to earlier models [2]. The mushy zone was studied extensively. A group of mathematicians produced a theoretical model of a mushy zone for a binary alloy in the early 1980s [24]. This model was physics-based, and it was one-dimensional. Bennon and Incropera extensively studied the transport processes occurring within the mushy zone [25]. They based their model on so-called mixture theory. The basic theory behind the model is that any part of the mushy zone can contain both solid and liquid. Their model was also one-dimensional [2].

Another one-dimensional model used a volume-averaging technique to model the mushy zone [25]. The mushy zone was taken to contain two "interpenetrating phases" [25]. The microscopic properties of a phase were considered constant throughout that phase but were considered discontinuous over the entire mushy zone. The mass and momentum equations were written on the microscopic scale; however, and averaged over a set volume. The equations were averaged in order to reduce complexity of calculation. This volume-averaging method changes the conservation equations from microscopic to macroscopic [25]. The results of this study determined that different coefficients, of permeability and resistance, must be used for columnar and equiaxed structures.

Other researchers used mixture theory or the volume-averaging technique to model the mushy zone, as presented elsewhere [2], and these models are termed "single domain models" [2]. These models require numerical methods and computational resources in order to accurately predict macrosegregation. The development of these single domain models was a huge step in macrosegregation modeling; however, the models were only applicable to binary systems.

The columnar-to-equiaxed transition (CET) was also examined throughout 1980s. The work began with an analytical model used for qualitative predictions [26]. This model was later extended to make quantitative predictions for an ingot. The advanced model, however, was one-dimensional and failed to consider conservation of alloying components [26]. Since conservation was not considered, model predictions were likely to have serious errors. Other CET modeling work includes research efforts using Monte-Carlo methods and experimental research on binary alloys [26]. Still, these additional modeling efforts failed to accurately predict/describe the CET occurring during solidification.

2.5.2.3 Coupled Micro-Macro Models

Researchers started to focus on coupled microsegregation and macrosegregation models in the late 1980s and early 1990s. The goal of these models was to include microscopic occurrences in the macrosegregation equations in order to predict the resulting macrostructure [26]. These coupled models have been developed for both columnar and equiaxed solidification conditions.

Poirier and Heinrich established a basis for relating permeability to prediction of freckles during vertical solidification [27]. They used a two-dimensional approach to numerically model the mushy zone. In order to effectively balance computational time and costs, the area modeled for each computation was small. Permeability values were

taken from literature or determined from experimental data. This research established the need for further examination of permeability in order to more accurately predict macrosegregation. The authors proposed a direct simulation method to obtain permeability data [27]. This study also confirmed that permeability varied with microstructure. A drawback to this research is that it was not aimed at multi-component alloys or at production-scale castings. Other work in this area has been summarized elsewhere [2].

Another coupled micro-macro model of the early 1990s was aimed at determining how microsegregation, permeability, and fluid flow affected macrosegregation [28]. This work focused on a binary alloy that formed a eutectic upon solidification. The single-domain, numerical model was based on a volume-averaging technique. Several assumptions were made to simplify calculations. These assumptions included: thermal equilibrium in an "averaging volume," completely mixed liquid in that volume, either complete or absent microscopic solid diffusion, thermal equilibrium at the solid-liquid interface, and no macroscopic gradients or fluxes [28]. Darcy's law was utilized for flow within the mushy zone with varied permeability. Permeability values were taken from literature and varied widely. The authors concluded that the mushy zone permeability must be further examined [28]. The overall modeling established very little difference between the assumptions of complete diffusion and no diffusion. One problem was that the model was two-dimensional and the goal was to predict three-dimensional phenomena.

Models for multicomponent alloy systems that accounted for fluid flow in the liquid and the mushy zone were developed in the early to mid-1990s [29]. Modeling efforts were concentrated on steels, nickel-based alloys, and superalloys.

2.5.2.4 State of the Art

The focus of current macrosegregation models is to balance the number of solidification parameters included in the model with the available computational resources. For a coupled model in which all microscopic parameters were determined via direct numerical simulation, macrosegregation could be predicted for "scales of the order of several millimetres [sic] (requiring of the order of 10^9 to 10^{12} grid points in three dimensions)" [2]. This model could only be developed with advances in computer technology. Other work is focused on examination of how the computational area affects the resulting macrosegregation patterns [30] and on porosity predictions [31]. Research has also been directed in the area of solid-phase particle movement [32, 33]. These and many other research efforts, however, are not focused on macrosegregation modeling of titanium alloys. Instead they focus on modeling segregation in steels, aluminum alloys, nickel alloys, superalloys, etc.

A limited amount of solidification modeling work has been published for titanium alloys. The School of Mines, in Nancy, France, has developed a model to simulate the VAR process [34]. This model is numerical and based on a finite volume method. Experimental work was conducted on commercially pure titanium and Ti-6Al-2Sn-4Zr-2Mo alloy. The numerical model can simulate various events associated with the VAR process like hot-topping, ingot cooling, ingot inversion, etc. [34]. Electrode composition information was experimentally determined and used in the simulation. The predicted oxygen segregation was in good agreement with experimental findings for a small-scale ingot.

A Ti-6Al-4V ingot was used for a large-scale solidification simulation. The predicted oxygen segregation for this ingot had varied agreement with measured values. The largest variations from experimental findings were found at the top center location of

the ingot [34]. A triple-melted full-scale titanium ingot required approximately a week to complete the simulation on a standard PC [34]. This work did not establish a connection between iron concentration and the resulting oxygen macrosegregation. The accuracy of the predicted oxygen segregation could be improved as well, and computational time could be reduced with additional advances in computer technology.

2.6 Phase Equilibria

A brief discussion of the thermodynamic parameters necessary to construct phase diagrams and model solidification of alloy systems is provided in this section.

Determination of phase diagrams is essential to segregation modeling. Thermodynamics can be utilized to determine the phase diagram for a particular alloy system as an alternative to solely empirical methods.

A phase diagram is a graphical representation of the thermodynamic relationships between different phases existing in the alloy system [35]. The lines on the diagram (solidus, liquidus, etc.) can be determined using Gibbs energy functions for each phase present in the system [35]. The Gibbs energy accounts for the energy of each component present in each phase as well as the energy associated with mixing.

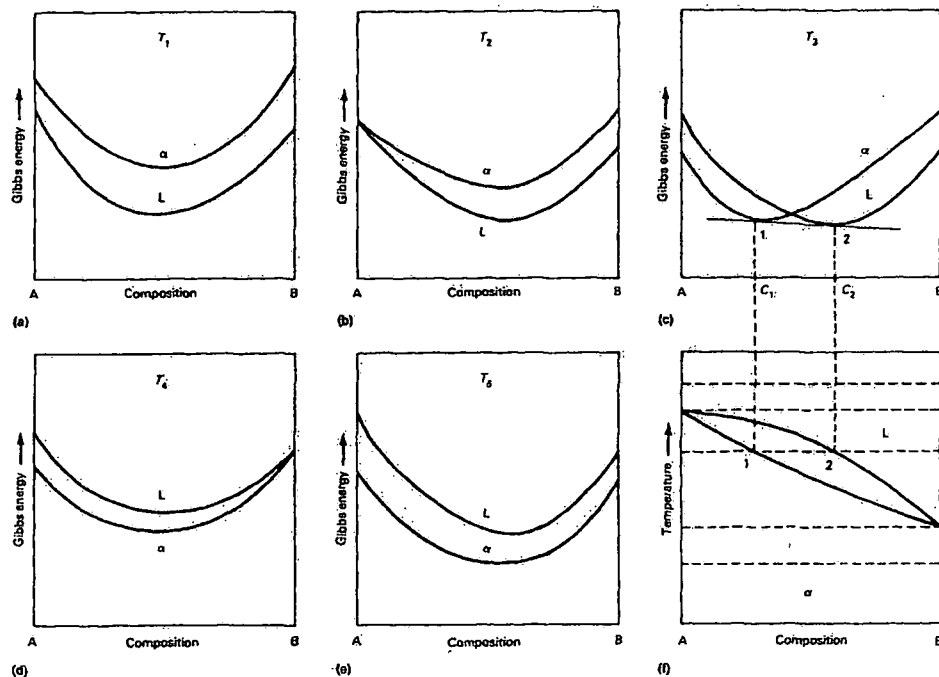


Figure 6. Utilization of Gibbs energy curves to develop a phase diagram for a binary system [35].

The Gibbs energy is usually determined under conditions of constant pressure and temperature. The composition of a binary system ranges from one hundred percent of species "A" to one hundred percent species "B". The Gibbs energy is calculated for a variety of temperatures and utilized to construct the phase diagram for a binary alloy system (Figure 6). The phase diagram curves for the two-phase region (liquid plus solid) are developed using those Gibbs energy diagrams in which the two phases are in equilibrium. The compositions of solidus and liquidus points, for a given temperature, are determined by drawing a line tangent to two curves that intersect on a Gibbs energy diagram (Figure 6c). The basis for this method lies in the principles of thermodynamics [35]. These points are then transferred to an isothermal line on a phase diagram (Figure 6f). This process is repeated for other temperatures in order to fully develop the phase diagram curves. Determination of phase diagrams for higher order systems becomes increasingly complex, requiring the solution of many equations. Computational packages

are often used to calculate phase diagram curves for higher order alloy systems, which require solution of numerous equations as well as knowledge of many physical parameters (diffusion coefficients, density, latent heat, etc.).

2.7 Pandat™ Software for Thermodynamic Calculations

The capabilities of a computational package produced by CompuTherm, LLC are highlighted in this section.

Pandat™ (licensed by CompuTherm, LLC) is a computational package that has several applications for multicomponent alloy systems. Pandat is used to calculate phase equilibrium, phase diagrams, and liquidus projections. Solidification simulations are performed using either the Lever or Scheil model to predict microstructure and microsegregation. Pandat also contains thermodynamic databases necessary to perform these calculations. These databases are based on models of Gibbs free energy for each phase contained within the alloy system [36].

Thermodynamic databases are available for several alloy systems, including those alloys based in aluminum, titanium, magnesium, and nickel with several alloying elements available for each base component. These databases include thermodynamic and physical property parameters required for the calculation of phase diagrams.

Pandat™ was a successful tool in the prediction of both microstructure and microsegregation for several multicomponent aluminum alloys undergoing dendritic solidification. The modified Scheil model used accounted for the effects of solid-state back diffusion, undercooling, and dendrite arm coarsening [37]. For comparison, the Scheil model and the lever rule calculations were completed.

Pandat™ was used in this study to determine the partition coefficients as well as the solidus and liquidus lines for Ti-6Al-4V alloys having varying oxygen and iron concentrations.

2.8 Experimental Techniques for Investigation of Segregation

Experimental techniques used to determine solidus and liquidus temperatures are discussed. These temperatures are then used in macrosegregation models. Two thermal analysis methods are discussed, differential thermal analysis and differential scanning calorimetry. Electron microprobe analysis and microhardness measurements are also discussed briefly.

2.8.1 Thermal Analysis

In order to model the solidification process of an alloy system (or to determine effects of alloying elements on the phase diagram), liquidus and solidus temperatures must be determined. Thermal analysis is commonly used to determine liquidus and solidus temperatures [38]. If several samples of different compositions are analyzed, the shape of the curves on the phase diagram can be determined [35]. Two thermal analysis methods, DTA and DSC are used to determine liquidus and solidus temperatures.

Differential thermal analysis (DTA) measures the temperature difference over time between a "reactive" sample and a "non-reactive" reference sample [38]. These two samples are subjected to the same heating and cooling cycles. A reactive sample is one that may exhibit a phase change due to applied heat. A material that does not exhibit a phase change in the analysis temperature range is used as the non-reactive or reference material.

The reference material should be very close in weight to that of the sample of interest. As stated before, the reference material should not transform in the temperature range of analysis. A "differential" thermocouple is used to measure the difference in temperature between the sample and reference material. One pair of the thermocouple wires is attached to the bottom of sample container and the other to the bottom of the

reference container [38]. The voltage is measured across two “screw” terminals to obtain a temperature for the sample and reference (Figure 7).

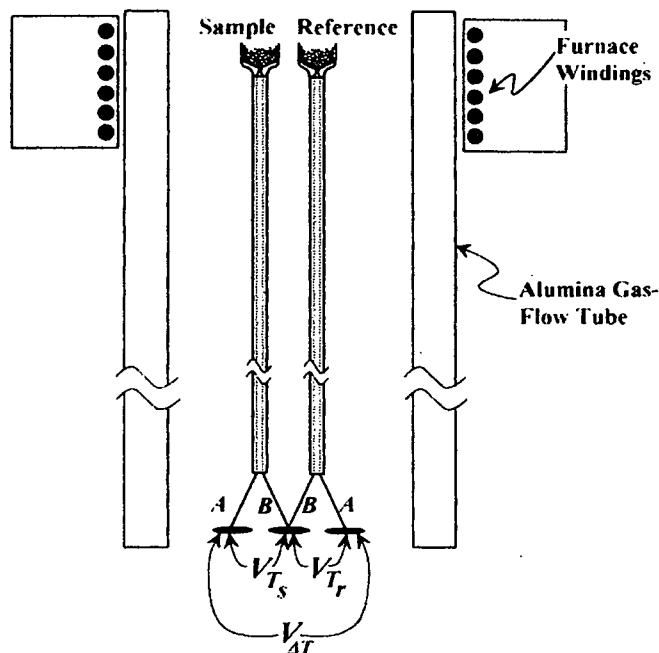


Figure 7. Schematic of a differential thermal analyzer [38].

If the sample exhibits a phase transformation during the analysis temperature cycle, the change is either endothermic or exothermic. During an endothermic transformation, the sample absorbs heat. During an exothermic transformation, the sample releases heat. A material in the solid phase must absorb heat in order to melt because the material needs energy to complete the phase transformation [38]. Thus, a solid material exhibits an endothermic change during melting.

The DTA and DSC traces, graphical results, have a distinct shape for melting transitions (Figure 8). The solidus temperature for titanium and titanium alloys is easily determined from the DTA trace of a fully melted and cooled sample. The liquidus temperature, however, is a nontrivial measurement.

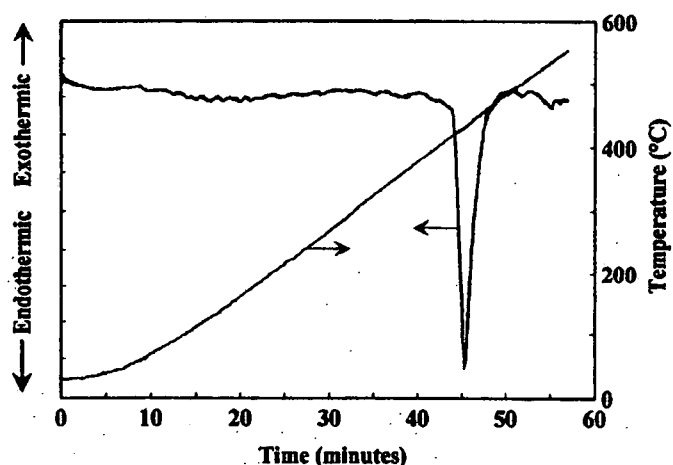


Figure 8. DTA trace for the melting of zinc in an argon atmosphere, heated at a rate of 10°C/min. [38]

Differential scanning calorimetry (DSC) provides similar information to DTA. The main difference is that a DSC instrument can more accurately measure energy of a phase change [38]. Like DTA, the sample and reference material are placed in separate containers. DSC, however, uses separate heating sources for each, and platinum wires are used instead of thermocouples. The resistance of the wires is measured and used to determine the temperature of the sample and reference [38].

In DSC, both samples are enclosed in a chamber capable of quick cooling. The cooling medium is usually flowing water or air. Once the specimens are enclosed, equal heat is provided to the sample and reference containers. As a transformation occurs within the sample, its temperature differs from that of the reference material. The DSC apparatus works to maintain a zero temperature difference between the two samples. The machine increases heat flow to one heat source while decreasing heat flow to the opposite source. This zero temperature difference between sample and reference is often termed the "null balance" [38].

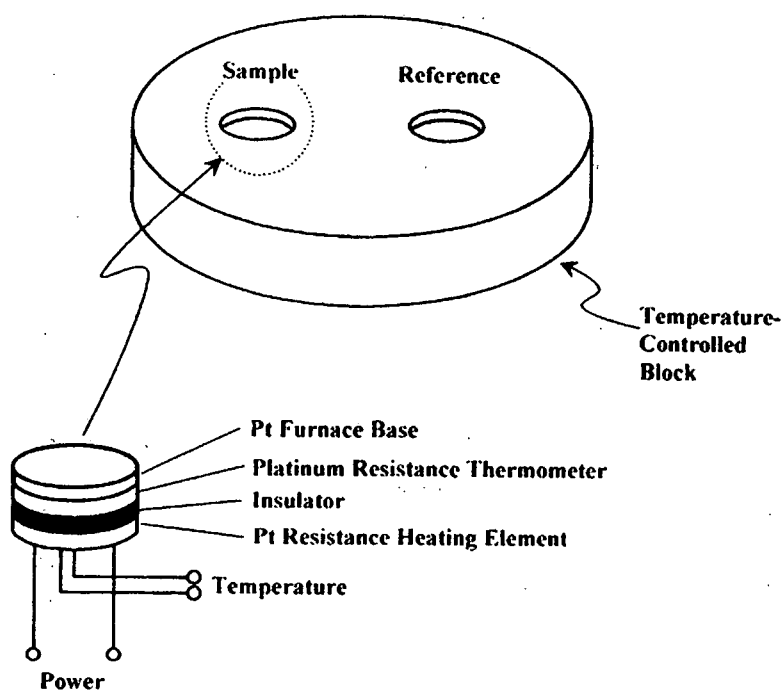


Figure 9. Schematic of a power-compensated differential scanning calorimeter [38].

For analytical purposes, the amount of energy added to the heating sources beyond that required to maintain the desired temperature cycle is assumed to be proportional to the heat released/absorbed by the sample. Both quantities are on a unit time basis [38].

A DTA instrument is used to measure the temperature at which a transformation occurs. It is, however, difficult to measure heat expelled or absorbed due to that transition with a DTA instrument. This difficulty arises from various temperature profiles that develop within a sample due to the shape of the container [39]. In other words, material at the surfaces of the crucible may not be at the same temperature as material at the crucible center.

2.8.1.1 Interpretation of Thermal Analysis Curves

Solidus temperatures (melt onset temperatures) are typically determined from DTA traces of fully melted samples (Figure 10).

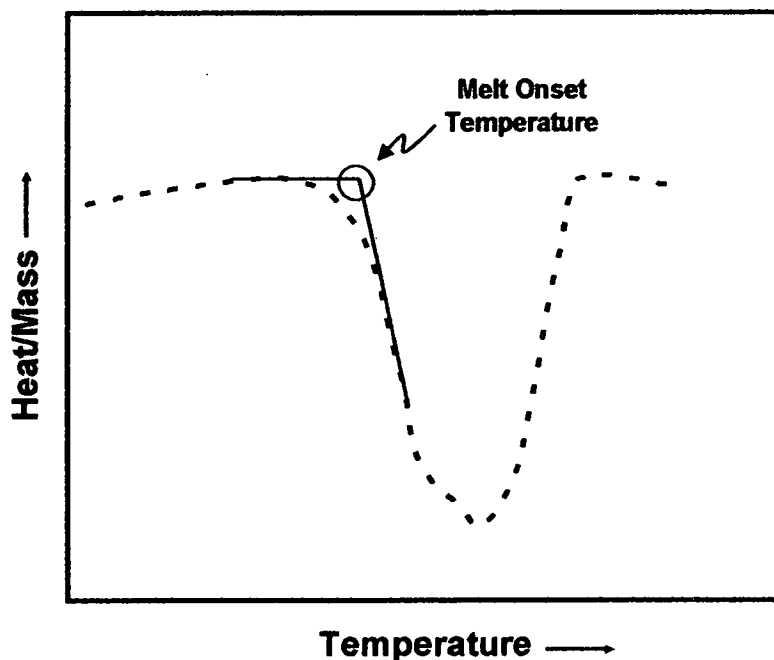


Figure 10. Sample DTA trace upon heating.

Liquidus temperatures are typically determined from continuous heat/cool cycles. (A sample is heated above the melting point at a constant rate and then cooled at a constant rate.) This method can lead to variable results due to sample non-uniformity and nonequilibrium solidification of alloy systems [40].

The liquidus temperature cannot be directly determined from a single melt. Several cycles of heating and cooling must be implemented, and then the liquidus can only be resolved to lie within a 1-2°C range [41] due to experimental limitations. While heating rate impacts both the solidus and liquidus temperatures, it is especially critical for finding the liquidus. A heating rate of 20 K/min would overshoot the liquidus because

too much energy would be entering the sample at a given time. The measurement would not be as close to the actual liquidus than if the heating rate was slower. Alternately, if the sample was heated or cooled very slowly the difference between the sample and reference would not be large enough for instrument detection.

Whether the liquidus range had been reached was determined from the cooling exotherm. If the sample did not fully melt upon heating, the cooling curve indicates an exothermic reaction immediately upon cooling. A cooling curve that flattens prior to exothermic reaction indicates undercooling and complete melting. The liquidus falls between the temperature at which complete melting is observed and that at which the sample does not fully melt (Figure 11).

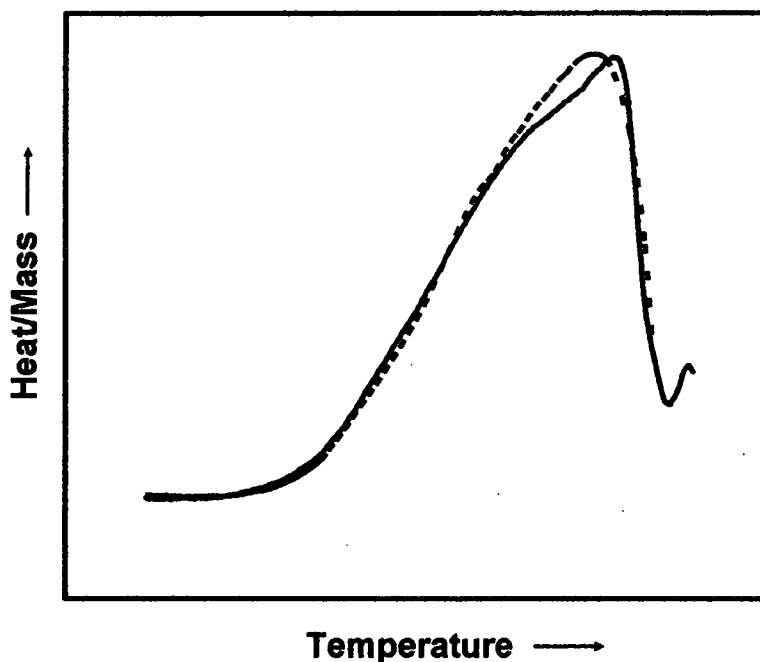


Figure 11. Sample DTA trace upon cooling. The solid line indicates complete melting (at a temperature above the liquidus), and the dotted line indicates incomplete melting (at a temperature below the liquidus). The actual liquidus temperature falls between the two cooling curves.

A possible explanation for flattening of a DTA cooling curve after complete melting is that a degree of undercooling is observed. Undercooling occurs when the liquid is cooled below a transition temperature without occurrence of that transition. Alternatively, a DTA cooling curve that spikes may indicate the presence of a nucleus. For this case, undercooling is not necessary since growth could begin on an existing nucleus.

2.8.2 Electron Microprobe Analysis

An electron microscope contains an electron microprobe analyzer that can produce a stable beam of electrons. This stable beam of electrons can remain focused on a single point on a solid specimen. The microprobe differs from normal operation of scanning electron microscopy in which the beam is rastered across the surface of a sample [42].

A microprobe provides information about the chemical composition of solid samples by either wavelength-dispersive spectrometry (WDS) or energy-dispersive spectrometry. WDS provides a very exact chemical analysis on tiny (1-2 microns in diameter) sections of the sample. EDS describes the amount and location of a component in a sample rather quickly. EDS does not provide the highly accurate composition information that WDS provides, however, WDS analysis is significantly more time consuming than EDS [42].

2.8.3 Microindentation Hardness Measurements

Microindentation hardness testing is generally performed on small or thin specimens to determine hardness characteristics of a material [43]. An indentation is made on the sample surface using an indenter with a pre-specified load. Knoop or Vickers hardness indenters can be employed. The size of the indentation is measured

and compared to standard tables to arrive at a microhardness value. Several measurements are taken to eliminate statistically significant errors. The microindentation hardness value of post-processed material was determined and compared to that of the as-received material to verify that contamination did not occur during processing. A standard is also tested to confirm the accuracy of the tester.

2.9 Research Issues/Objectives

There are several issues involved with determination and prediction of macrosegregation in Ti-6Al-4V and other titanium alloys. Accurate phase equilibria properties are needed for segregation calculations. These properties include solidus and liquidus temperatures as well as higher order phase diagrams. Thermophysical properties, like permeability are also needed. Relationships need to be developed between initial ingot concentration and casting parameters with the resulting macrosegregation. Also titanium is extremely reactive making experimental work especially difficult.

The objectives of this research were divided into three focal areas, characterization, ingot investigation, and segregation modeling. The goal of the characterization study was to determine the impact of iron and oxygen content on the freezing range of Ti-6Al-4V alloys. The purpose of the ingot investigation was determination of segregation trends in ingots following casting. Segregation models were examined to determine sensitive parameters and usefulness of models for segregation prediction.

To fulfill the objective of the characterization study, Ti-6Al-4V buttons with varying oxygen and iron contents were melted. These buttons were extreme cases with compositions that bracket that of the actual production alloy. A baseline material, with a composition similar to industry, was used for comparison. Wet chemical analysis was

performed to determine the actual composition of each button. Differential thermal analysis was performed to obtain the necessary phase equilibria data for segregation calculations. Following thermal analysis, samples were analyzed for contamination using scanning electron microscopy, energy-dispersive spectrometry, electron microprobe analysis, and microhardness testing. Thermodynamic calculations were performed to predict freezing ranges and partition coefficients. The calculations were validated with the results of DTA testing.

For the ingot investigation, samples at different radial and axial positions were taken from a cross-section of a Ti-6Al-4V round ingot. Wet chemical analysis was performed on each sample to obtain an average composition for the location within the ingot slab. Samples from axial and radial positions were also sectioned from equiaxed Ti-6Al-4V laboratory-scale ingots. Electron microprobe analysis was employed to establish segregation patterns. Small-scale ingots were also examined.

Segregation modeling was completed using the Lever Rule, Scheil equation, and the local solute redistribution equations. Calculations were completed using phase equilibria data from the literature, DTA results, and thermodynamic calculations.

CHAPTER III

MATERIALS AND EXPERIMENTAL PROCEDURES

The materials and procedures utilized in experimentation are outlined in this chapter. The button melts and baseline material were used to gain insight on the melting range of various Ti-6Al-4V alloys via differential thermal analysis. Ingot slabs were used to obtain segregation measurements from actual full-scale production material. A small-scale ingot was used to mimic segregation in large-scale production.

3.1 Button Melts and Baseline Material

The characterization experiments are discussed in this section. Ten Ti-6Al-4V buttons having different concentrations of iron and oxygen were melted. A baseline material, with composition typical to industry, was chosen for comparison. Wet chemical analysis was performed to determine the composition of each button melt and the baseline material. Differential thermal analysis (DTA) was performed to determine solidus and liquidus temperatures of the various alloys. The samples were sectioned and prepared for microscopy using standard metallographic techniques. Backscatter electron image (BEI) micrographs were taken using a scanning electron microscope (SEM) to establish as-received and post-DTA microstructures. Energy-dispersive spectrometry (EDS) and wavelength-dispersive spectrometry (WDS) were performed to verify sample purity following thermal analysis. Microindentation hardness testing was performed to compare hardness values of as-received material to that of thermal analysis specimens.

Thermodynamic calculations were performed and validated with the results of DTA testing.

3.1.1 Starting Material

A domestic titanium supplier vacuum arc melted ten Ti-6Al-4V buttons of different iron and oxygen contents. Five levels of iron were chosen; 0.0, 0.1, 0.2, 0.3, and 0.4 weight percent. Two levels of oxygen were chosen; 0.1 and 0.2 weight percent. Other alloying elements were kept at nominal values. The buttons weighed approximately 250g. Samples for chemical and thermal analysis were sectioned from the center area of each button.

Hot-rolled Ti-6Al-4V plate material was utilized as a baseline for comparison to the ten alloys. The composition of this material was close to industry standards.

3.1.2 Wet Chemical Analysis

Wet chemical analysis was performed by Chemsys, Incorporated (Dayton, Ohio) to verify button and baseline compositions. Aluminum, vanadium, and carbon contents were established via atomic absorption spectrometry. An inductively-coupled plasma-optical emission spectrometer (ICP-OES) was used to determine iron, nickel, and copper content. Oxygen and nitrogen were quantified via a Leco TC500 oxygen/nitrogen analyzer and hydrogen via a Leco RH404 hydrogen analyzer.

3.1.3 Differential Thermal Analysis

A differential thermal analysis (DTA) instrument was used to determine solidus and liquidus temperatures for Ti-6Al-4V alloys containing different concentrations of iron and oxygen. The baseline material was also tested for comparison.

A Netzsch STA 409 CD was used to perform differential thermal analysis on the Ti-6Al-4V alloys. Analysis was carried out in a helium-regulated atmosphere. The helium was 99.99999 percent pure (with water, oxygen, and total hydrocarbons present in amounts less than 2, 1, and 1 ppm each, respectively). The thermocouple used for temperature measurements was (tungsten-3 pct rhenium) vs (tungsten-25 pct rhenium). Temperature calibration was completed, using standards with known melting points, each time the sample carrier was exchanged. Y_2O_3 powders were used as the reference material. Samples and reference material were contained in solid Y_2O_3 (99.9 percent pure) crucibles. The samples were approximately 1.5 mm by 3 mm by 3 mm in size and 100 mg in weight. Samples were cleaned in acetone or ethanol and buried in Y_2O_3 powders inside the crucibles.

The solidus temperatures were determined from DTA traces of fully melted samples (Figure 9). Samples were heated to 1705°C, and the melt onset was determined using Proteus® analysis software.

An incremental trial-and-error test was used to pinpoint the liquidus range. Initially, complete melting was achieved by heating to 1705°C. The sample was then cooled well below the solidus temperature. Next, the sample was heated to a temperature between melt onset and 1705°C. The sample was allowed to equilibrate by maintaining temperature for 60 seconds. The sample was again cooled below the onset temperature. The cycle was repeated, decreasing the specified temperature by one or five degree(s) each cycle. "Five-degree" trials were implemented to establish a liquidus range quickly, and "one-degree" trials were used to narrow the range. See Appendix C for an example DTA heating scheme.

3.1.4 Metallographic Preparation

Following thermal analysis, samples were sectioned into two approximately equal pieces. One half of each sample was mounted in conductive mounting material with the cut surface exposed. Samples were ground using silicon carbide papers of grit sizes 200, 320, 400, and 600. Polishing steps included 9 μm , 6 μm , 3 μm , and 1 μm diamond pastes. Final polish was completed using colloidal silica. After completion of metallographic preparation, samples were cleaned for microscopy.

3.1.5 Scanning Electron Microscopy

Scanning electron microscope (SEM) backscattered electron image (BEI) micrographs were shot to determine microstructure changes resulting from differential thermal analysis (DTA) testing. Images were taken at magnifications of 500 and 1000 times at center and edge locations of each post-DTA sample. Images of as-received material were not taken in specific locations due to material homogeneity. Microscope settings included emission high tension (EHT) at 15.0 kV, probe current at 1 nA, and a working distance of 15 mm.

3.1.6 Energy-Dispersive Spectrometry

Energy-dispersive spectrometry (EDS) was utilized to qualitatively determine if the samples became contaminated during DTA testing. This analysis was performed using a SEM with EHT set at 20 kV, probe current at 1 nA, and a working distance of 25 mm. Testing was completed at center, edge, and impurity locations.

3.1.7 Electron Probe Microanalysis

Wavelength-dispersive spectrometry (WDS) was performed to confirm sample composition following DTA testing. Wet chemical analysis methods were not used due to

the small sample size. These compositions were established via electron probe microanalysis (EPMA) in a JEOL Superprobe 733. Measurements were taken at several locations on the sample surface and averaged. A beam spot size of 20 μm was employed.

3.1.8 Microindentation Hardness Measurements

After micrographs were taken and chemical composition determined, microindentation hardness measurements were completed using a Buehler Micromet 2100 Microhardness Tester with an applied load of 100 g. A Knoop indenter was employed, and testing was completed at center and edge locations. Microindentation hardness measurements of post-processed and as-received material were compared to determine if contamination occurred during thermal analysis. Standards were also tested to determine the accuracy of the apparatus.

3.1.9 Thermodynamic Modeling

The goal of the thermodynamic modeling was to predict the freezing range and partition coefficients for each Ti-6Al-4V alloy, using alloy composition, Gibbs free energy, etc. These calculations were performed by CompuTherm LLC, using PandatTM software. Thermodynamic input parameters were obtained from PanTitanium database [44], and composition data were taken from wet chemical analysis results.

3.2 Production-Scale Ingots

The production-scale experiments were performed on a Ti-6Al-4V VAR ingot. Wet chemical analysis was performed to determine the segregation patterns from the outer radius to the ingot center. Segregation calculations were performed to establish model accuracy in production-scale applications.

3.2.1 Material and Sectioning

The starting material was a 915 mm diameter Ti-6Al-4V VAR ingot. The ingot was sectioned into two halves along the axis of rotation. An axial plate, 50 mm thick, was sliced off one of the two halves and cut into six pieces. These six slabs were approximately the same size and contained the grain structure across the ingot center. Slabs on the left side of the axial plate were examined. The slabs were labeled A, C, and E for top, middle, and bottom, respectively. Samples for wet chemical analysis were sectioned from center, mid and outer radius at selected heights of each slab. The columnar zone on the middle and bottom slabs was examined as well.

3.2.2 Wet Chemical Analysis

Wet chemical analysis was performed by Chemsys, Incorporated (Dayton, Ohio) on the three slabs on the left side of the axial ingot plate. Aluminum, vanadium, and carbon contents were established via atomic absorption spectrometry. An inductively-coupled plasma-optical emission spectrometer (ICP-OES) was used to determine iron, nickel, and copper content. Oxygen and nitrogen were quantified via a Leco TC500 oxygen/nitrogen analyzer and hydrogen via a Leco RH404 hydrogen analyzer.

3.3 Small-Scale Ingot

This section discusses the material used to imitate production-scale processes. Material sectioning, metallographic preparation, and electron probe microanalysis are also outlined.

3.3.1 Material and Sectioning

The starting material was an induction-skull melted ingot with an equiaxed solidification structure, 87 mm in diameter with a height of 257.25 mm. Casting details

can be found elsewhere [45]. The lab-scale ingots were sliced in half axially. Samples were sectioned along the entire radius just above and just below mid-height.

3.3.2 Metallographic Preparation

Samples were mounted in conductive mounting material and ground using silicon carbide papers of grit sizes 200, 320, 400, and 600. Polishing steps included 9 μm , 6 μm , 3 μm , and 1 μm diamond pastes. Final polish was completed using colloidal silica on a vibromet. After completion of metallographic preparation, samples were cleaned for microscopy.

3.3.3 Electron Probe Microanalysis

Wavelength-dispersive spectrometry (WDS) was performed to determine segregation from cast surface to ingot center. A spot size of 20 μm and a step size of 20 μm were employed.

CHAPTER IV

CHARACTERIZATION RESULTS AND DISCUSSION

Wet chemical analysis was performed to determine the initial composition of the button melts and baseline material. Freezing ranges of the button melts and baseline material were determined via differential thermal analysis. Scanning electron microscopy, energy-dispersive spectrometry, electron microprobe analysis, and microindentation hardness testing were performed to determine if contamination occurred during thermal analysis.

4.1 Wet Chemical Analysis

Wet chemical analysis was performed on each of the button melts as well as the baseline material (Table 1) prior to thermal analysis testing.

Table 1. Results of wet chemical analysis on as-received material. All values reported in weight percent except hydrogen. Hydrogen data reported in parts per million.

Sample ID	Al	V	Fe	O	N	H	C
XB3040	6.17	4.39	0.02	0.1010	0.0031	45.7	0.0104
XB3041	6.06	4.47	0.02	0.1900	0.0037	30.7	0.0103
XB3042	6.14	4.05	0.10	0.0957	0.0018	17.9	0.0157
XB3043	5.96	4.12	0.10	0.2000	0.0037	18.0	0.0142
XB3044	5.73	4.00	0.21	0.0965	0.0038	22.8	0.0164
XB3045	5.72	4.10	0.22	0.1830	0.0020	11.2	0.0112
XB3046	5.77	3.92	0.33	0.0885	0.0024	13.6	0.0126
XB3047	6.19	4.03	0.32	0.1830	0.0026	22.8	0.0222
XB3048	5.90	3.93	0.44	0.0980	0.0039	19.7	0.0112
XB3049	6.17	4.07	0.44	0.2490	0.0018	38.0	0.0110
baseline	6.16	3.87	0.15	0.2470	0.0110	87.1	0.0155

4.2 Differential Thermal Analysis

Solidus and liquidus temperatures were determined via differential thermal analysis for the baseline material and six of the ten Ti-6Al-4V alloys (Figures 12-15). The vertical lines (Figures 12-15) indicate the range of the results. These vertical lines are not error bars. Due to time/equipment constraints, freezing ranges of alloys XB3042, XB3044, XB3046, and XB3047 were not determined. Refer to Appendix D for individual thermal analysis plots.

Freezing ranges varied for alloys having different iron and oxygen contents. For alloys having the same iron content (other solutes nominally the same), the alloy with the lower oxygen content had a larger freezing range (Figure 12). At 0.44 weight percent iron, oxygen content did not have a significant impact on the freezing range. Also, freezing range tended to increase with an increase in iron content. The two data points

at 0.15 weight percent iron (Figure 12) are possible outliers as they do not follow the trends of the other data. If the two points are not outliers, then definitive trends cannot be determined from the existing data set.

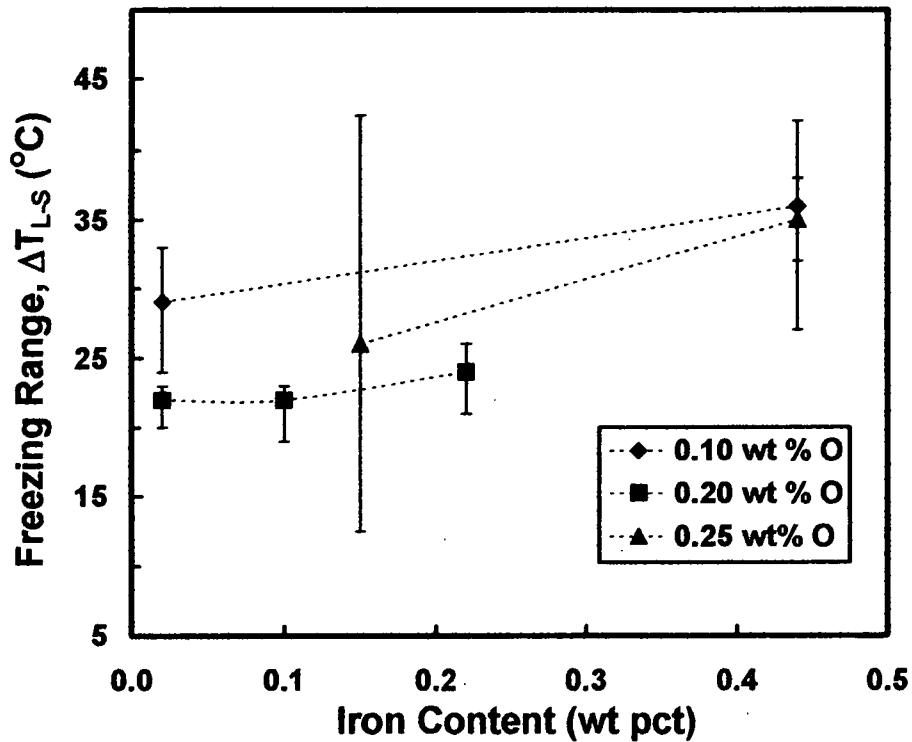


Figure 12. Measured freezing range as a function of iron content for Ti-6Al-4V alloys having different concentrations of iron and oxygen.

For alloys having the same oxygen content, the alloy with a higher iron concentration had a larger freezing range (Figure 13).

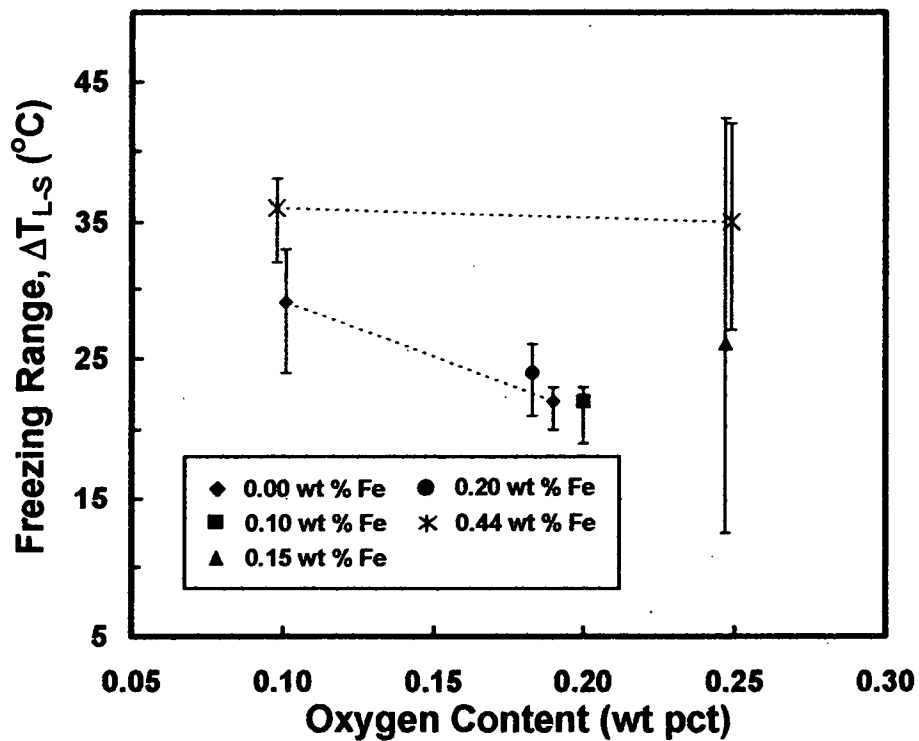


Figure 13. Measured freezing range as a function of oxygen content for Ti-6Al-4V alloys having different concentrations of iron and oxygen.

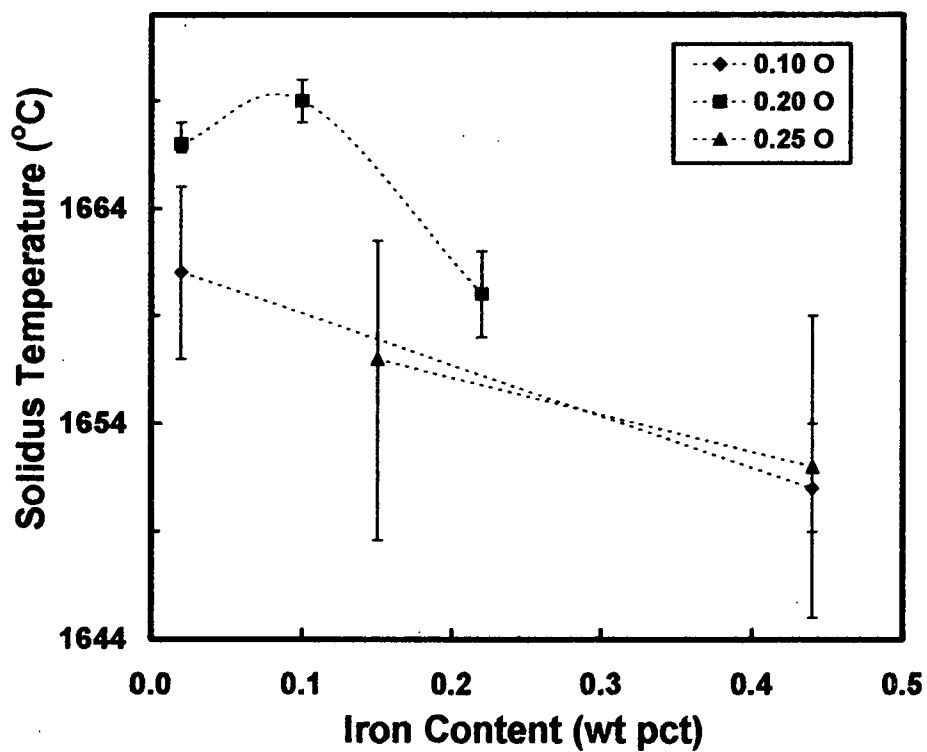


Figure 14. Solidus temperature as functions of iron content for Ti-6Al-4V alloys having different concentrations of iron and oxygen.

Solidus and liquidus temperatures also varied for alloys of different iron and oxygen content. For alloys having the same iron content, the alloy with a higher concentration of oxygen had the higher solidus temperature (Figure 14). The point at 0.15 weight percent iron and 0.25 weight percent oxygen is a possible outlier since it did not exhibit the same behavior as the other alloys. Also, oxygen content had no significant impact on solidus temperature for alloys having 0.44 weight percent iron. A definitive relationship between iron and oxygen content and liquidus temperature could not be determined. Alloys having the same iron content but different oxygen contents had very similar liquidus temperatures, except for the alloy at 0.15 weight percent iron. For example, 0.02 iron pair exhibited only a one-degree difference in liquidus temperature (Figure 15). This effect also occurred for the 0.44 iron alloy pair.

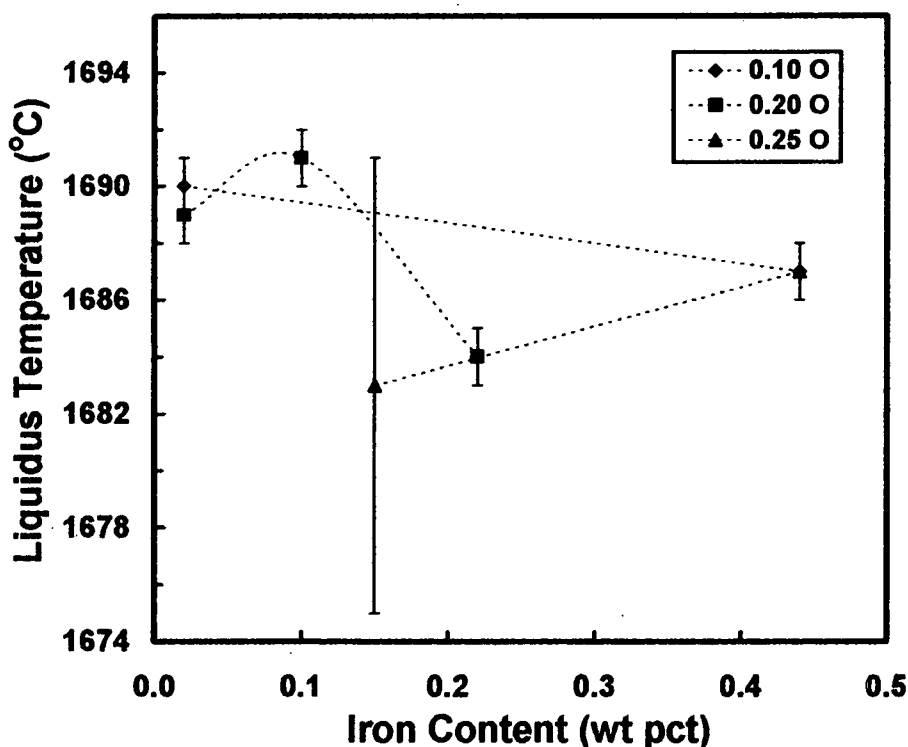


Figure 15. Liquidus temperatures as functions of iron content for Ti-6Al-4V alloys having different concentrations of iron and oxygen.

The liquidus temperatures determined by the traditional (cooling curve) method varied from those determined by the present method (incremental trial-and-error test) by up to ten degrees or more (Figure 16). This effect confirms the importance of reliable liquidus temperature determination procedures.

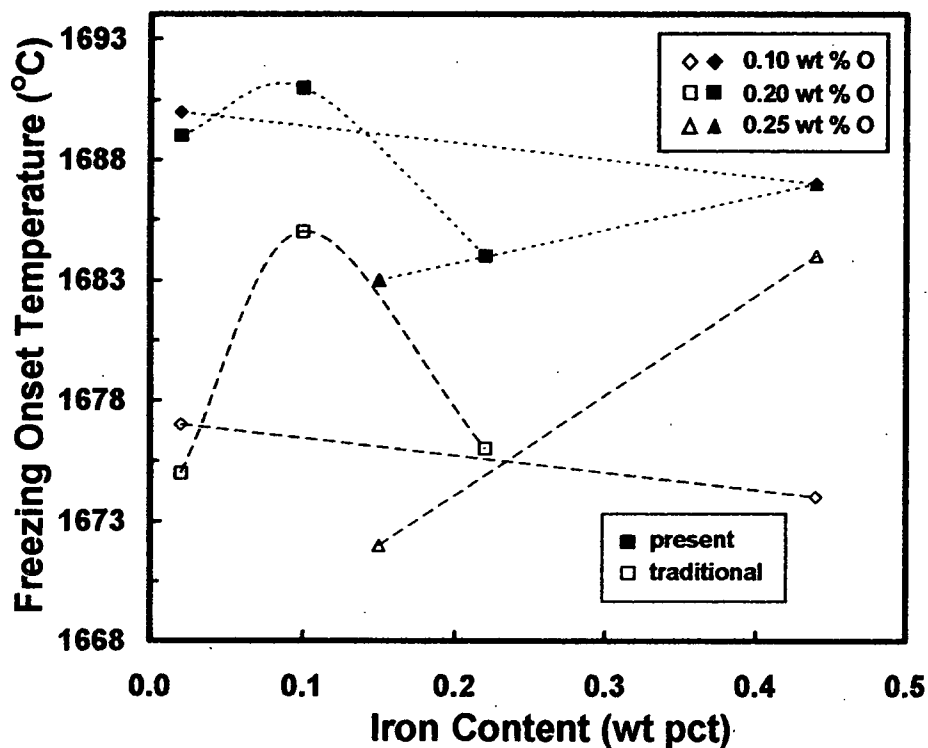


Figure 16. Comparison of present and traditional methods of determining the freezing onset or liquidus as a function of iron content

4.3 Scanning Electron Microscopy

Post-thermal analysis microstructures differed from those of the as-received material. The post-thermal analysis microstructures, however, were similar in morphology and scale from alloy to alloy. SEM backscattered electron images indicated that the structure was colony- or Widmanstätten (basketweave)-alpha. While small white impurities were scattered along the sample radius, there was no indication of oxygen

contamination at the edges (alpha case). Refer to Appendix E for a complete set of micrographs.

4.4 Energy-Dispersive Spectrometry

Energy-dispersive spectrometry (EDS) provided qualitative confirmation that the samples were essentially free of contamination. The results indicated that the small white impurities dispersed throughout the sample contained mainly yttrium and oxygen with a small amount of titanium. No other foreign material was apparent from this analysis.

4.5 Electron Probe Microanalysis

Electron probe microanalysis (EPMA) confirmed that thermal samples had little contamination. The results, however, also indicated an average aluminum loss of approximately 0.5-1.0-wt pct depending on the sample. The largest aluminum loss was 1.5-wt pct and represented a single sample. For a given temperature, aluminum has a higher vapor pressure than titanium [46] or vanadium. Thus aluminum will easily evaporate. Refer to Appendix F for a table of results.

4.6 Microindentation Hardness Measurements

Microindentation hardness testing established that the thermal analysis specimens had higher hardness values than did the as-received material. This effect, however, is reasonable since heat-treating changes material properties. Refer to Appendix G for complete results.

4.7 Thermodynamic Modeling

Thermodynamic modeling was comprised of two parts, initial calculations and aluminum loss calculations.

4.7.1 Initial Calculations

Thermal analysis measurements did not verify the thermodynamic calculations performed by CompuTherm, LLC [44]. Experimental freezing ranges were significantly lower than the calculated ranges (Figure 17&18). The freezing range of the baseline material was especially overestimated in the calculations, even if the possible outliers are included.

Measured and calculated freezing range trends varied from alloy to alloy. Trends in the data were similar except for the alloys having 0.25 weight percent oxygen (Figure 17). Experimental data indicated that the alloy with higher iron content would have a larger freezing range, while the calculations indicated that the alloy with higher iron content would have a lower freezing range. Refer to Appendix H for a table of actual values.

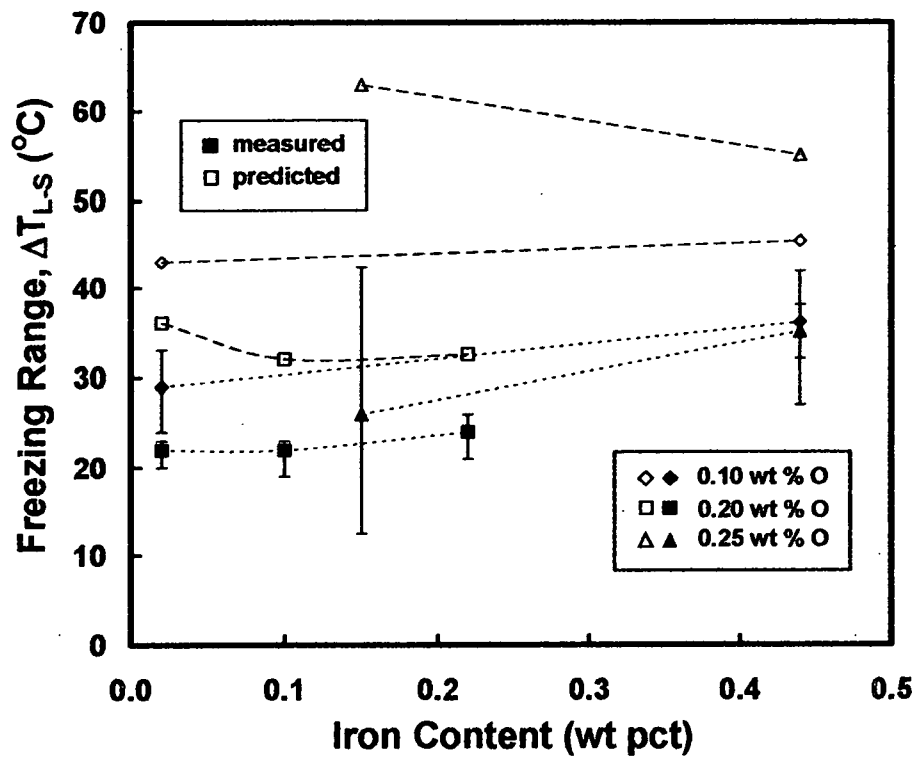


Figure 17. Comparison of measured and predicted [44] freezing range as a function of iron content.

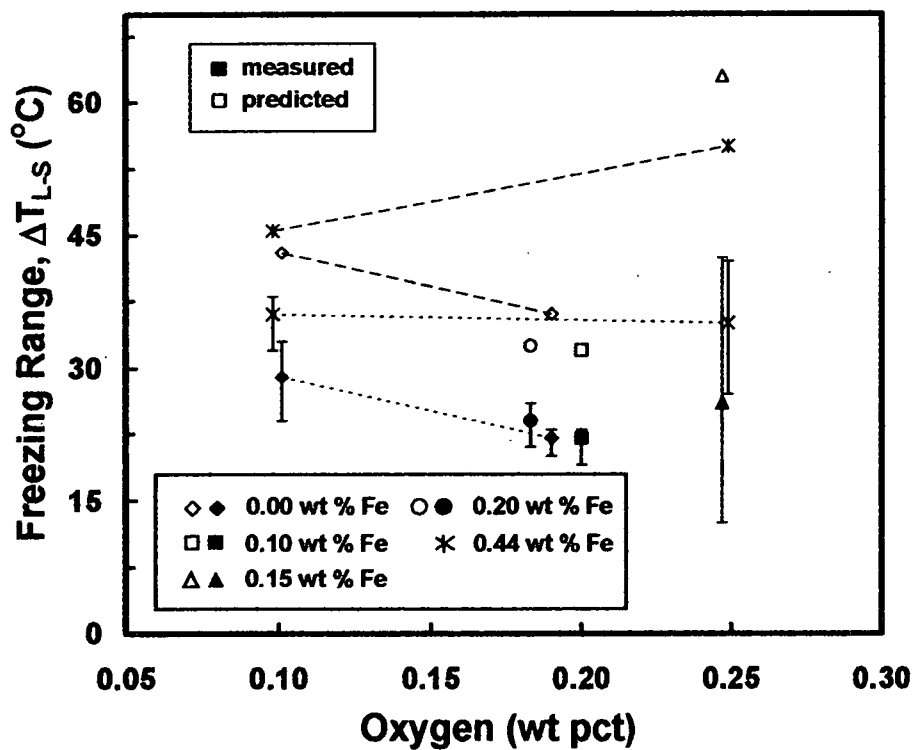


Figure 18. Comparison of measured and predicted [44] freezing range as a function of oxygen content.

4.7.2 Effect of Aluminum Evaporative Losses on Freezing Range Calculations

Thermodynamic calculations performed by CompuTherm, LLC, [44] established that loss of aluminum impacted the liquidus and solidus temperatures (Table 2). Alloys XB3040 and XB3049 were chosen for this investigation. Measured solidus and liquidus temperatures for alloy XB3040 were 1664°C and 1690°C, respectively (Figures 14&15). If the final aluminum concentration of alloy XB3040 was taken to be 4.55-wt pct (as determined via EMPA), then predicted and measured solidus temperatures had better agreement. I.e. the predicted solidus temperature for this alloy would lie between 1665°C and 1669°C, closer to 1664°C, the measured solidus value. Nevertheless, predicted liquidus values, and thus freezing ranges, were still much too large for this alloy.

Measured solidus and liquidus temperatures for alloy XB3049 were 1659°C and 1686°C, respectively. If the final aluminum concentration of alloy XB3049 was taken to be approximately 5.03 (as determined via EMPA), then predicted and measured solidus values had better agreement. Similar to alloy XB3040, the predicted liquidus value for alloy XB3049 was much too high.

Table 2. Results of the aluminum evaporative loss calculations [44].

Alloy	Al Content (wt pct)	Liquidus Temperature (°C)	Solidus Temperature (°C)	Freezing Range, Δ_{L-S} (°C)
XB3040 original	6.17	1715	1672	43
XB3040-5Al	5.00	1708	1669	39
XB3040-4Al	4.00	1701.5	1665	36.5
XB3049 original	6.17	1715	1660	55
XB3049-5Al	5.00	1710	1657	53
XB3049-4Al	4.00	1705.5	1653.5	52

4.8 Conclusions

Thermal analysis on Ti-6Al-4V button melts established that freezing range varied for alloys having different iron and oxygen content. A clear relationship between iron and oxygen content and the freezing range was not determined. SEM micrographs, EDS, and EMPA confirmed that the samples were not contaminated during thermal analysis. Accounting for aluminum loss, however, is a potential complication during thermal analysis. Microindentation hardness measurements indicated that post-thermal analysis samples had higher hardness values than as-received specimens. Thermal analysis measurements did not confirm the freezing range predictions of the thermodynamic calculations; however, some freezing range trends were similar. Still, the calculated solidus temperatures had better agreement with the consideration of aluminum losses. The calculated liquidus temperatures were still much higher than those measured via thermal analysis.

CHAPTER V

INGOT INVESTIGATION RESULTS

The results of the ingot investigation of ingot slabs and small-scale ingot halves are presented in this chapter. Wet chemical analysis was performed on three slabs of a Ti-6Al-4V VAR ingot having a mixed structure (columnar and equiaxed). Distribution of four solutes, aluminum, vanadium, iron, and oxygen, were plotted as a function of radial position. Iron and oxygen distribution were compared. Distribution of aluminum, vanadium, and iron, in the small-scale equiaxed ingot, were measured via electron microprobe analysis (EMPA) and plotted as a function of radial position.

5.1 Wet Chemical Analysis

Wet chemical analysis was performed on selected samples from each of the three ingot slabs (Tables 3-5) denoted as top, middle, and bottom or "A", "C," and "E," respectively.

Table 3. Wet chemical analysis results for the top ingot slab (slab "A"). All values are given in weight percent, except hydrogen which is given in parts per million.

ID	r/R	h/H	Al	V	Fe	O	N	H	C
1	0.89	0.94	6.06	4.02	0.23	0.245	0.013	16.2	0.0246
2	0.49	0.94	6.35	4.02	0.22	0.236	0.010	24.7	0.0272
3	0.09	0.94	6.23	4.10	0.22	0.220	0.011	15.7	0.0268
4	0.89	0.83	6.36	4.07	0.20	0.253	0.010	15.5	0.0230
5	0.49	0.83	6.07	4.02	0.22	0.229	0.011	24.6	0.0285
6	0.89	0.70	6.25	3.99	0.17	0.228	0.010	11.4	0.0234
7	0.49	0.70	6.25	4.11	0.21	0.221	0.009	14.6	0.0249
8	0.09	0.70	6.18	4.18	0.22	0.225	0.009	18.8	0.0243

Table 4. Wet chemical analysis results for the middle ingot slab (slab "C"). All values are given in weight percent, except hydrogen which is given in parts per million.

ID	r/R	h/H	Al	V	Fe	O	N	H	C
9	0.92	0.64	5.86	3.59	0.22	0.230	0.009	12.3	0.0283
10	0.52	0.64	6.04	3.82	0.21	0.210	0.008	28.9	0.0260
11	0.15	0.64	5.88	3.72	0.21	0.214	0.009	20.9	0.0272
12	0.92	0.51	6.10	3.74	0.20	0.229	0.007	14.6	0.0257
13	0.86	0.51	6.31	3.86	0.17	0.260	0.011	30.3	0.0258
14	0.80	0.51	6.56	3.95	0.17	0.251	0.010	46	0.0259
15	0.75	0.51	6.12	4.00	0.20	0.233	0.010	32.9	0.0276
16	0.58	0.51	6.00	3.98	0.20	0.229	0.011	25.3	0.0230
17	0.52	0.51	6.08	3.77	0.24	0.219	0.010	16.3	0.0262
18	0.15	0.51	6.11	3.76	0.20	0.205	0.008	28.8	0.0283
19	0.92	0.38	5.84	3.68	0.15	0.225	0.010	26.8	0.0247
20	0.52	0.38	6.08	3.72	0.21	0.212	0.009	19.7	0.0284
21	0.15	0.38	6.21	3.83	0.21	0.213	0.009	19.2	0.0258

Table 5. Wet chemical analysis results for the bottom ingot slab (slab "E"). All values are given in weight percent, except hydrogen which is given in parts per million.

ID	r/R	h/H	Al	V	Fe	O	N	H	C
22	0.88	0.32	6.36	3.85	0.13	0.223	0.0078	12.8	0.0204
23	0.47	0.32	6.18	3.95	0.22	0.202	0.0065	16.4	0.0273
24	0.06	0.32	6.30	3.94	0.20	0.203	0.0082	15.8	0.0264
25	0.88	0.20	6.36	3.96	0.16	0.227	0.0072	20.8	0.0206
26	0.47	0.20	6.13	4.01	0.18	0.210	0.0088	21.4	0.0263
27	0.06	0.20	6.24	4.01	0.18	0.226	0.0089	23.8	0.0234
28	0.88	0.04	6.07	3.95	0.18	0.218	0.0086	23.6	0.0212
29	0.47	0.04	6.00	3.76	0.15	0.230	0.0069	20.4	0.0242
30	0.06	0.04	6.19	3.69	0.15	0.237	0.0079	23.7	0.0198

5.2 Ingot Solute Distribution Plots

Aluminum, vanadium, iron, and oxygen distribution were plotted as a function of normalized radial position for the top, middle, and bottom ingot slabs. Three axial positions were investigated in each slab. Distribution was plotted with respect to overall ingot height. For example, 94 percent of ingot height (near the top) is denoted by 94% H.

5.2.1 Aluminum Distribution

Overall, aluminum distribution varied from slab to slab and within individual slabs. A slight decrease in aluminum concentration was observed from the edge (fraction of R equal to 1.0) of slab "A" to the center (fraction of R equal to 0.0), except for the very top of the ingot (Figure 19). A slight decrease in aluminum content from edge to center is reasonable behavior since the last material to solidify should be depleted in aluminum. Aluminum content increased from the edge to the end of the columnar zone at mid-

height of the entire ingot (Figure 20). The concentration increased from edge to center at the bottom of slab "C," opposite of expected behavior. For the bottom portion of the ingot (slab "E"), aluminum concentration decreased then increased at all three axial positions (Figure 21).

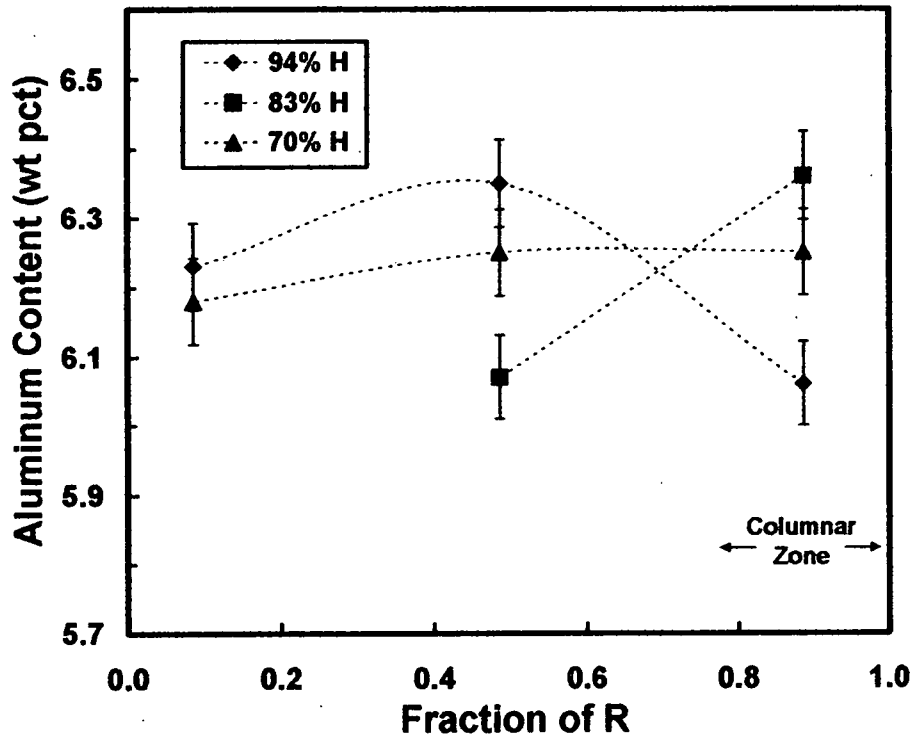


Figure 19. Aluminum radial distribution in Ti-6Al-4V ingot slab "A" as measured via wet chemical analysis.

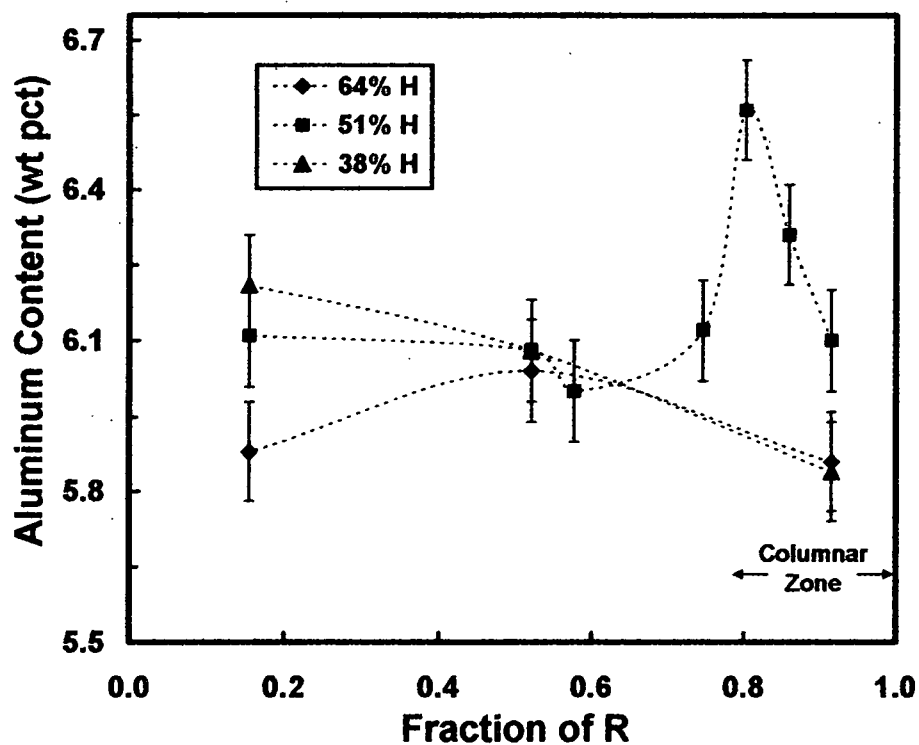


Figure 20. Aluminum radial distribution in Ti-6Al-4V ingot slab "C" as measured via wet chemical analysis.

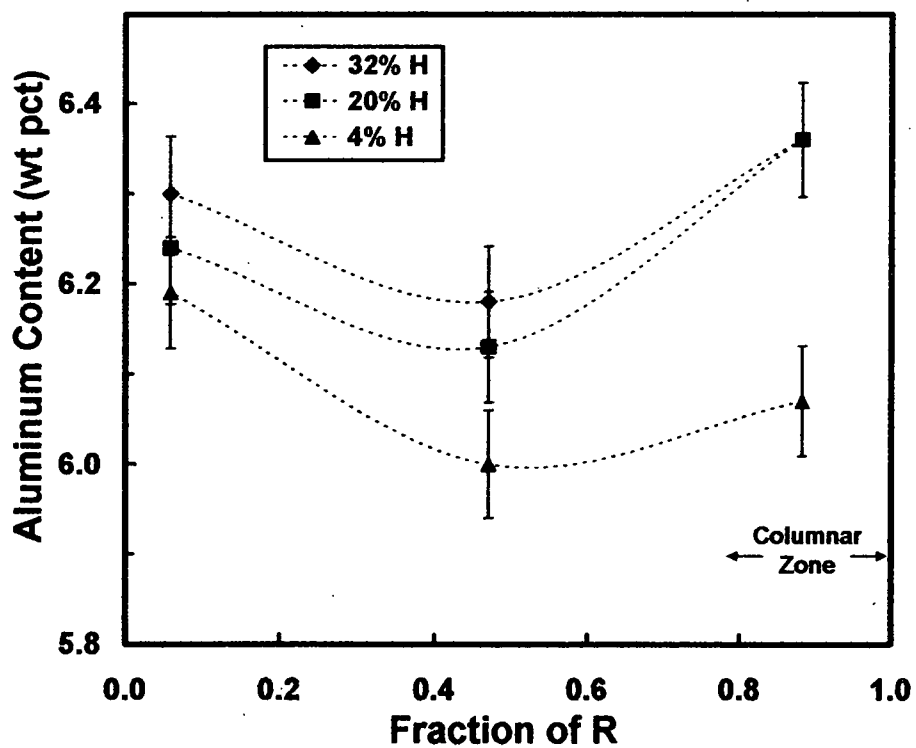


Figure 21. Aluminum radial distribution in Ti-6Al-4V ingot slab "E" as measured via wet chemical analysis.

5.2.2 Vanadium Distribution

Vanadium distribution varied from slab to slab and within individual slabs. Conclusive trends could not be observed for the top ingot slab. At 94 percent of ingot height (94% H), vanadium concentration was flat from edge to mid-radius and increased from mid-radius to ingot center (Figure 22). Vanadium concentration decreased from edge to mid-radius at 83 percent of ingot height, and at 70 percent of ingot height, vanadium content increased from edge to center. Vanadium content increased from ingot edge to the columnar zone end for mid-ingot height (Figure 23). Expected behavior, an increase in vanadium content, was observed along the bottom of slab "C" (Figure 23). The top of this slab, however, did not exhibit a conclusive trend. Two opposite trends were noticed across slab "E." Vanadium content increased across the top portion of this slab but decreased across the bottom (Figure 24).

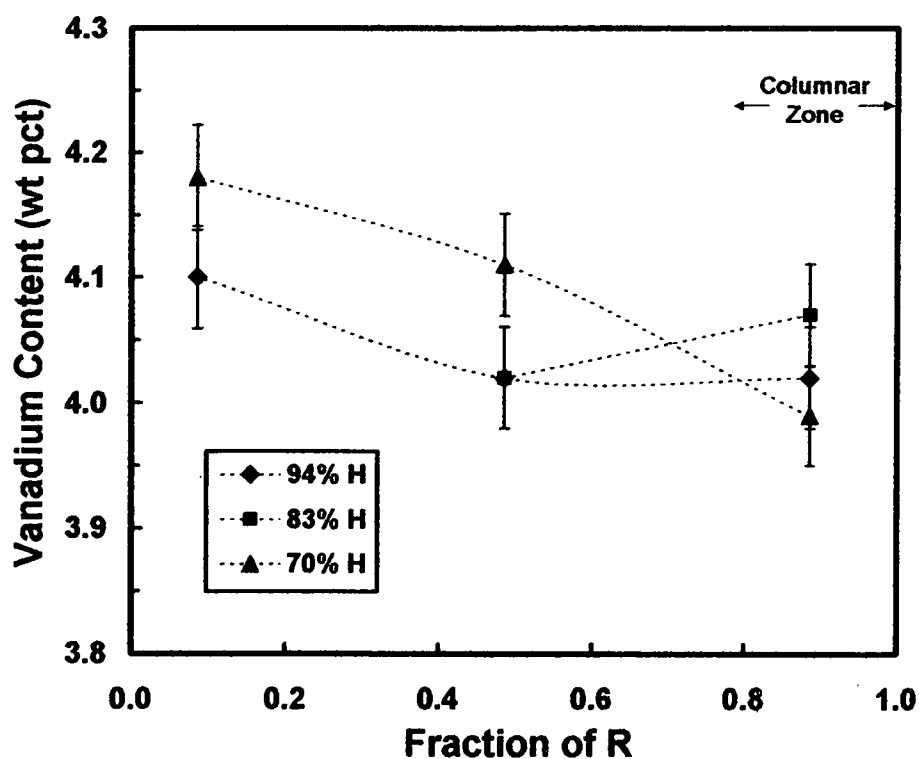


Figure 22. Vanadium radial distribution in Ti-6Al-4V ingot slab "A" as measured via wet chemical analysis.

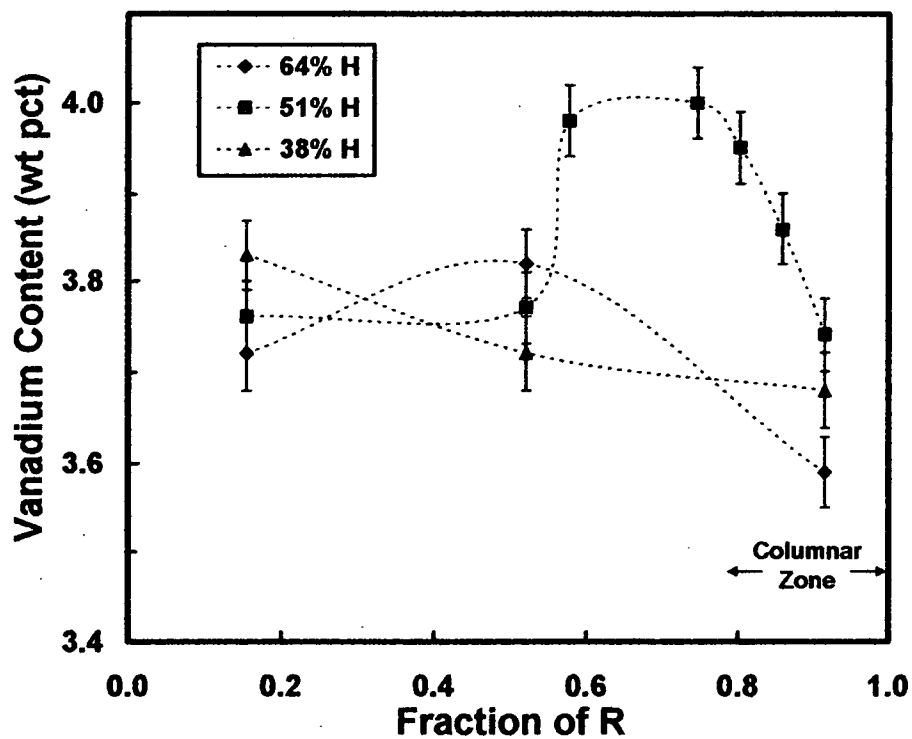


Figure 23. Vanadium radial distribution in Ti-6Al-4V ingot slab "C" as measured via wet chemical analysis.

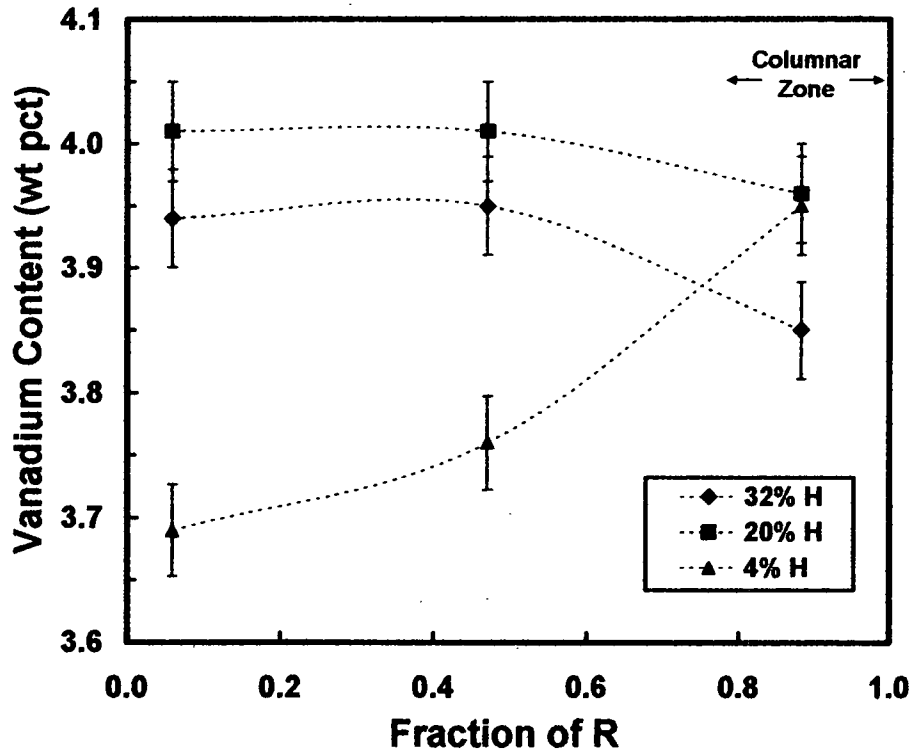


Figure 24. Vanadium radial distribution in Ti-6Al-4V ingot slab "E" as measured via wet chemical analysis.

5.2.3 Iron Distribution

Iron distribution varied from slab to slab and within individual slabs. At the top of the ingot (94% H) iron content decreased from ingot edge to center (Figure 25). Opposite behavior was observed at 83 and 70 percent ingot height. Iron content decreased through the columnar zone at mid-height of the ingot (Figure 26), but a definitive trend was not observed through the equiaxed zone. The other two axial positions investigated in slab "C" exhibited opposite trends. Iron content was observed to decrease in the very bottom portion of the ingot (Figure 27). At the other two axial positions (32% H and 20% H), iron concentration increased and then remained constant from mid-radius to center.

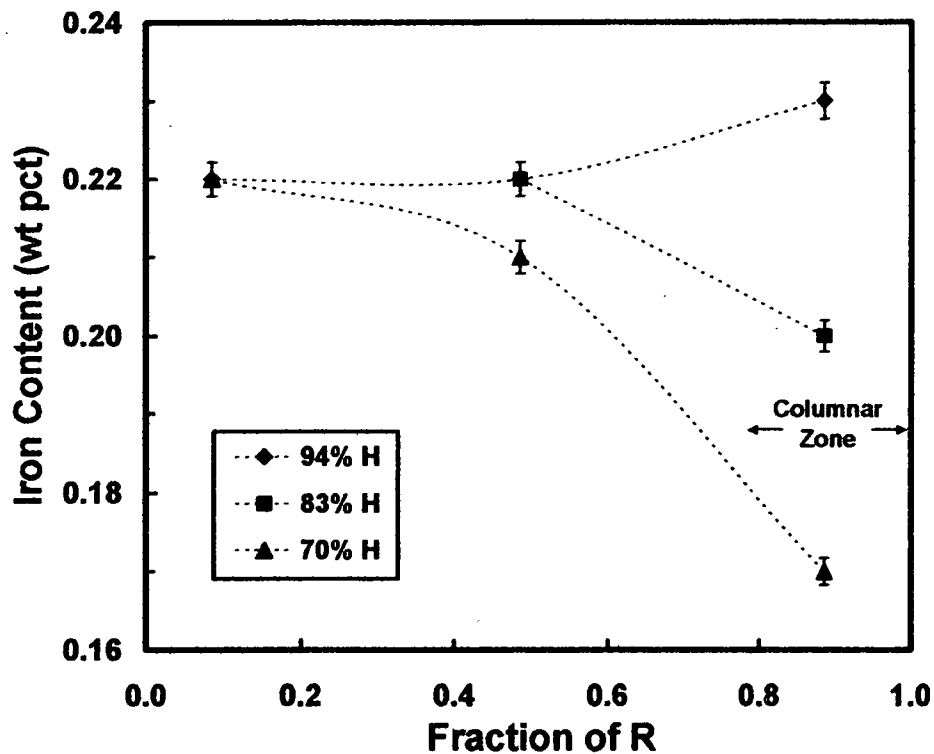


Figure 25. Iron radial distribution in Ti-6Al-4V ingot slab "A" as measured via wet chemical analysis.

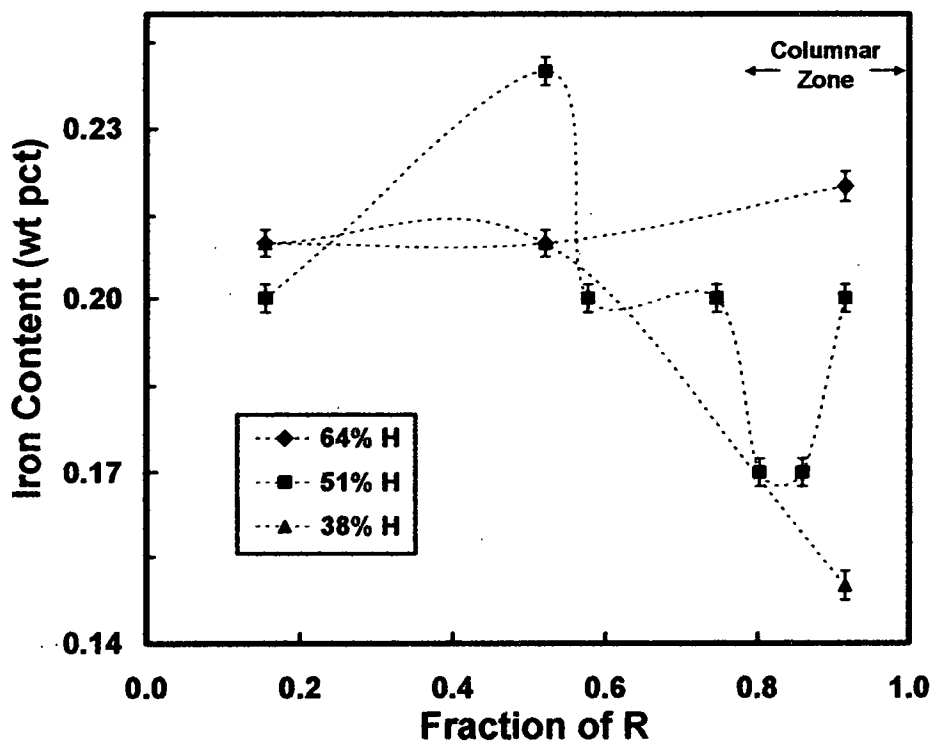


Figure 26. Iron radial distribution in Ti-6Al-4V ingot slab "C" as measured via wet chemical analysis.

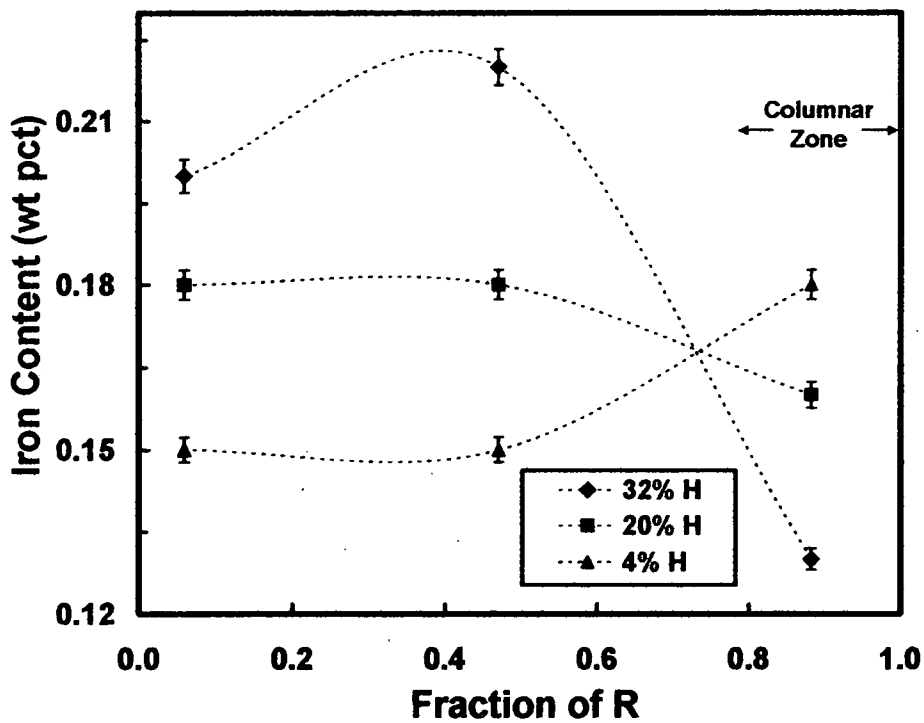


Figure 27. Iron radial distribution in Ti-6Al-4V ingot slab "E" as measured via wet chemical analysis.

5.2.4 Oxygen Distribution

Overall, oxygen tended to decrease from edge to center for all slabs, however, some discrepancies were observed in the top and bottom slabs. Oxygen content was higher at the edge than the center for the top portion (94% H and 83% H) of the ingot (Figure 28), expected behavior since oxygen-depleted material should be the last to solidify. A slight decrease then increase was observed at 70 percent ingot height. A slight increase in oxygen concentration through the columnar zone was observed at mid-height (51% H) of the ingot (Figure 29). Oxygen content tended to decrease from edge to center for slab "C" (Figure 29). Oxygen radial distribution varied for the three axial positions in slab "E" (Figure 30). At the top of the slab, oxygen content decreased from edge to center. The opposite effect was observed for the bottom portion of the ingot (4% height). In the middle of the slab "E," oxygen content increased and then decreased.

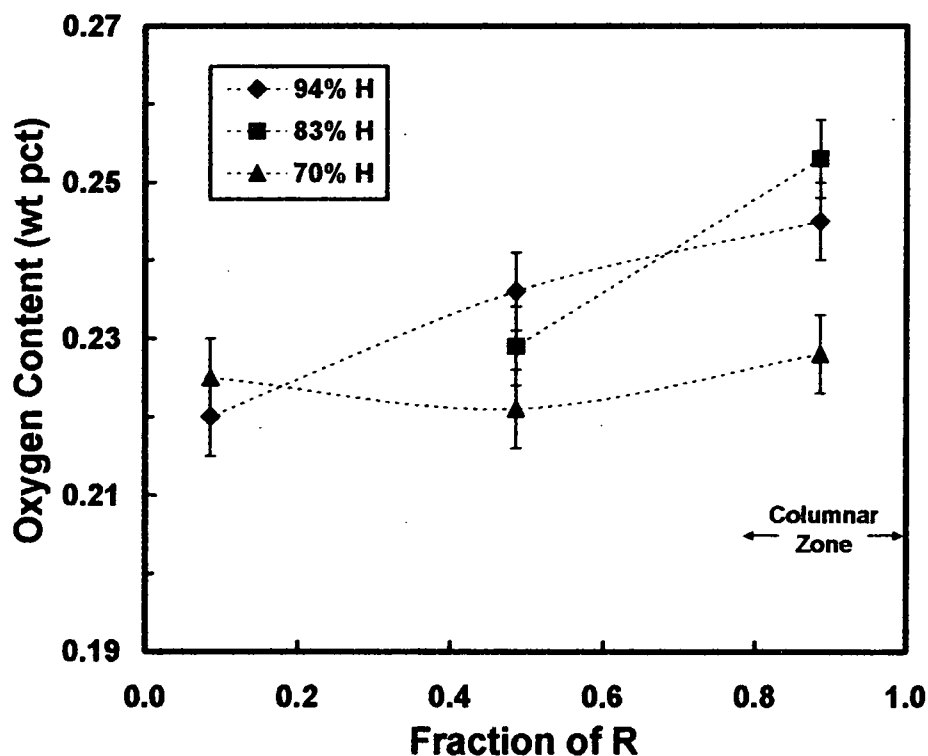


Figure 28. Oxygen radial distribution in Ti-6Al-4V ingot slab "A" as measured via wet chemical analysis.

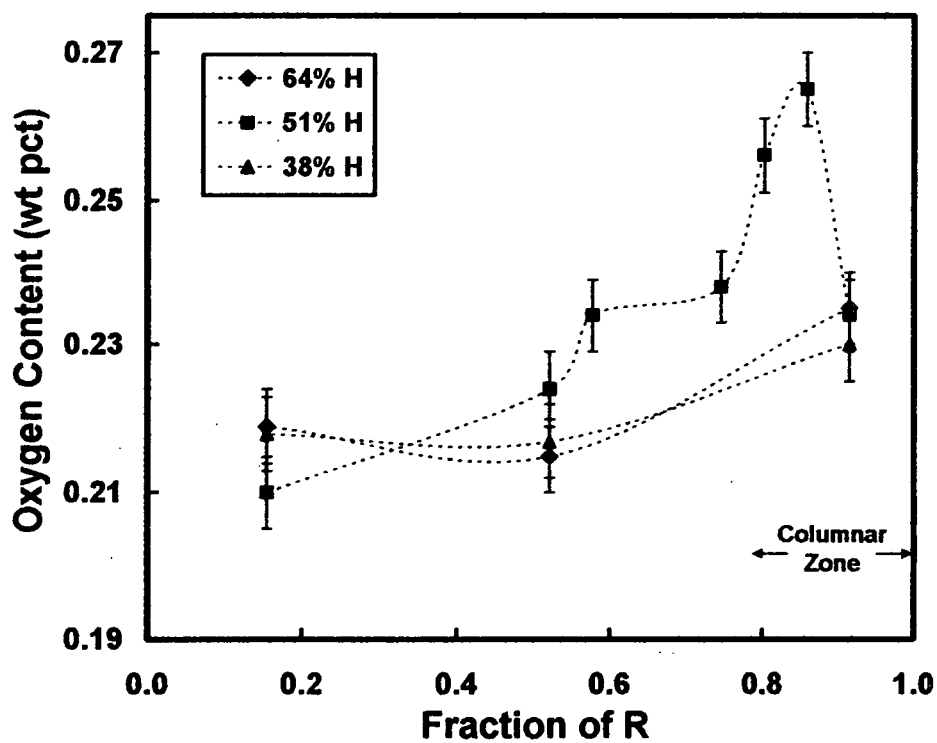


Figure 29. Oxygen radial distribution in Ti-6Al-4V ingot slab "C" as measured via wet chemical analysis.

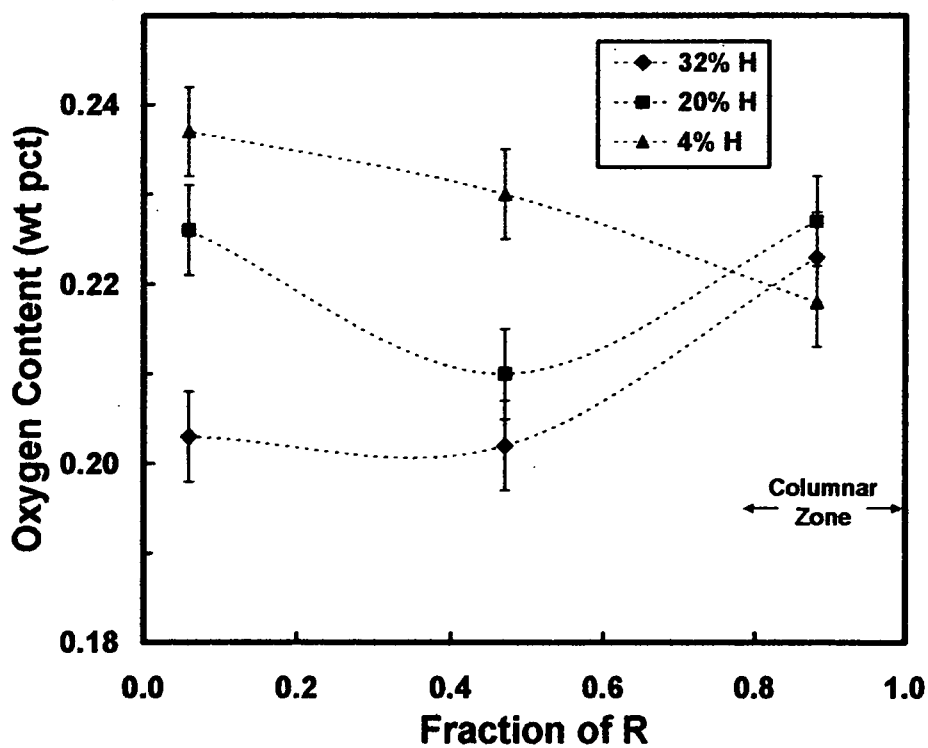


Figure 30. Oxygen radial distribution in Ti-6Al-4V ingot slab "E" as measured via wet chemical analysis.

5.2.5 Comparison of Iron and Oxygen Distribution

A definitive relationship between iron and oxygen radial distribution could not be established for the production-scale ingot. At 94 percent ingot height, similar behavior was observed for iron and oxygen while opposite behavior was established at 83 percent ingot height (Figures 25&28). Opposite behavior is expected since the solutes stabilize different phases. Again, opposite behavior was observed at 38 percent ingot height (Figures 26&29). At other axial locations radial distribution of iron and oxygen did not follow any clear patterns.

5.3 Small-Scale Ingot Solute Distribution

Measurements of solute concentrations in a small-scale ingot were taken along the radius at two axial locations via EMPA. Solutes investigated included aluminum, vanadium, and iron. The microprobe apparatus was not capable of determining oxygen content.

5.3.1 Aluminum Distribution

Overall, aluminum content decreased from edge (R equals 1.0) center (R equals 0.0) for both axial locations investigated (Figures 31-32). Some fluctuation, however, was observed in measurements taken between the edge and center. The trend of decreased aluminum content, from edge to center, is logical considering the binary partition coefficient found in the literature is less than unity.

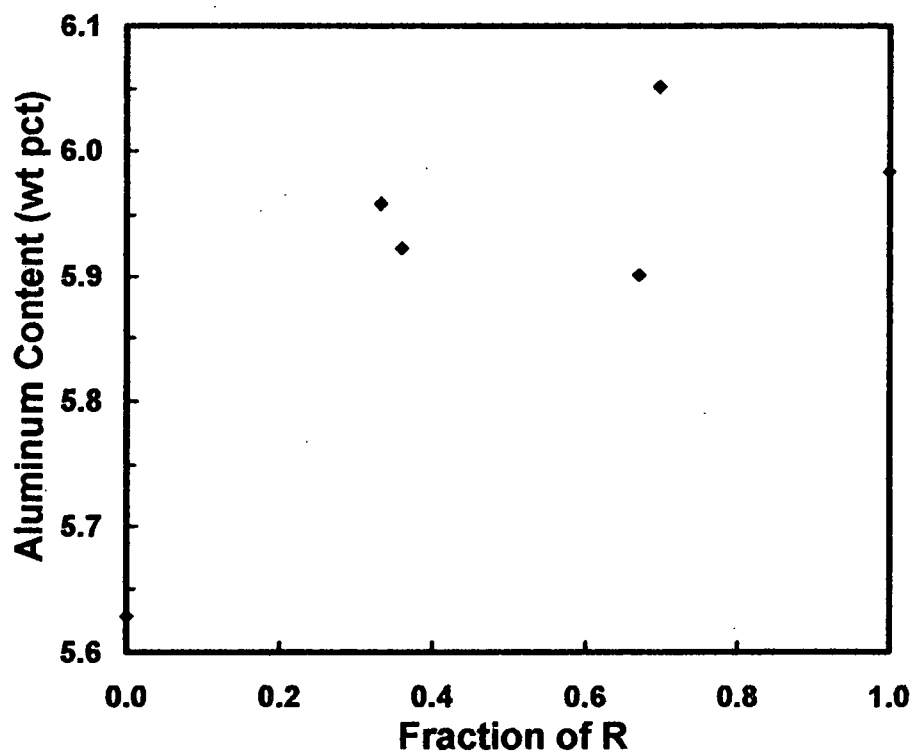


Figure 31. Aluminum radial distribution, just above mid-height, in a Ti-6Al-4V small-scale ingot.

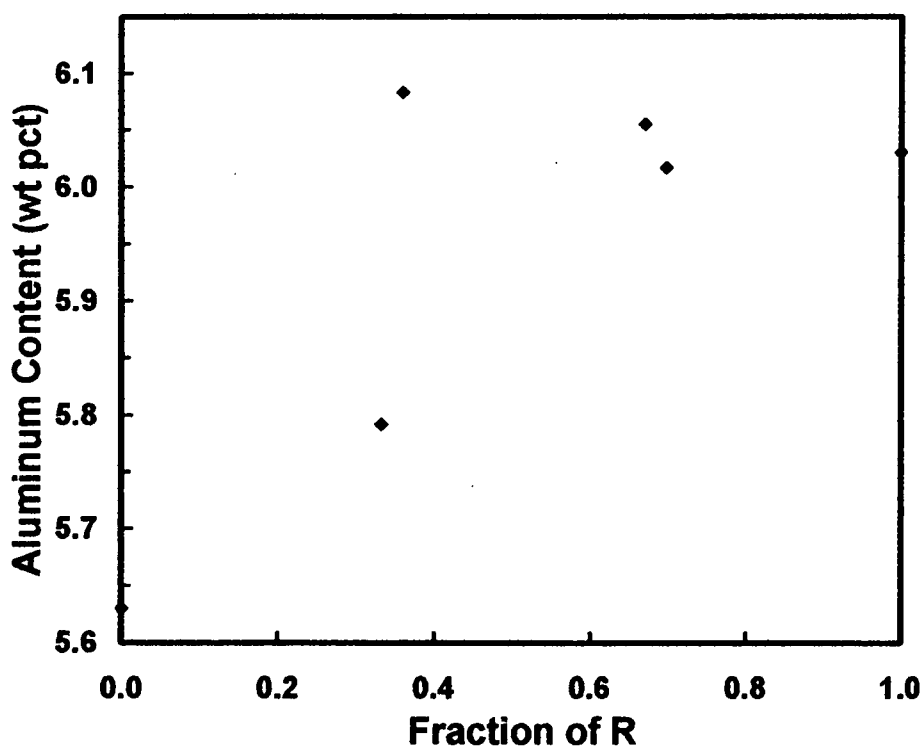


Figure 32. Aluminum radial distribution, just below mid-height, in a Ti-6Al-4V small-scale ingot.

5.3.2 Vanadium Distribution

Different trends in vanadium distribution were observed in the two axial locations investigated. A decrease in vanadium content was observed just above mid-height (Figure 33), while an increase was observed just below mid-height (Figure 34). At both positions, however, vanadium content increased and decreased significantly at a fraction of R approximately equal to 0.66. Vanadium content increased and decreased significantly at a fraction of R approximately equal to 0.37 for measurements taken just above mid-height (Figure 33). For a fraction of R equal to approximately 0.37, vanadium content levels out for measurements taken just below mid-height (Figure 34).

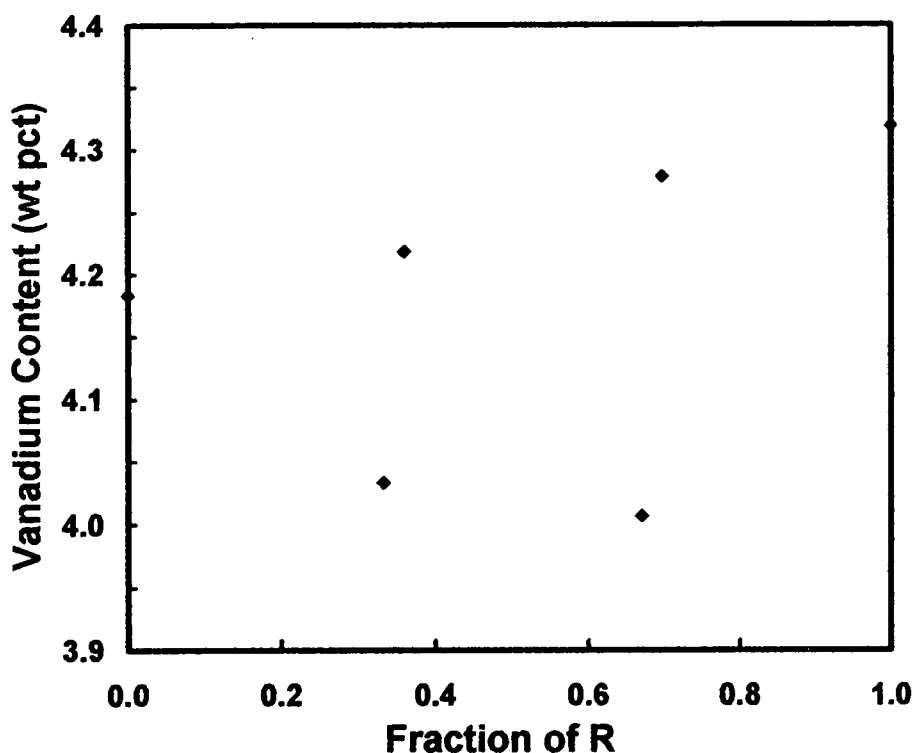


Figure 33. Vanadium radial distribution, just above mid-height, in a Ti-6Al-4V small-scale ingot.

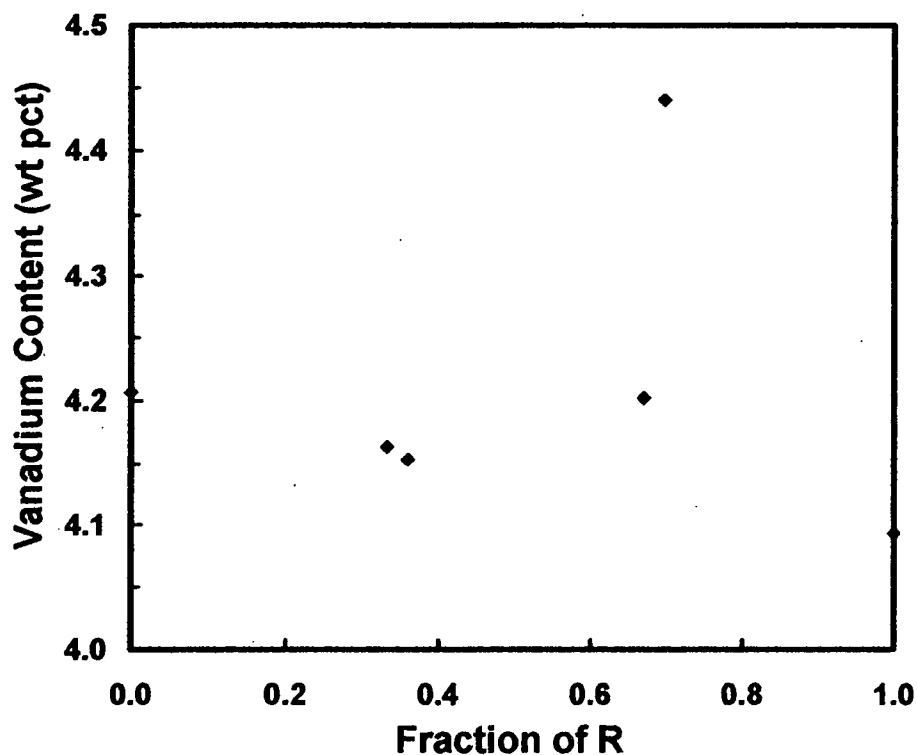


Figure 34. Vanadium radial distribution, just below mid-height, in a Ti-6Al-4V small-scale ingot.

5.3.3 Iron Distribution

Different trends in iron distribution were observed at the two axial locations investigated. Overall a slight decrease in iron content was identified from edge to center at just above mid-height (Figure 35). An opposite effect was established just below mid-height (Figure 36); however, a significant amount of scatter was observed at this axial position. Less scatter in the data was observed at just above mid-height.

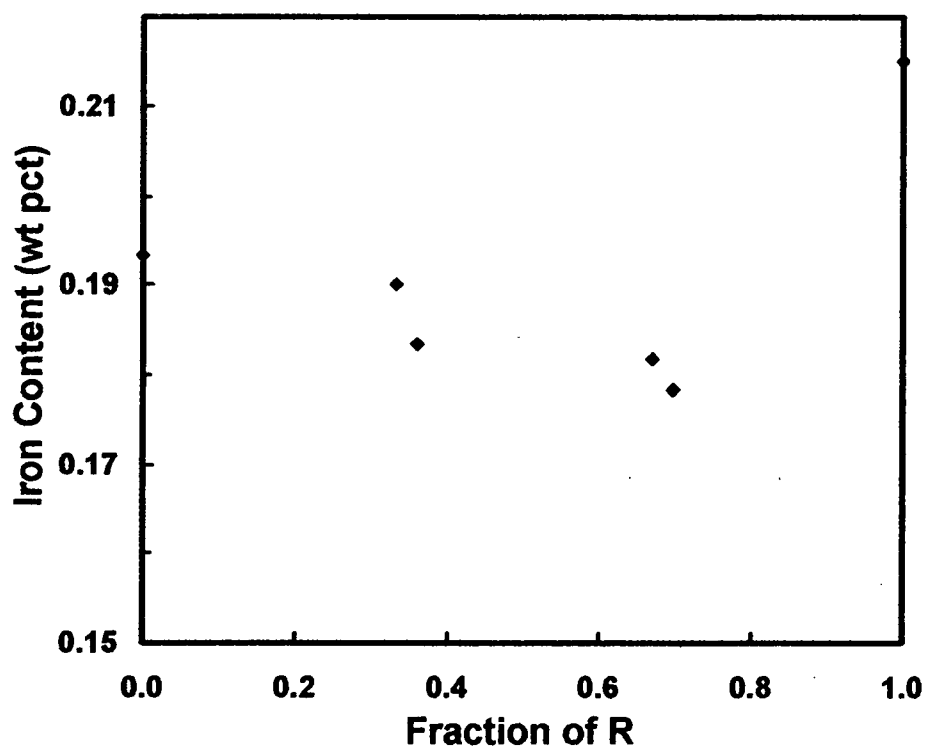


Figure 35. Iron radial distribution, just above mid-height, in a Ti-6Al-4V small-scale ingot.

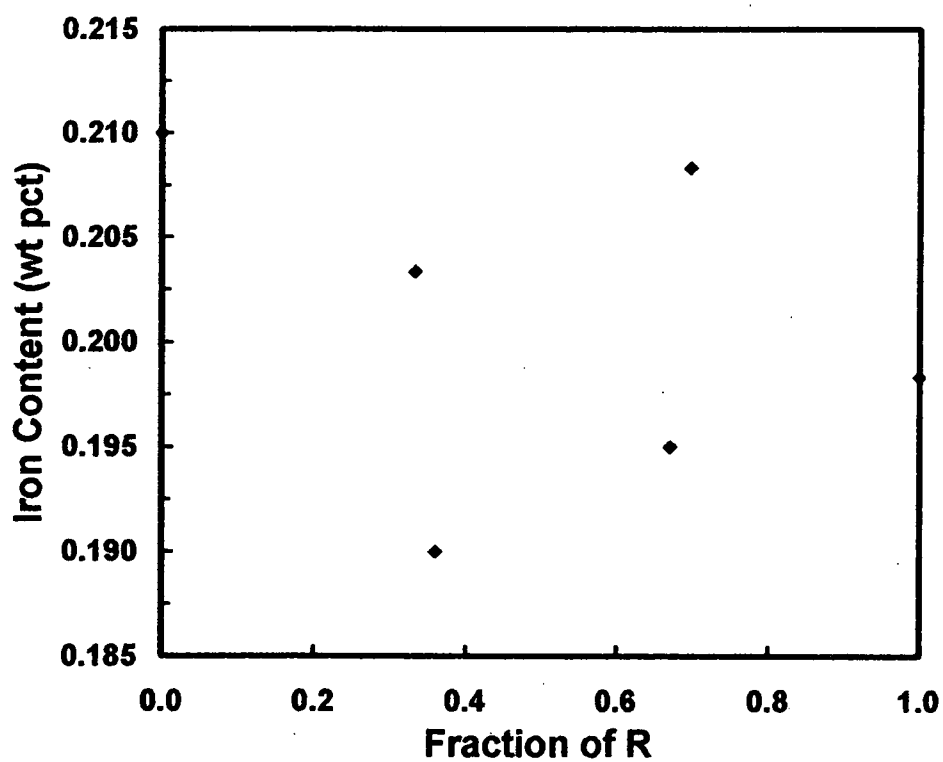


Figure 36. Iron radial distribution, just below mid-height, in a Ti-6Al-4V small-scale ingot.

5.4 Conclusions

Solute distribution across the radius of a Ti-6Al-4V production-scale ingot varied from slab to slab and within individual slabs for all solutes considered. Solute distribution also varied at the two axial locations in the small-scale ingot for all solutes considered. As observed in the production-scale ingot, there are possibly different trends in the columnar than the equiaxed zone. Additionally, a relationship between iron and oxygen distribution was not established for the production-scale ingot.

CHAPTER VI

SEGREGATION MODELING

The results of segregation modeling are presented in this chapter. Modeling was completed using two simple microsegregation models and one macrosegregation model. The Lever Rule and the Scheil Equation microsegregation models were used, and the local solute redistribution macrosegregation model was used. A sensitivity analysis was conducted, and the segregation of four solutes of Ti-6Al-4V was determined. Solute of interest included: aluminum, vanadium, iron, and oxygen.

6.1 Procedures

6.1.1 Equations and Assumptions

Both micro- and macrosegregation models were employed: including the lever rule, Scheil model, and several limiting cases of the local solute redistribution equation. The assumptions of each model are discussed briefly. The goal of the modeling was to determine the usefulness of straightforward analytical relationships in macrosegregation prediction.

6.1.1.1 Microsegregation Models

Both the lever rule and Scheil model are perhaps best suited for unidirectional heat and fluid flow, similar to conditions found in directional solidification. The Lever Rule assumes k to be constant for a given temperature range, to simplify mathematics. The

assumptions include equilibrium solidification, complete diffusion in the solid and liquid phases, and no significant degree of undercooling. The assumptions of the Scheil Equation are similar to that of the Lever Rule except that no solid diffusion is assumed.

6.1.1.2 Macrosegregation Models

The local solute redistribution equation (LSRE) assumes no solid phase deformation and no flow in the bulk liquid phase. Flow in the mushy zone, however, is considered [2]. The media must be porous for Darcy's law to be valid.

Five limiting cases of the LSRE were considered. The basis for each case was unidirectional solidification with heat and fluid flow only in the x-direction. Partition coefficients, solid and liquid density, viscosity, and pressure drop were assumed constant for all cases considered.

For the first case, "steady state" solidification, the LSRE reduces to an equation identical to the Scheil equation [47]

$$f_L = \left(\frac{C_L}{C_o} \right)^{\frac{-1}{(1-k)}} \quad (12)$$

The second case considers solidification against a cold mold wall with finite resistance to heat transfer at the interface [47].

$$f_L = \left(\frac{C_L}{C_o} \right)^{\frac{-(1-\beta)}{(1-k)}} \quad (13)$$

The third case considers solidification in a cold mold with no resistance to heat transfer at the interface [47]. These conditions apply to an alloy with a narrow freezing range. Results, however, match those of the first limiting case. The fourth case considers the same as the third except; the freezing range is very wide [47].

$$f_L = \left(\frac{C_L}{C_o} \right)^{\frac{[1-(\beta/2)]}{(1-k)}} \quad (14)$$

The last case assumes fluid flow is parallel to primary dendrites and the permeability is variable.

$$C_s = kC_o \left(\frac{m(1-f_s)^2 + (1-f_s) - 1}{m(1-f_s)} \right)^{\frac{m}{2q}} \left(\frac{f_s(-1 + \sqrt{1+4m}) + 2m(1-f_s)}{f_s(-1 - \sqrt{1+4m}) + 2m(1-f_s)} \right)^{\frac{m}{2q\sqrt{1+4m}}} \quad (15)$$

$$m = \frac{C_2 d_1^2 \Delta T_x \left(\frac{\Delta P}{\Delta x} + \rho_L g_r \right)}{\varepsilon \mu \Delta x} \quad (16)$$

$$q = - \left(\frac{1-\beta}{1-k} \right) \quad (17)$$

Darcy's law was utilized in the development of the previous equations. The permeability was assumed constant for a given fraction liquid and was calculated via

$$K = C_2 \frac{d_1^2 f_L^3}{(1-f_L)} \quad (18)$$

$$C_2 = 4.53 \times 10^{-4} + 4.02 \times 10^{-6} (f_L + 0.1)^{-5} \quad (19)$$

The average deviation for the previous equations is ± 92 pct [48].

C_s was calculated via C_L and k for various solutes as a function of fraction solidified to assess the tendency for segregation.

6.1.2 Thermophysical Data

Several parameters had to be obtained or estimated in order to predict the tendency for segregation. All necessary parameters could not be acquired directly from the literature. Liquid and solid phase densities, and liquid viscosity, however, were taken directly from the literature. Binary partition coefficients, temperature gradients, and cooling rates within the melt had to be estimated using graphical data from the literature. Non-binary partition coefficients, mushy zone length, and primary dendrite arm spacing were obtained from unpublished research. Pressure drop across the mushy zone was estimated based on superalloy modeling.

6.1.2.1 Partition Coefficients

The partition coefficients were obtained from the literature and thermodynamic calculations [44]. Again, the initial composition was taken from alloy XB3043. Binary partition coefficients were estimated from [49], [50], [51], and [52] for binary titanium phase diagrams containing aluminum, vanadium, iron, and oxygen, respectively.

The other set of partition coefficients was determined for XB3043 alloy system using the PandatTM software [36] with input data taken from the PanTitanium thermodynamic database [44].

Table 6. Partition coefficients taken from the literature (binary) and calculated for alloy XB3043.

Solute	k_{lit}	$k_{Pan}^{[44]}$
Al	0.626	1.165
V	0.400	1.133
Fe	0.375	0.259
O	5.610	1.974

6.1.2.2 Solidification Shrinkage

Solidification shrinkage was calculated from the densities of the solid and liquid phases. These values for Ti-6Al-4V were taken from the literature [53]. The densities were measured using the levitated drop method, discussed elsewhere [54].

6.1.2.3 Additional Parameters

Additional parameters included permeability of the medium, liquid viscosity, change in pressure across the mushy zone, liquid density, volume fraction liquid, dendrite arm spacing, gravitational acceleration, temperature gradients, and cooling rates within the melt. Liquid-phase viscosity and density were taken from the literature [53]. Volume fraction liquid was varied from 1.0 (start of solidification) to 0.0 (end of solidification).

For the sensitivity analysis, primary dendrite arm spacing was varied from 7.78×10^{-4} m to 1.00×10^{-3} m after superalloy measurements [55]. Pressure drop across the mushy zone was varied from 0.1 [56] to 1.0 atm. Extreme cases of 0.01 and 10 atm were also investigated. The length of the mushy zone was varied from 0.01 to 0.14 m after superalloy modeling [57]. Temperature gradients and cooling rates within the melt were estimated from published literature values [58].

For segregation modeling of ingot slab "C," pressure drop across the mushy zone, mushy zone length, temperature gradients, and cooling rates within the melt were maintained at the minimum values. Partition coefficients were estimated from the literature.

6.1.3 Sensitivity Analysis

A sensitivity analysis was conducted to determine the impact parameters had on the tendency for macrosegregation. The LSRE, with the assumption of unidirectional heat and fluid flow, was the main focus. Limiting cases one through four were investigated as well and all produced similar results. See Appendix J for additional segregation plots. Solidification shrinkage, partition coefficients, pressure drop, and liquid viscosity were assumed constant. Parameters of interest included partition coefficients, primary dendrite arm spacing, pressure drop across the mushy zone, mushy zone length, temperature gradients, and cooling rates. One parameter was varied, as others were held constant.

The starting composition was taken from wet chemical analysis of alloy XB0343, considered close to standard industry composition for Ti-6Al-4V. Solutes of interest included aluminum, vanadium, iron, and oxygen. The segregation of the other alloying elements was not considered for this analysis.

Temperature gradients and cooling rates corresponded to solidification conditions for a mixed (columnar/equiaxed) grain structure [58]; similar to the structure found in as-cast production-scale ingots.

Table 7. Input parameters for the sensitivity analysis using the LSRE.

Parameter	Minimum Value	Maximum Value
C_{0Al}	5.96	na
C_{0V}	4.12	na
C_{0Fe}	0.10	na
C_{0O}	0.20	na
ρ_s (kg/m ³)	4165.13	na
ρ_L (kg/m ³)	3899.6	na
μ (N s/m ²)	0.00325	na
ΔP (atm)	0.1	1
g_L	0.00	1.00
d_1 (m)	0.000778	0.001
g_r (m/s ²)	9.8	na
G (K/m)	225	250
ε (K/s)	30	35
Δx (m)	0.01	0.14

6.1.4 Segregation Calculations for Ingots

Initial alloy compositions were taken from wet chemical analysis of the middle plate of the Ti-6Al-4V VAR ingot used for the production-scale analysis. The middle ingot slab is the similar to conditions in which there is unidirectional heat and fluid flow. Similar to the sensitivity analysis, solutes of interest included aluminum, vanadium, iron, and oxygen. The segregation of the other alloying elements was not considered for this analysis. Although the LSRE, limiting case five, was the main interest, the lever rule (equation 3) and Scheil model (equation 7) were used for comparison. See Appendix I for a complete set of input parameters.

$$C_s f_s + C_L f_L = C_o \quad (3)$$

$$C_s^* = k C_o (1 - f_s)^{(k-1)} \quad (7)$$

6.2 Results of Sensitivity Analysis

6.2.1 Partition Coefficients

The tendency for macrosegregation was different from solute to solute. The LSRE became unstable at approximately $f_s = 0.55-0.60$. The curves quickly approach infinity for solutes Al, V, and Fe (Figures 37-40). Predicted segregation curves for oxygen quickly approach zero in this range (Figure 40). Aluminum and vanadium contents were higher for thermodynamically calculated k-values than for those estimated from the literature. The opposite was observed for solutes iron and oxygen.

Similar behavior was observed for both sets of partition coefficients for this limiting case of the LSRE, however, the thermodynamically-calculated partition coefficients shifted the y-axis intercept for solutes Al, V, and Fe. The opposite effect was observed for oxygen. Aluminum, vanadium, and iron exhibited a tendency for positive segregation over the course of solidification while oxygen exhibited a tendency for negative segregation. These observations indicate that accurate knowledge of the partition coefficients is very important for this limiting case of the LSRE.

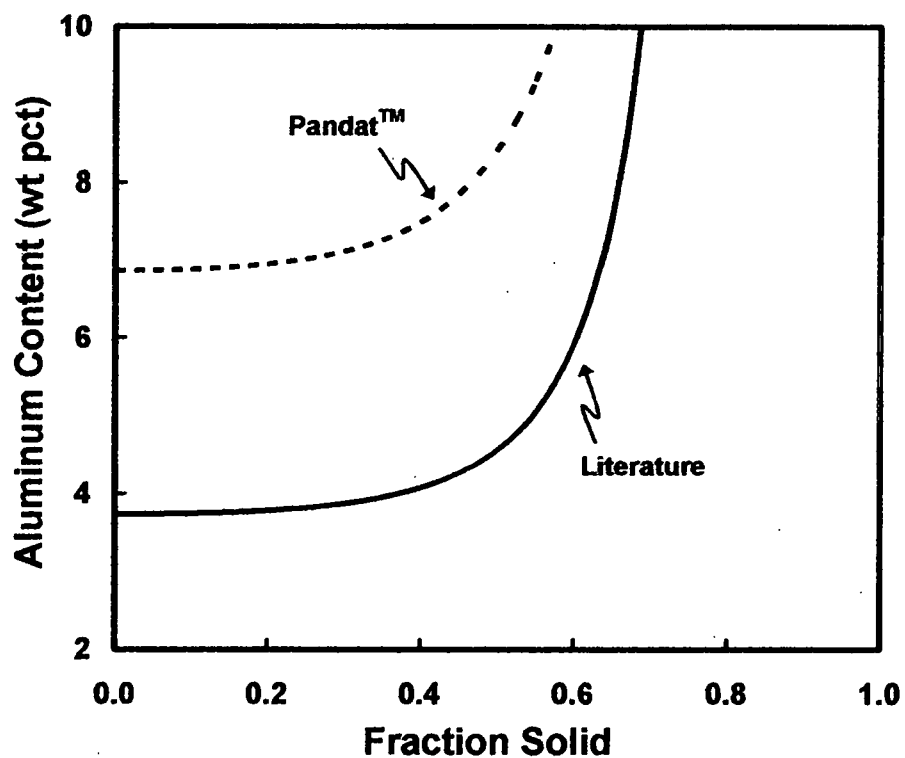


Figure 37. Predicted aluminum segregation, from the LSRE, using partition coefficients from the literature [49] and thermodynamic calculations [44].

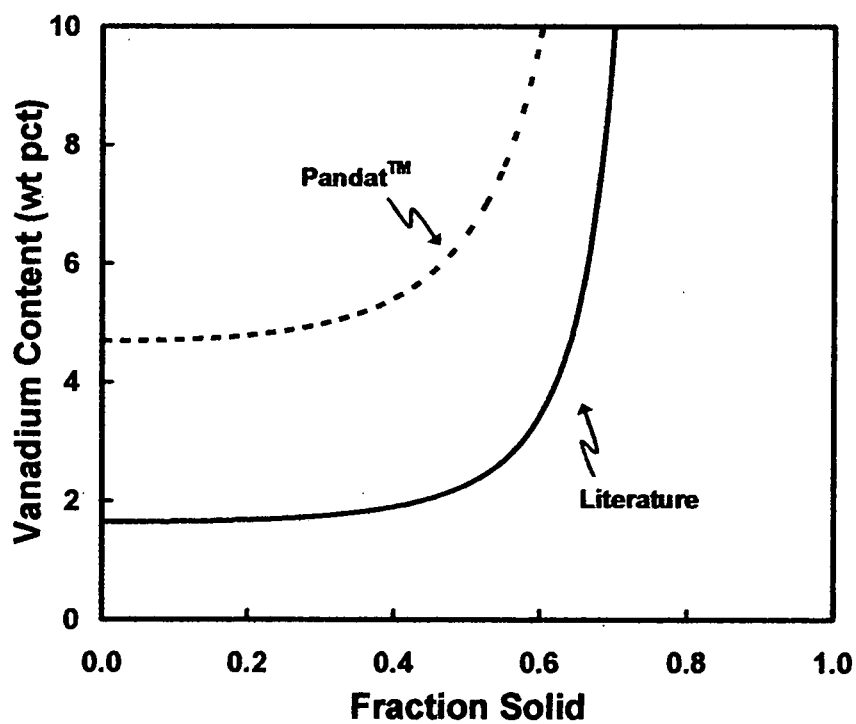


Figure 38. Predicted vanadium segregation, from the LSRE, using partition coefficients from the literature [50] and thermodynamic calculations [44].

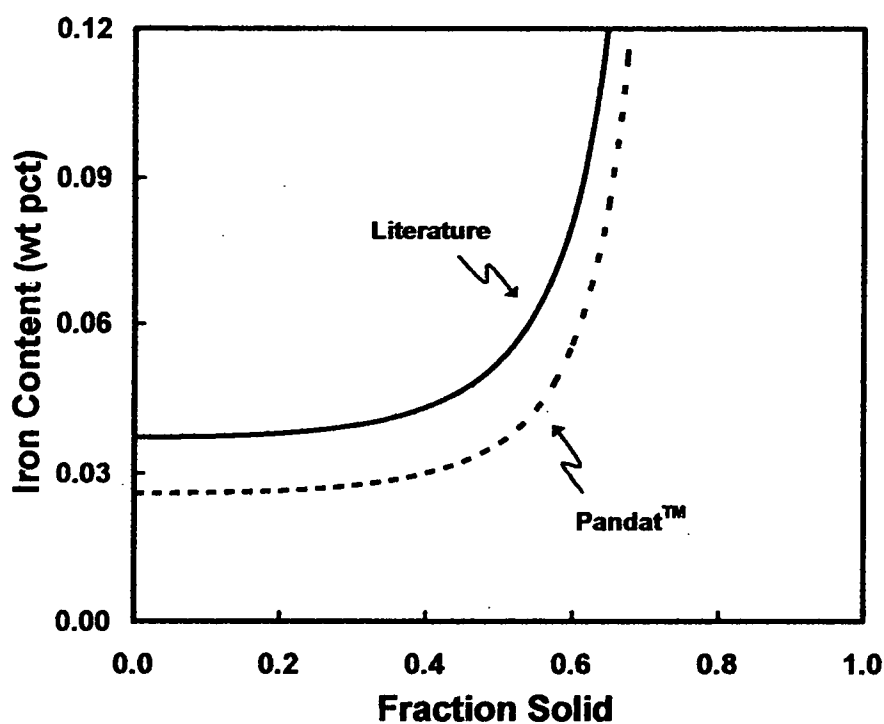


Figure 39. Predicted iron segregation, from the LSRE, using partition coefficients from the literature [51] and thermodynamic calculations [44].

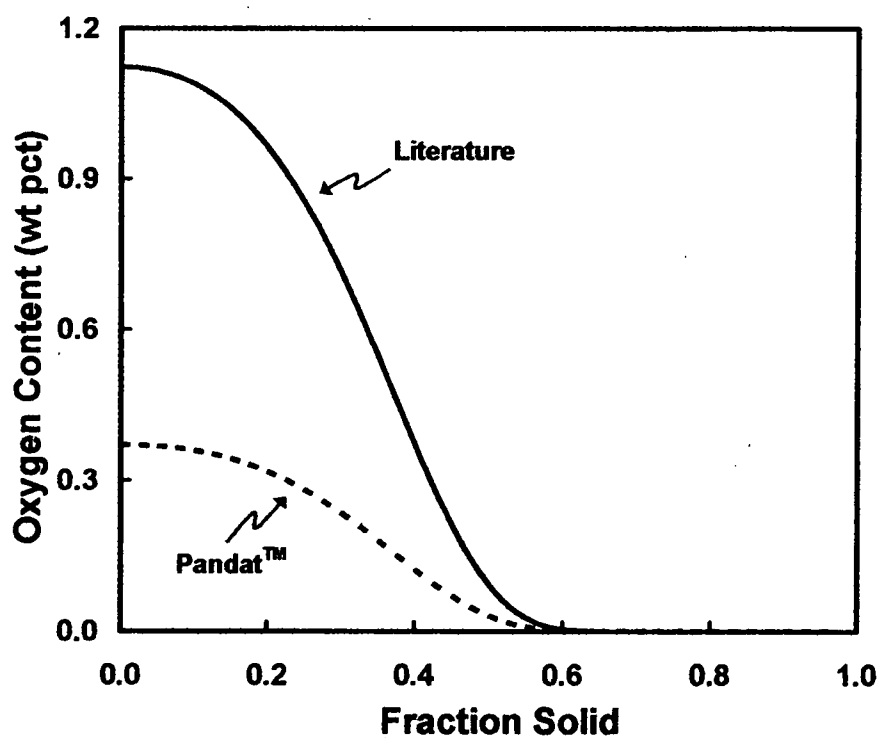


Figure 40. Predicted oxygen segregation, from the LSRE, using partition coefficients from the literature [52] and thermodynamic calculations [44].

6.2.2 Primary Dendrite Arm Spacing

Increasing the primary dendrite arm spacing did not have a significant impact on the tendency for segregation for any solute (Figures 41-44). The equation became unstable at $f_s=0.55-0.60$, approaching infinity for aluminum, vanadium, and iron, and zero for oxygen. Again, aluminum, vanadium, and iron exhibited a tendency toward positive segregation, while oxygen tended toward negative segregation. For this model, accurate knowledge of primary dendrite arm spacing is of less importance.

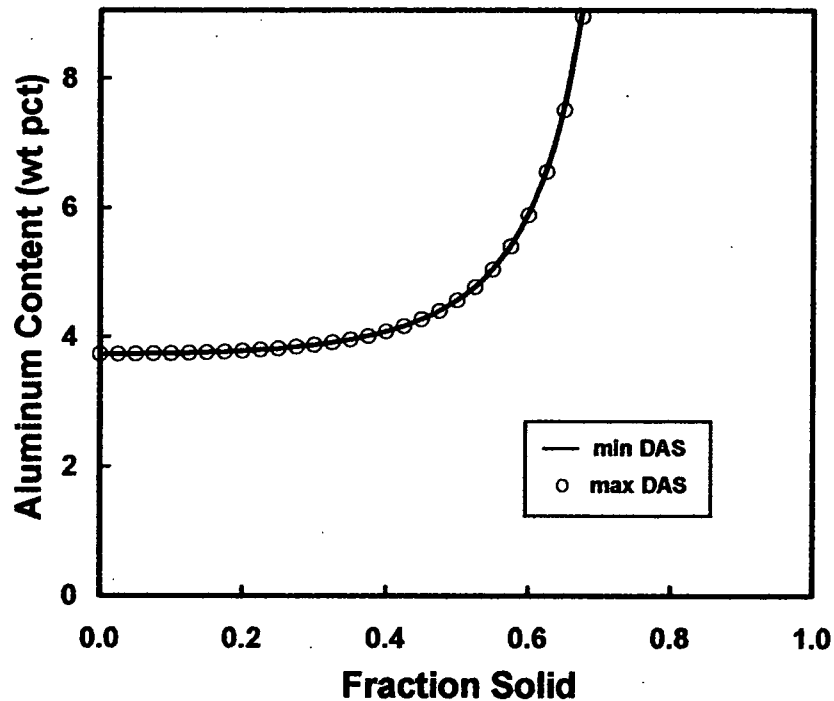


Figure 41. Predicted aluminum segregation, from the LSRE, using minimum and maximum values of primary dendrite arm spacing.

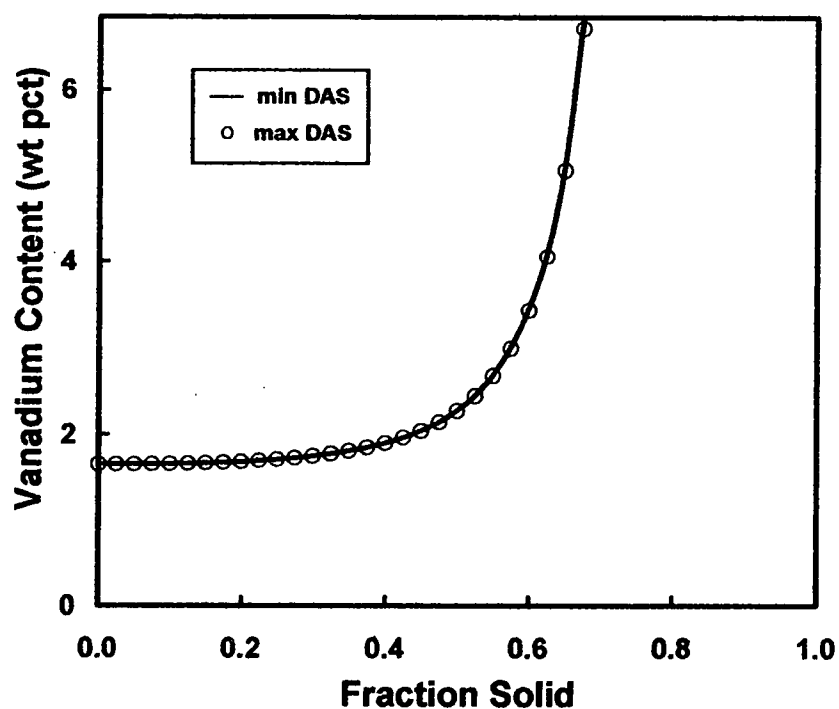


Figure 42. Predicted vanadium segregation, from the LSRE, using minimum and maximum values of primary dendrite arm spacing.

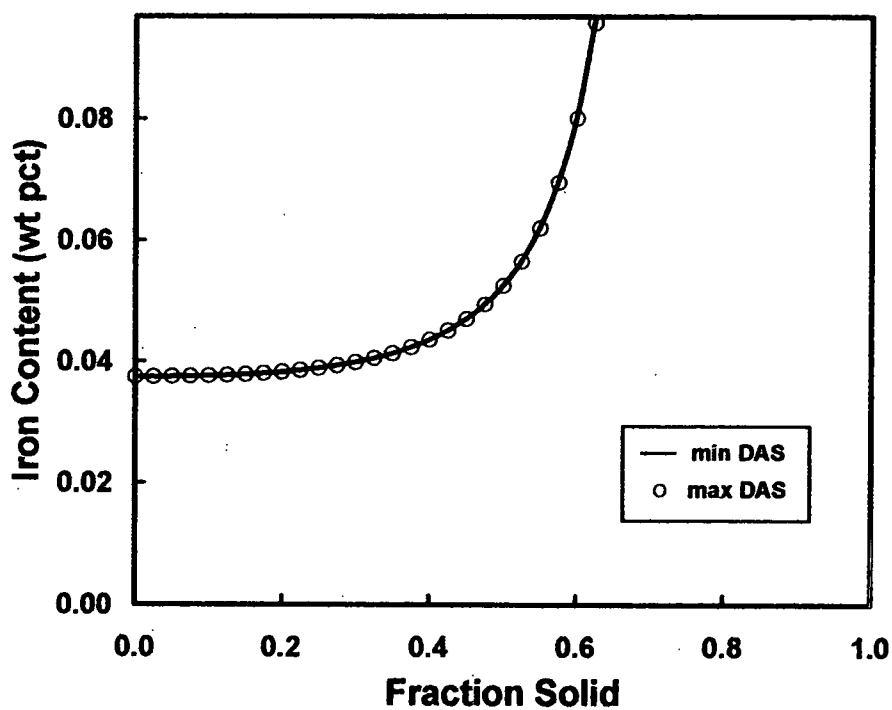


Figure 43. Predicted iron segregation, from the LSRE, using minimum and maximum values of primary dendrite arm spacing.

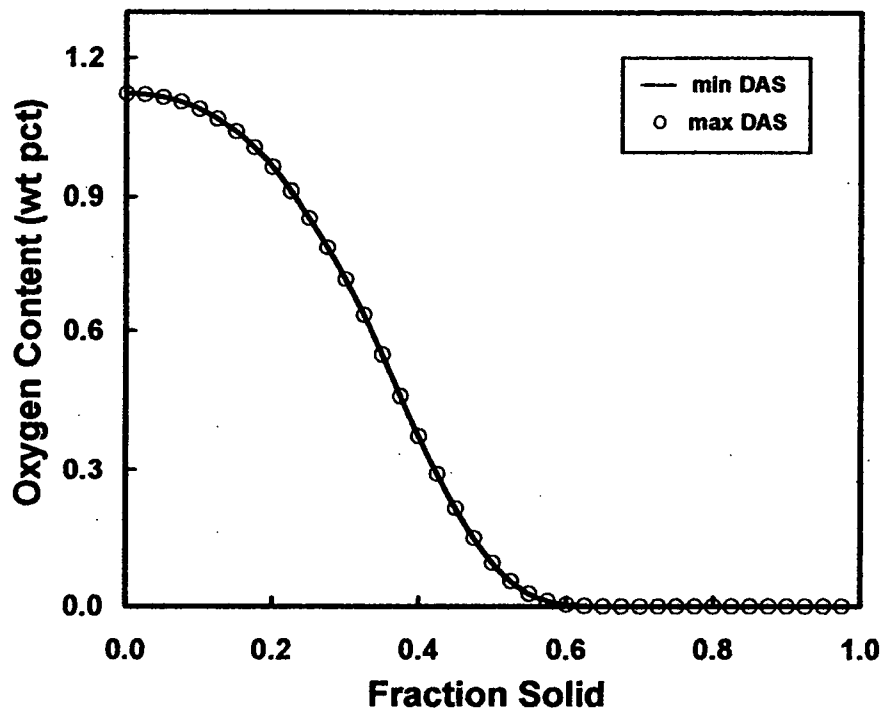


Figure 44. Predicted oxygen segregation, from the LSRE, using minimum and maximum values of primary dendrite arm spacing.

6.2.3 Pressure Drop across the Mushy Zone

Increasing pressure drop did not have a significant impact on the tendency for macrosegregation (Figures 45–48). Reducing pressure drop to 0.01 atm did not have a significant impact either (Figure 49). Additionally, the LSRE becomes unstable at approximately 0.55–0.60 fractions solid for all solutes considered. For this limiting case of the LSRE, pressure drop across the mushy zone is a less important parameter.

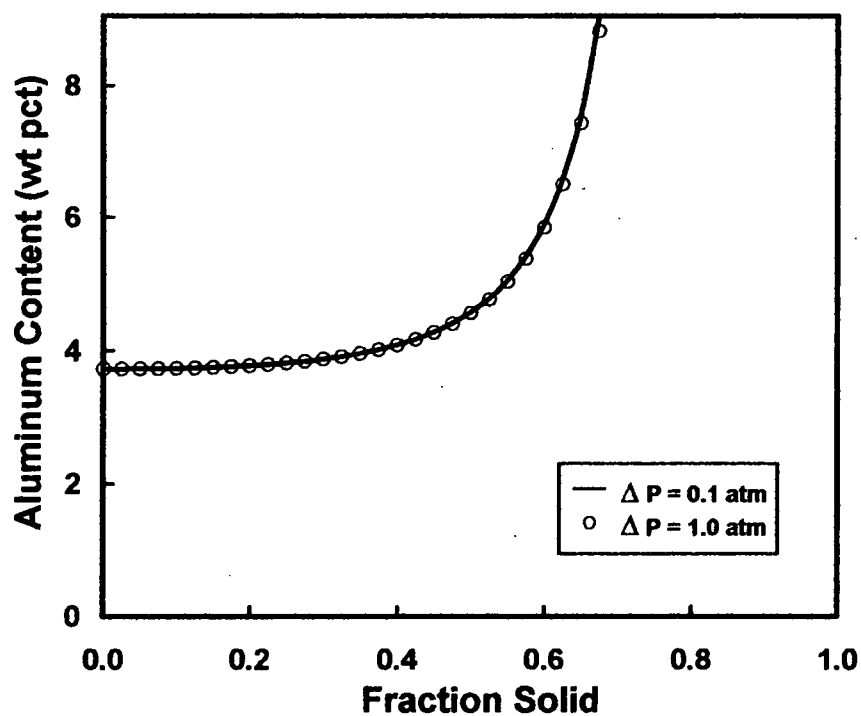


Figure 45. Predicted aluminum segregation, from the LSRE, using varied mushy zone pressure drops.

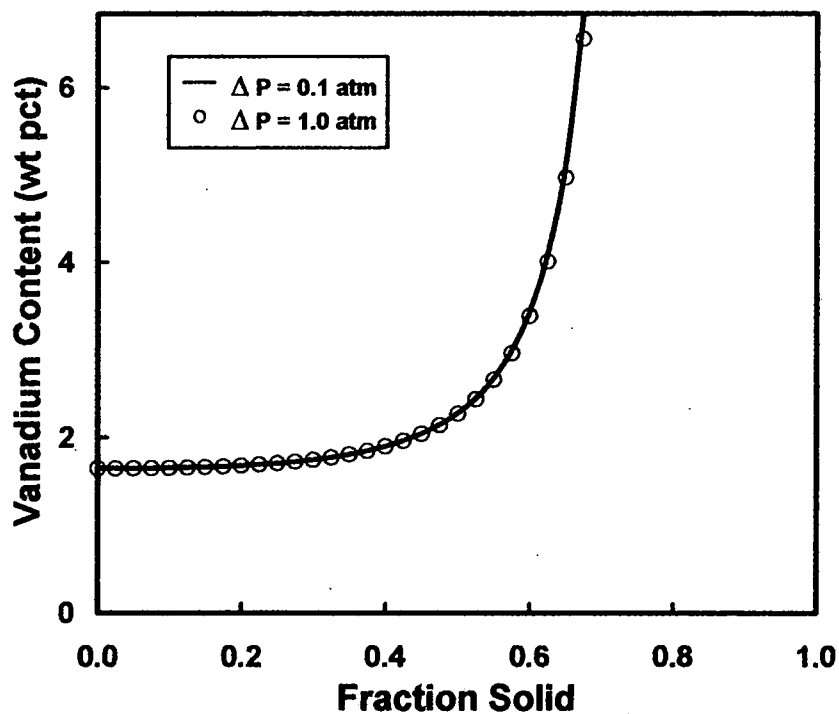


Figure 46. Predicted vanadium segregation, from the LSRE, using varied mushy zone pressure drops.

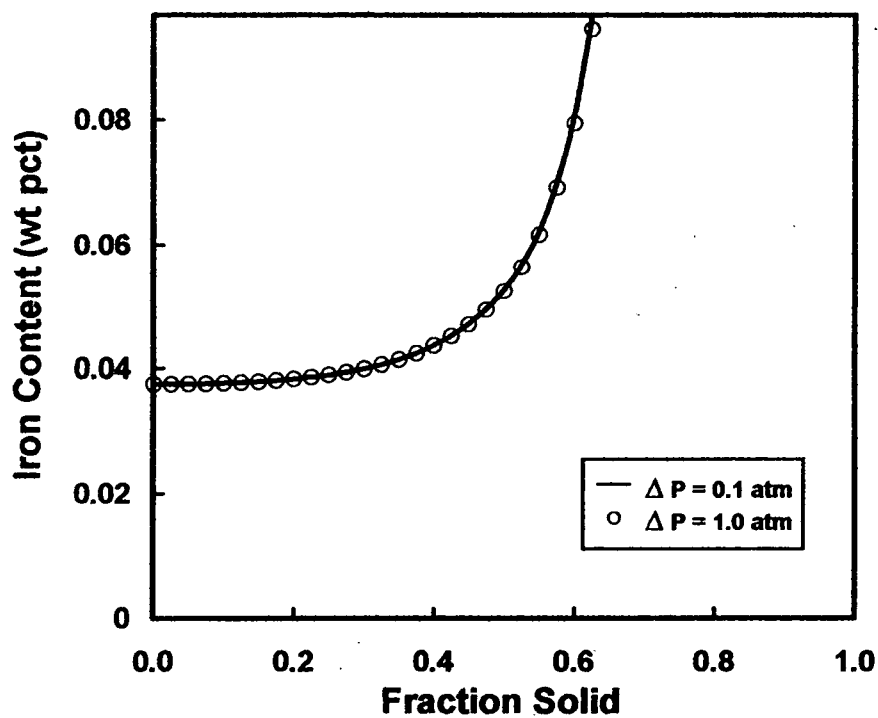


Figure 47. Predicted iron segregation, from the LSRE, using varied mushy zone pressure drops.

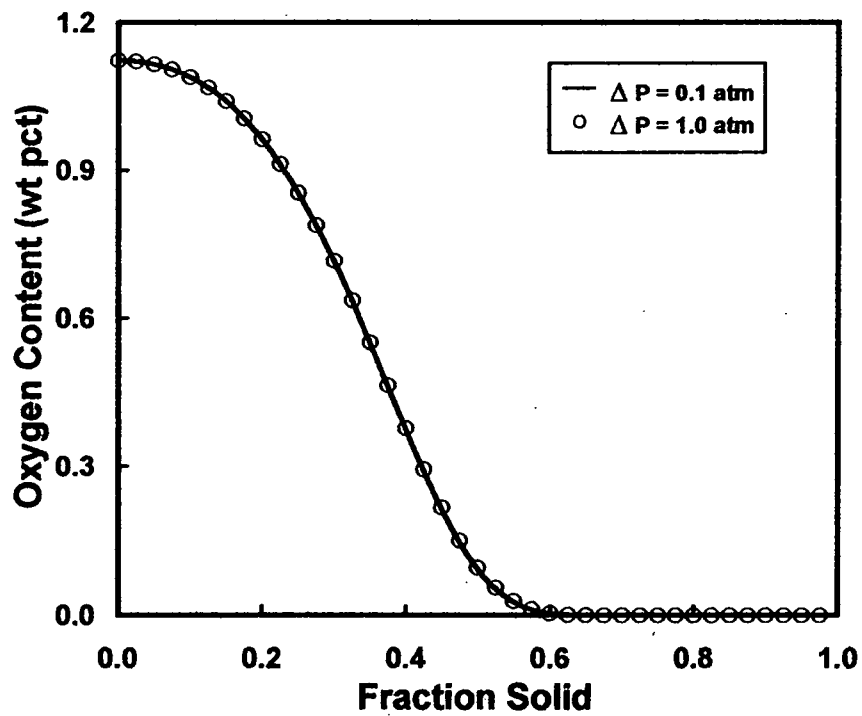


Figure 48. Predicted oxygen segregation, from the LSRE, using varied mushy zone pressure drops.

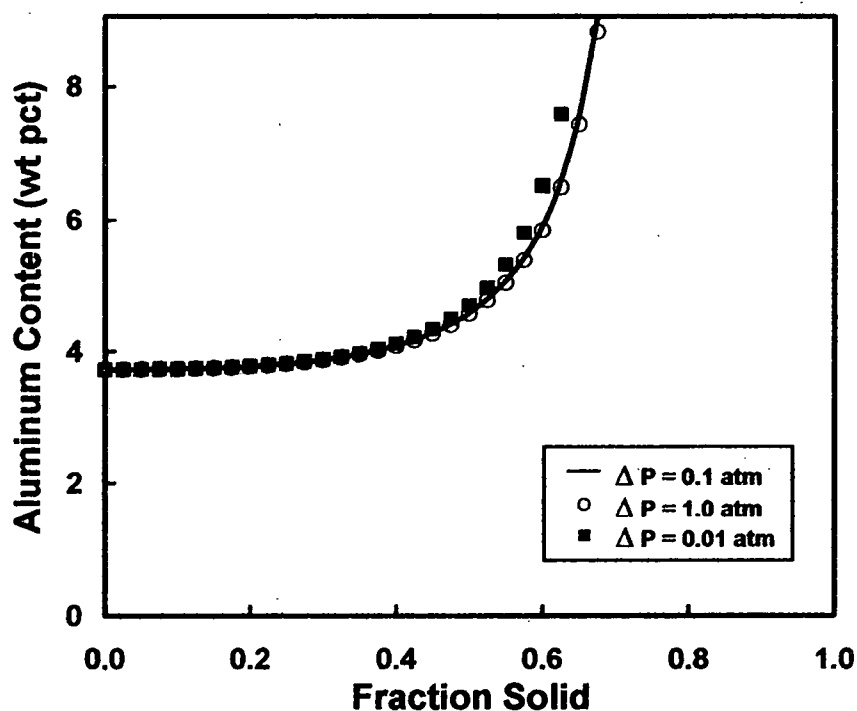


Figure 49. Predicted aluminum segregation, from the LSRE, using varied mushy zone pressure drops.

6.2.4 Mushy Zone Length

Increasing the mushy zone length had a significant impact on the usefulness of the LSRE. At the maximum length (0.14m), the equation became unstable after twenty-five percent fraction solidified for all four solutes (Figures 50-53). At the minimum mushy zone length, the LSRE became unstable in the fraction-solidified range 0.55-0.60. Accurate knowledge of the mushy zone is very important for use with this limiting case of the LSRE.

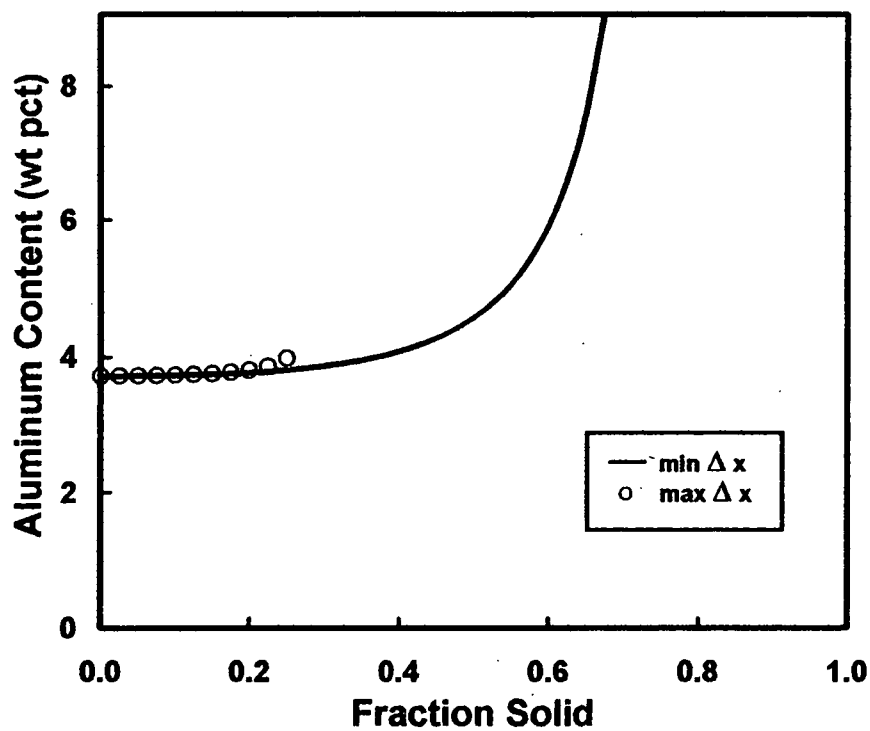


Figure 50. Predicted aluminum segregation, from the LSRE, using varied mushy zone lengths.

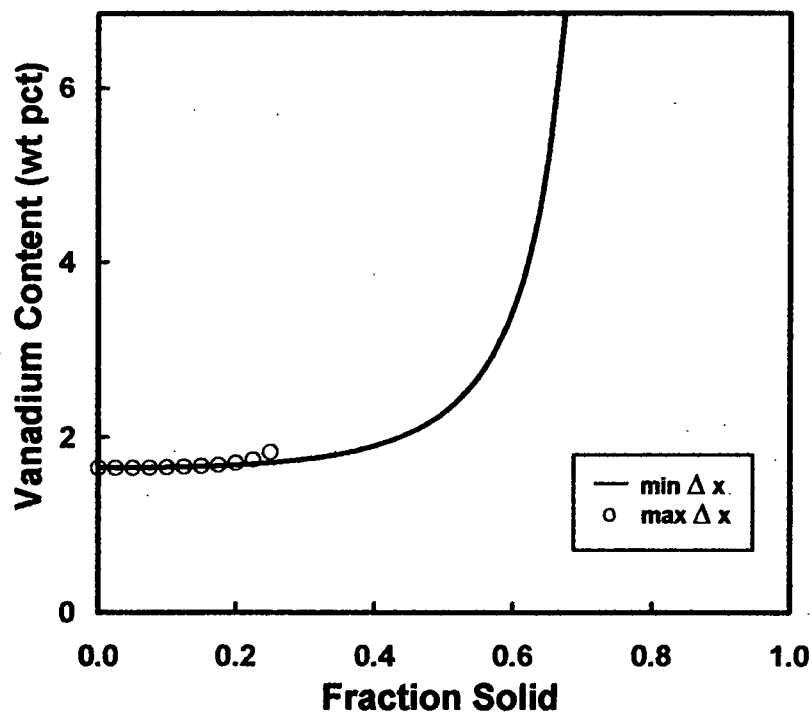


Figure 51. Predicted vanadium segregation, from the LSRE, using varied mushy zone lengths.

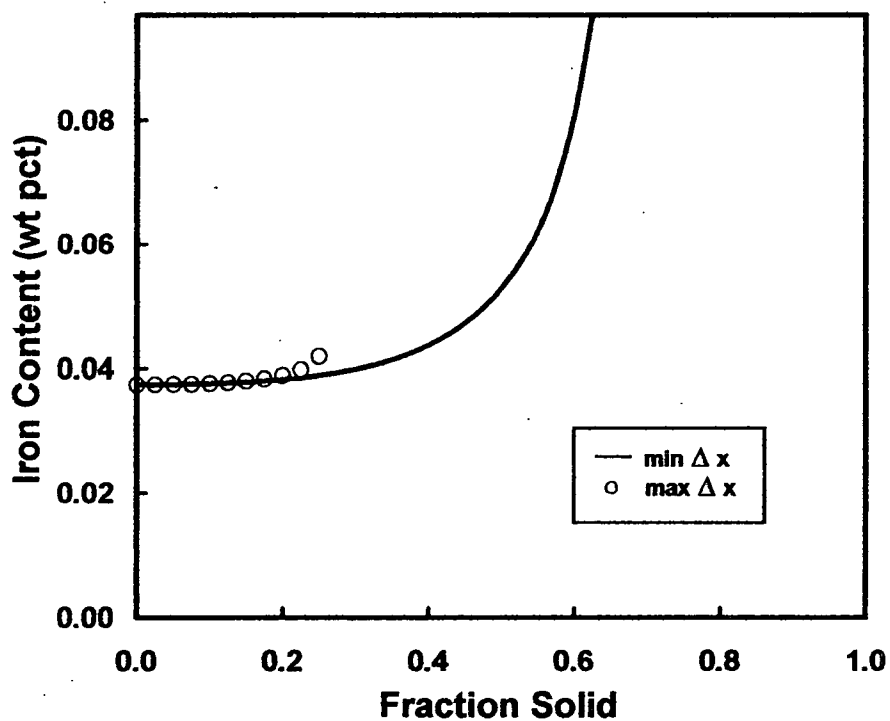


Figure 52. Predicted iron segregation, from the LSRE, using varied mushy zone lengths.

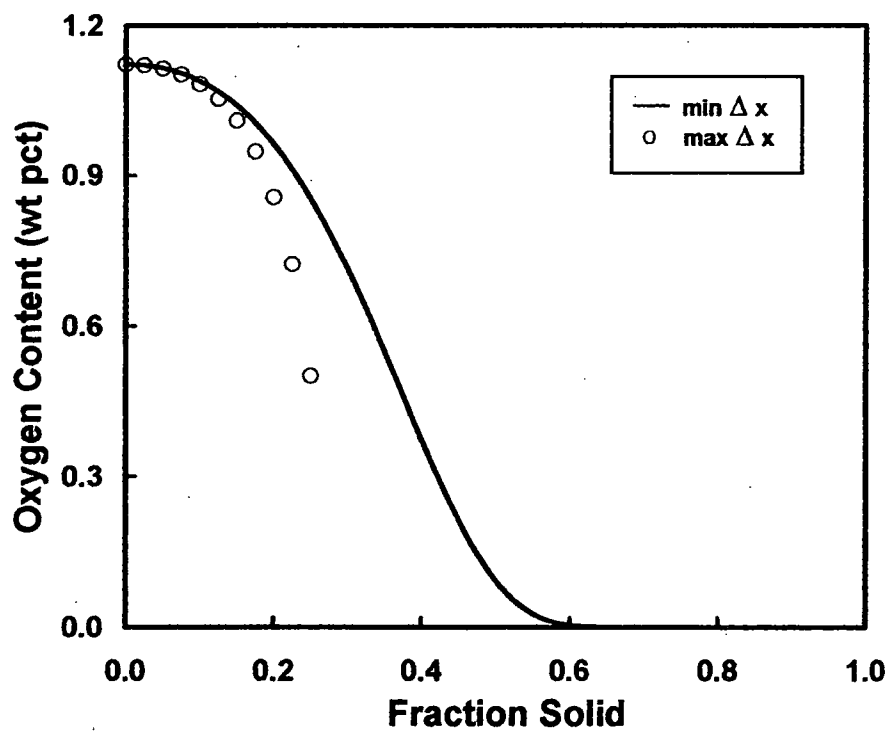


Figure 53. Predicted oxygen segregation, from the LSRE, using varied mushy zone lengths.

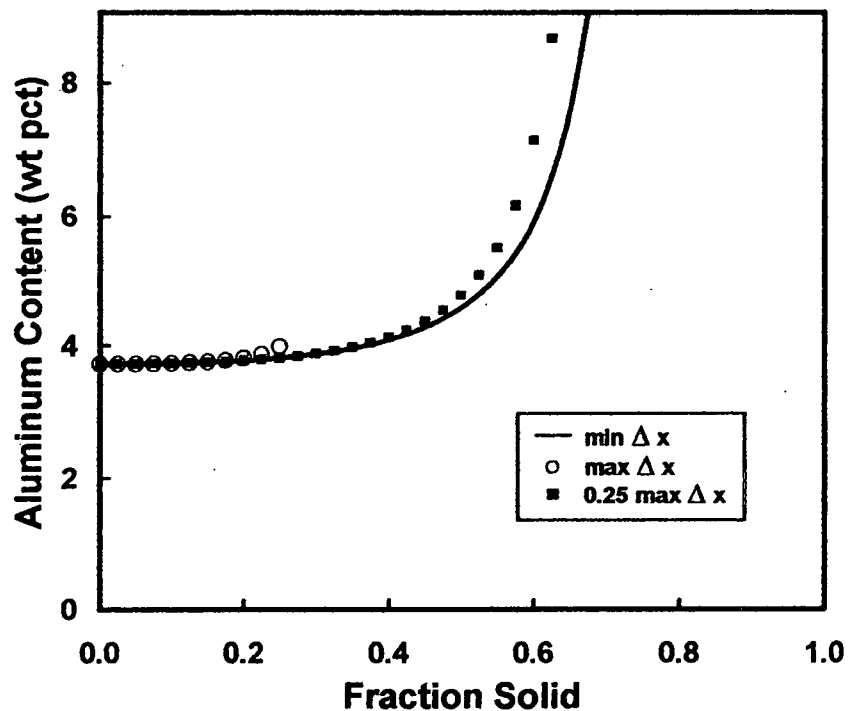


Figure 54. Predicted aluminum segregation, from the LSRE, using varied mushy zone lengths.

6.2.5 Temperature Gradients and Cooling Rates

Increasing the temperature gradient and cooling rates did not significantly impact the tendency for segregation for any solute considered (Figures 55-58). Changing the solidification conditions did not significantly impact the results either. I.e. Tendency for segregation in a fully-equiaxed structure was similar to that of a mixed structure. Also, the equation became unstable at approximately 0.55-0.60 fraction solidified. Refer to Appendix J for additional plots. Accurate knowledge of temperature gradients and cooling rates is of less importance than other parameters used for this model.

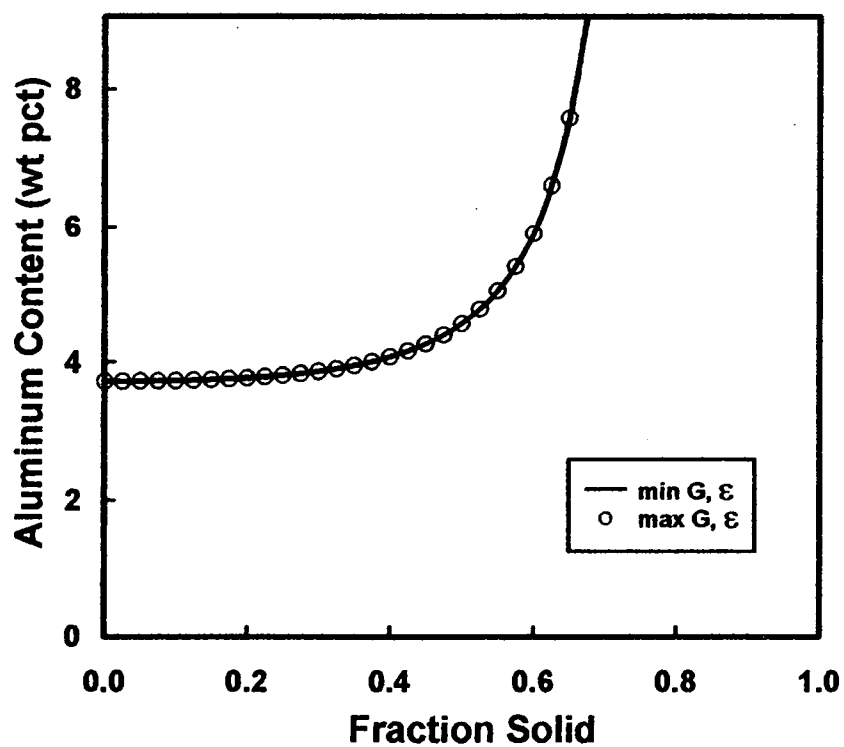


Figure 55. Predicted aluminum segregation, from the LSRE, using varied temperature gradients (G) and cooling rates (ϵ).

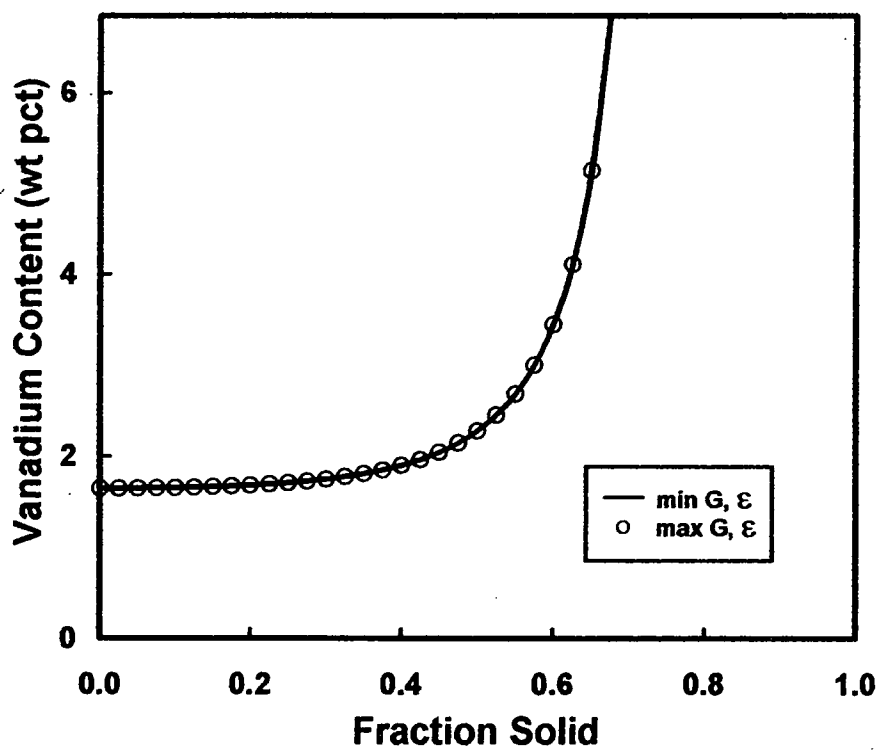


Figure 56. Predicted vanadium segregation, from the LSRE, using varied temperature gradients (G) and cooling rates (ϵ).

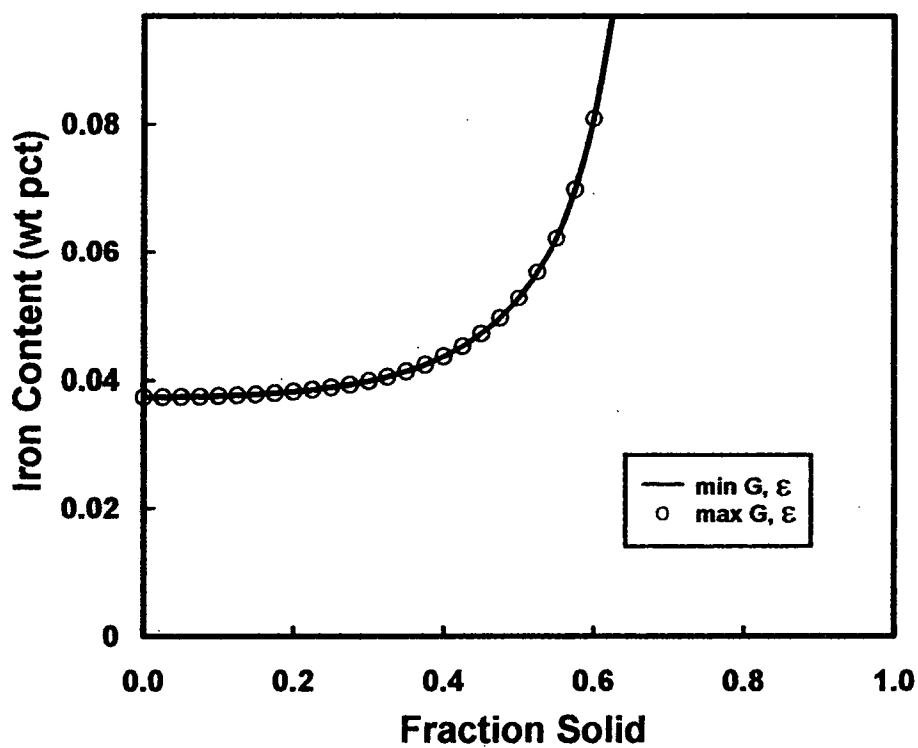


Figure 57. Predicted iron segregation, from the LSRE, using varied temperature gradients (G) and cooling rates (ϵ).

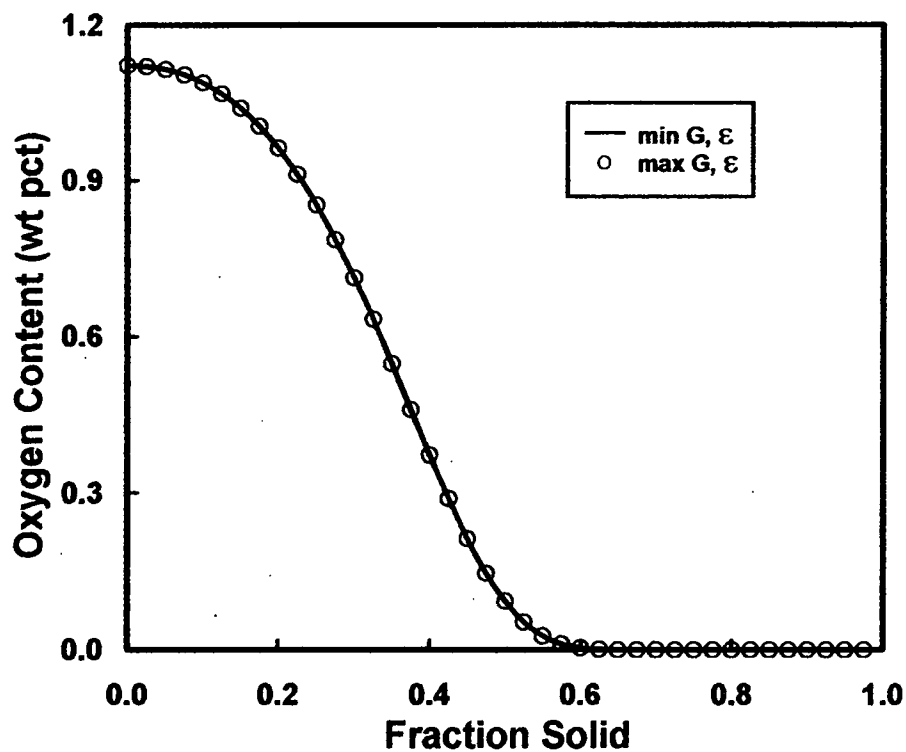


Figure 58. Predicted oxygen segregation, from the LSRE, using varied temperature gradients (G) and cooling rates (ϵ).

6.3 Results of Segregation Calculations for Ingots

Tendency for segregation was different for the lever rule and Scheil equation than for the LSRE. Similar to the sensitivity analysis, the LSRE became unstable at approximately 0.55-0.60 fraction solidified (Figures 60, 62, 64, 66). The Scheil equation became unstable as well at different fraction solidified ranges depending on the solute. Additionally, aluminum and vanadium contents, predicted with use of the LSRE, were higher with the use of the thermodynamically calculated k -values than with those estimated from the literature (Figures 60 and 62). The opposite effect was observed for solutes iron and oxygen (Figures 64 and 66). A tendency towards positive segregation was observed for solutes aluminum, vanadium, and iron. The opposite effect was observed for oxygen.

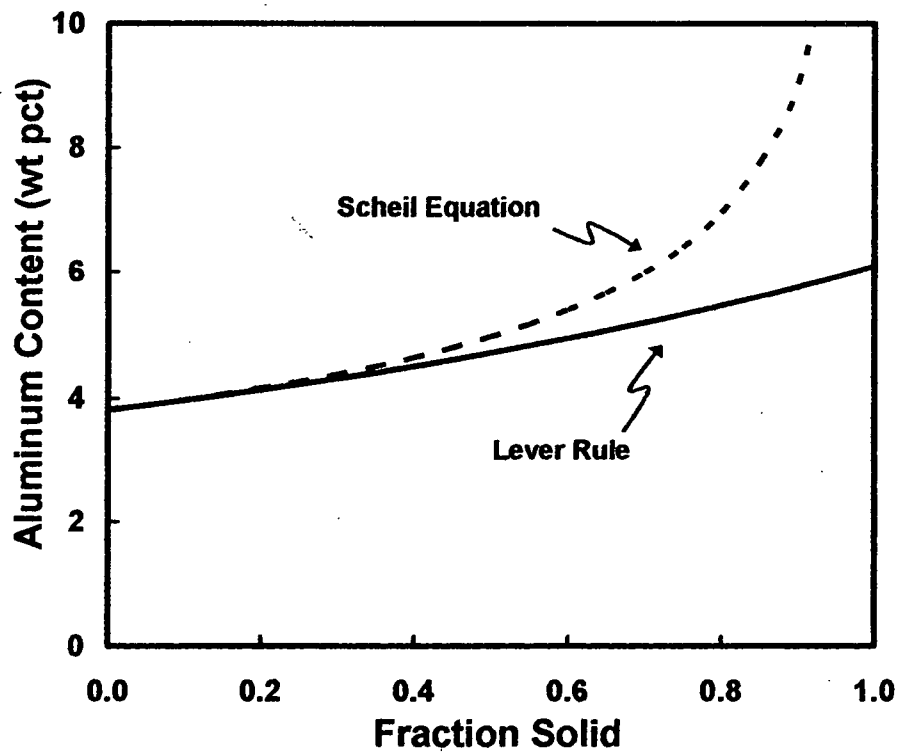


Figure 59. Predicted aluminum segregation for slab "C" using Lever rule and Scheil equation.

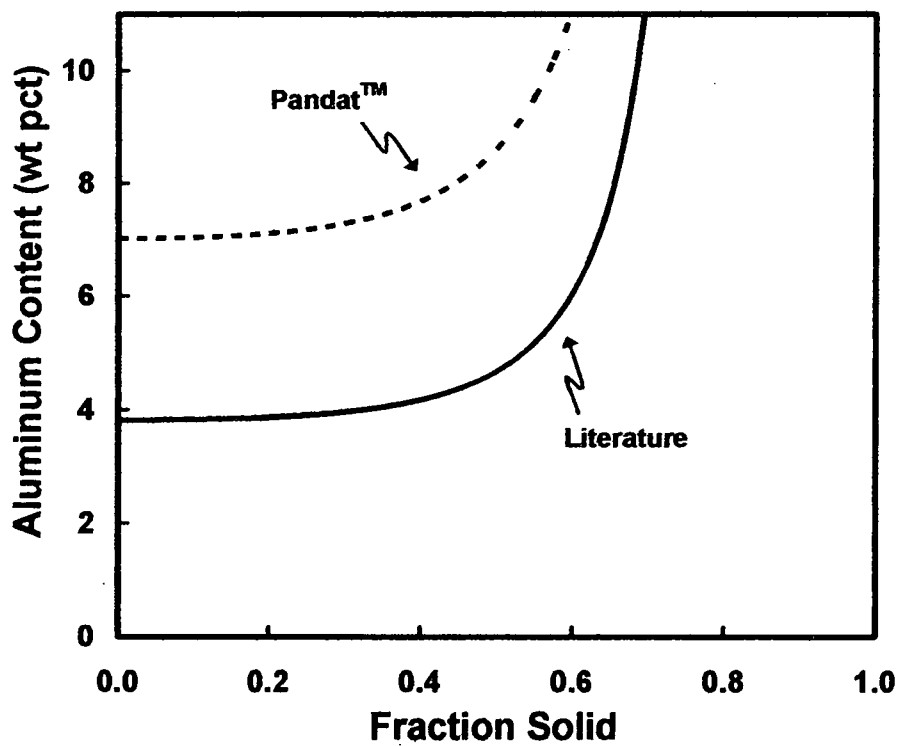


Figure 60. Predicted aluminum segregation for slab "C" using the LSRE.

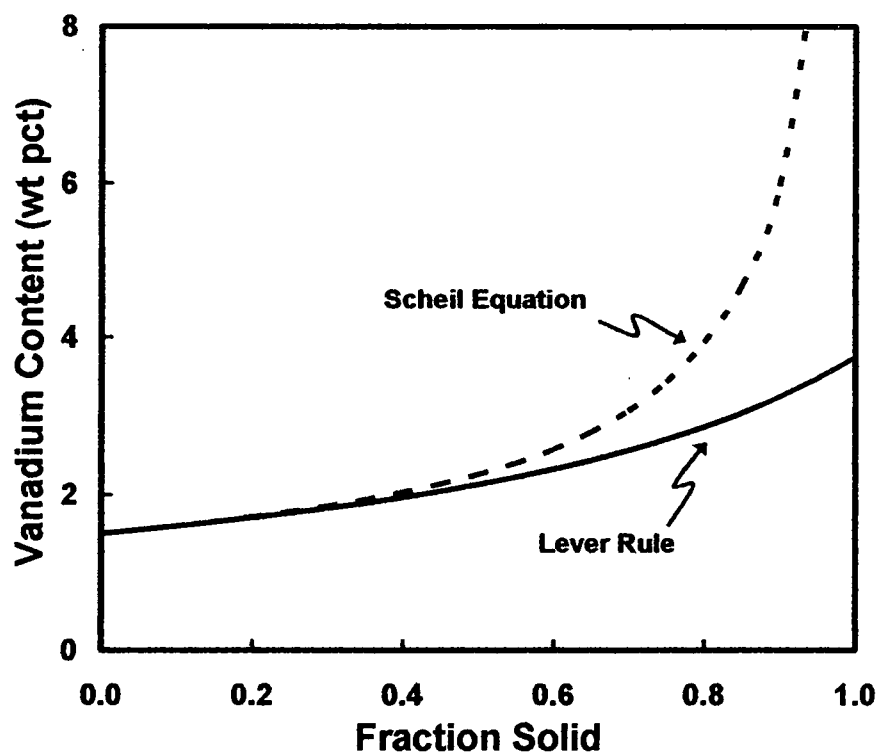


Figure 61. Predicted vanadium segregation for slab "C" using Lever rule and Scheil equation.

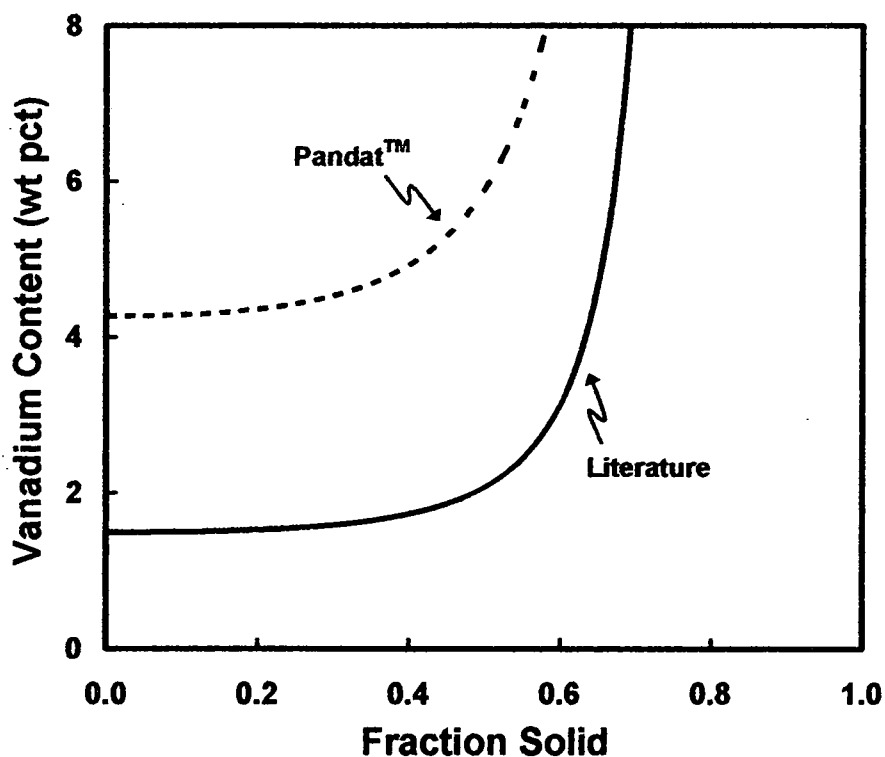


Figure 62. Predicted vanadium segregation for slab "C" using the LSRE.

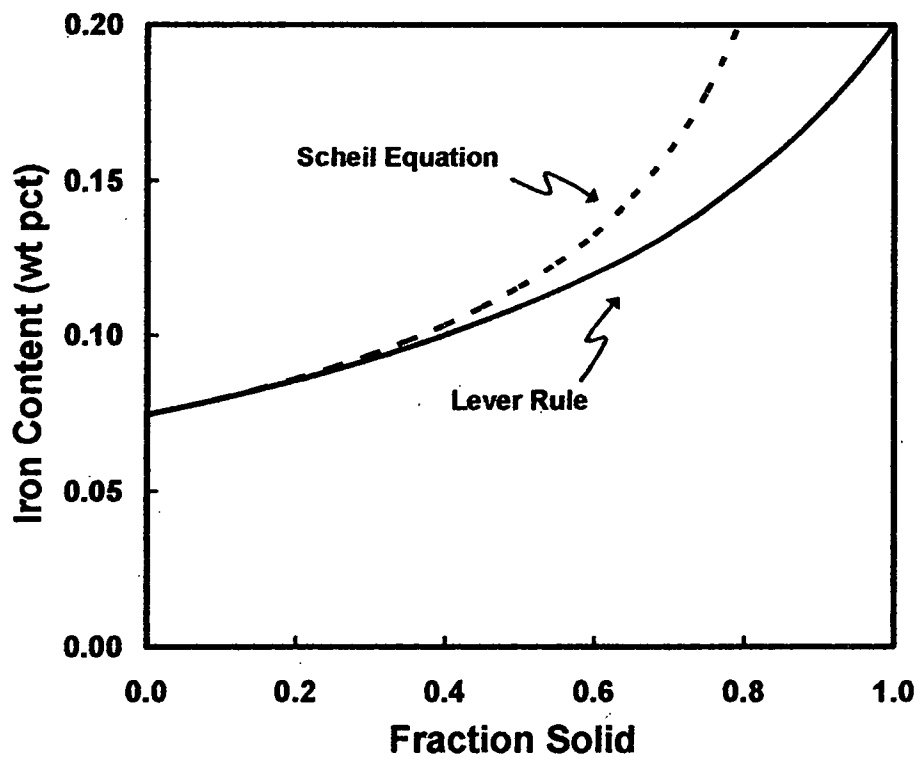


Figure 63. Predicted iron segregation for slab "C" using Lever rule and Scheil equation.

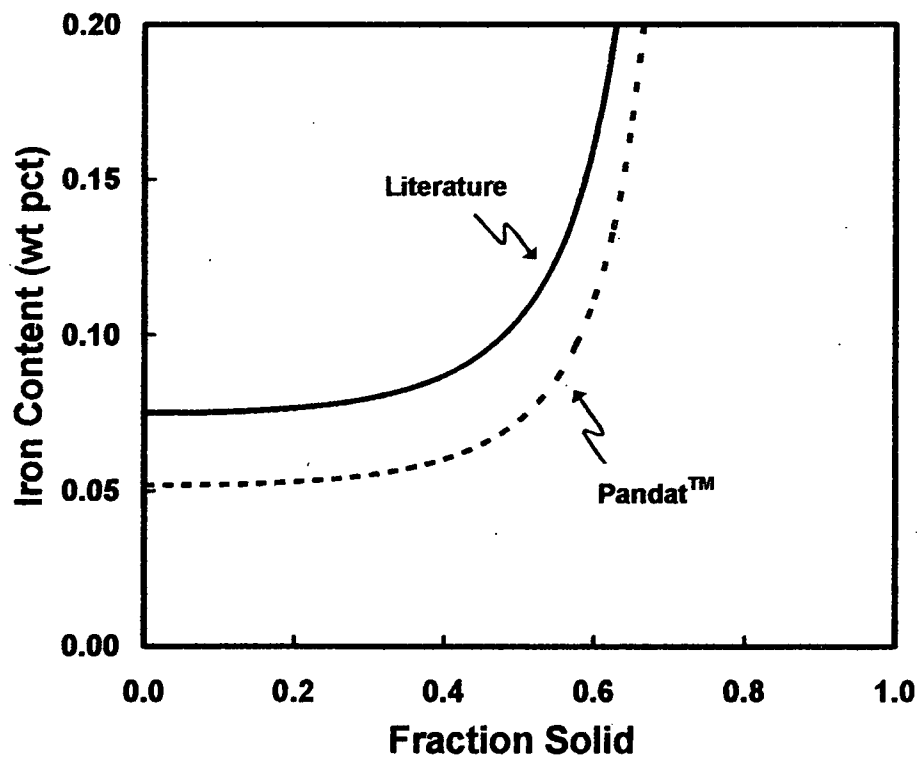


Figure 64. Predicted iron segregation for slab "C" using the LSRE.

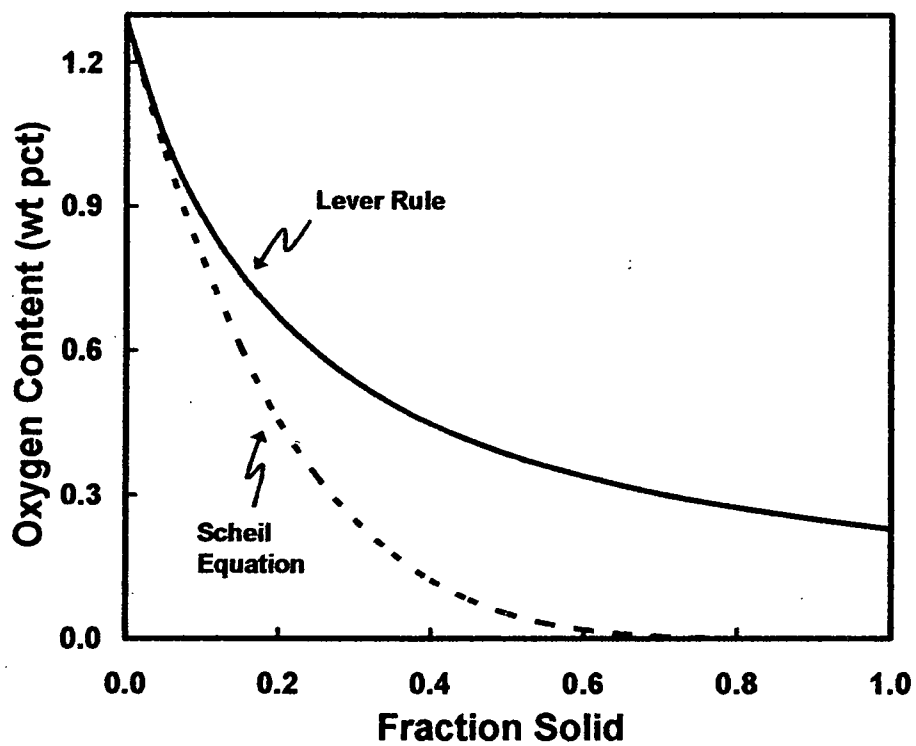


Figure 65. Predicted oxygen segregation for slab "C" using Lever rule and Scheil equation.

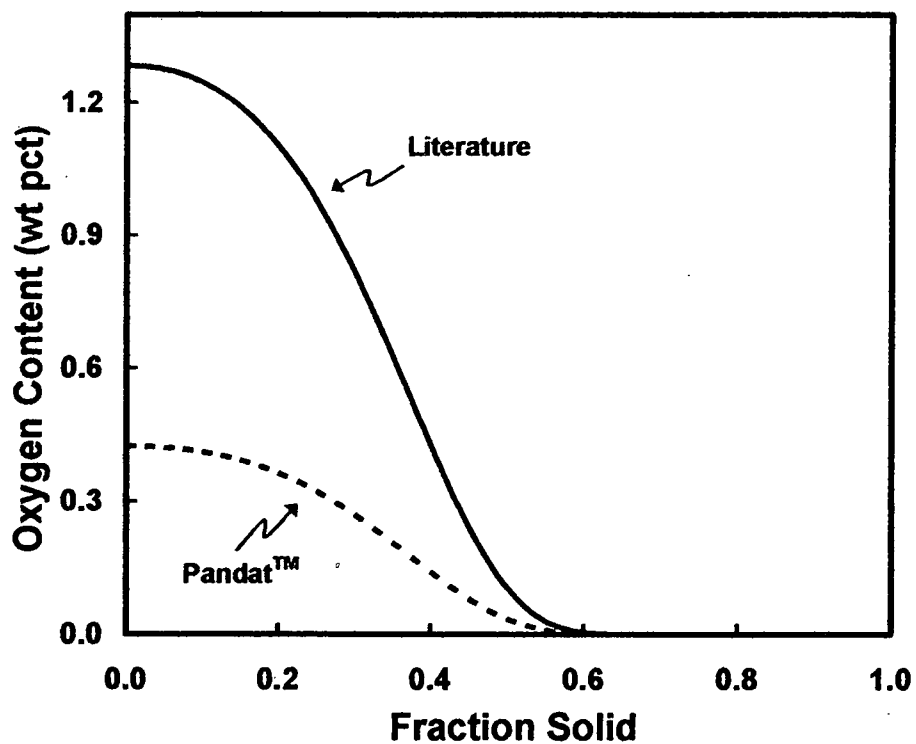


Figure 66. Predicted oxygen segregation for slab "C" using the LSRE.

6.6 Conclusions

Segregation modeling was completed using both straightforward analytical models as well as a numerical model to predict production-scale segregation. A sensitivity analysis was completed on the LSRE, an analytical model. The parameters that had the most impact on the tendency for segregation were the partition coefficient and the length of the mushy zone. This observation emphasizes the importance of determining the correct partition coefficients and mushy zone length for segregation prediction using the LSRE, limiting case five. Increasing the length of the mushy zone decreased the usefulness of the LSRE for segregation prediction.

The tendency for segregation in the middle slab using microsegregation equations was different than that of the LSRE. Both the Scheil model and the LSRE became unstable. The LSRE became unstable at approximately 0.55 to 0.60 fraction solidified, and the Scheil model became unstable near or before this range for all solutes. Solute aluminum, vanadium, and iron exhibited a tendency for positive segregation over the course of solidification while oxygen exhibited a tendency for negative segregation.

CHAPTER VII

CONCLUSIONS AND FUTURE WORK

Conclusions and ideas for future work are outlined in this section.

7.1 Conclusions

A reliable method for determination of the freezing range for Ti-6Al-4V was developed. Thermal analysis established that iron and oxygen content impacted the freezing range of Ti-6Al-4V. A definitive relationship, however, between iron content, oxygen content and freezing range was not determined. Aluminum loss was a potential complication to the thermal analysis measurements. Measured values of solidus and liquidus temperatures and freezing range did not confirm the predicted values from the thermodynamic calculations. Overall, freezing ranges trends were similar for the two data sets (measured and predicted).

Chemical distribution was measured across a production-scale ingot, a task not usually undertaken. Solute distribution across the radius, of the Ti-6Al-4V ingot, varied from slab to slab and within individual slabs for all solutes considered. Solute distribution also varied at the two axial locations in the small-scale ingots. Definitive trends were not determined from the ingot chemical distribution plots. While some segregation was apparent, it was difficult to pinpoint an exact cause. Also, a relationship between iron and oxygen distribution was not established.

Sensitive parameters used in segregation modeling with the LSRE were the partition coefficients and the mushy zone length.

7.2 Future Work

There are a few tasks that would enhance the results. Additional thermal analysis testing could be completed to determine at what point the freezing range trends become more defined. Adding another set of button melts having an oxygen concentration of 0.15 would be beneficial as well. Chemical analysis should be completed on a full set of ingot specimens that cover the breakdown steps.

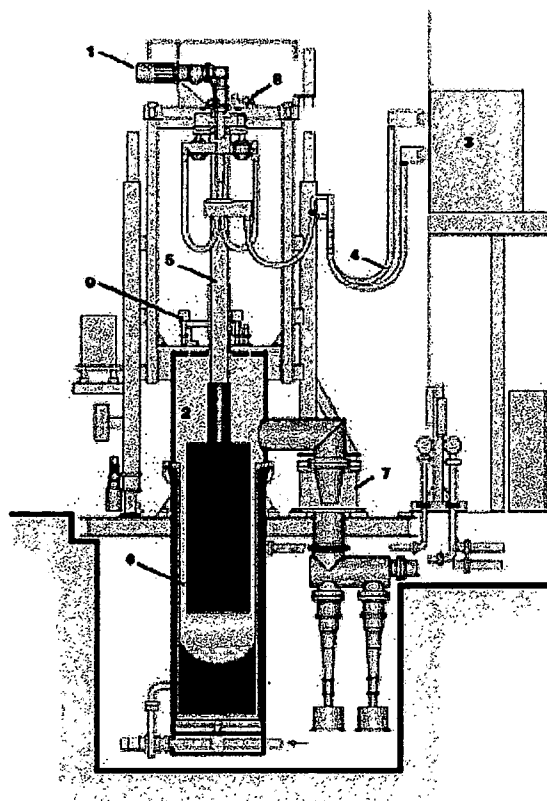
APPENDIX A

CASTING OF TITANIUM ALLOYS

A.1 Ingot Casting

A.1.1 Vacuum Arc Remelting

Both titanium ingots and titanium alloy ingots are usually produced via the VAR process. As the name suggests, the process is conducted under vacuum or, in certain cases, under low partial pressure of argon. The VAR process includes melting and remelting a consumable electrode with a dc arc [59]. The molten metal collects and subsequently solidifies in a water-cooled copper mold. The ingots are melted twice in order to meet homogeneity criteria. In certain cases, a third melting step is added to achieve a greater degree of refinement. This third melt potentially provides better chemical homogeneity and physical structure as well as further reducing any oxygen-rich and nitrogen-rich inclusions [13]. These inclusions are undesirable because they can lead to material failure.



- | | |
|------------------------|------------------------------|
| 1 Electrode feed drive | 6 Water jacket with crucible |
| 2 Furnace chamber | 7 Vacuum suction port |
| 3 Melting power supply | 8 X-Y adjustment |
| 4 Busbars/cables | 9 Load cell system |
| 5 Electrode ram | |

Figure 67. Schematic of a vacuum arc remelting (VAR) furnace [60].

The hot top step is carried out after the consumable electrode is reduced to a specified weight [59]. The power to the furnace is slowly throttled back, and the solidification front feeds the solidification shrinkage. In other words, the hot top step minimizes pipe cavity that results from alloy shrinkage.

There are several advantages of the VAR process. One such advantage is the ability to remove any unwanted gases, like hydrogen and nitrogen, which may dissolve in the molten alloy. VAR minimizes the amount of any unwanted trace component that has a high vapor pressure, and segregation is minimized but not eliminated [59]. Also, a wide-variety of alloy compositions can be achieved with the VAR process [61].

There are several disadvantages of the VAR process as well. These include the necessity of high quality of electrodes and complex equipment, costly electrode preparation, and high capital costs. Making chemical corrections during melting is very difficult and the entire process is lengthy [62].

A.1.2 Electron Beam Melting and Casting

Electron beam melting and casting is another method for producing titanium alloy ingots. High-energy electrons impinge the feedstock metal to provide energy required for melting. Similar to the VAR process, electron beam melting takes place under vacuum. Like VAR, this process sometimes employs a water-cooled copper crucible. Depending on the size of the casting a ladle, trough, or hearth may be used instead of the crucible [61].

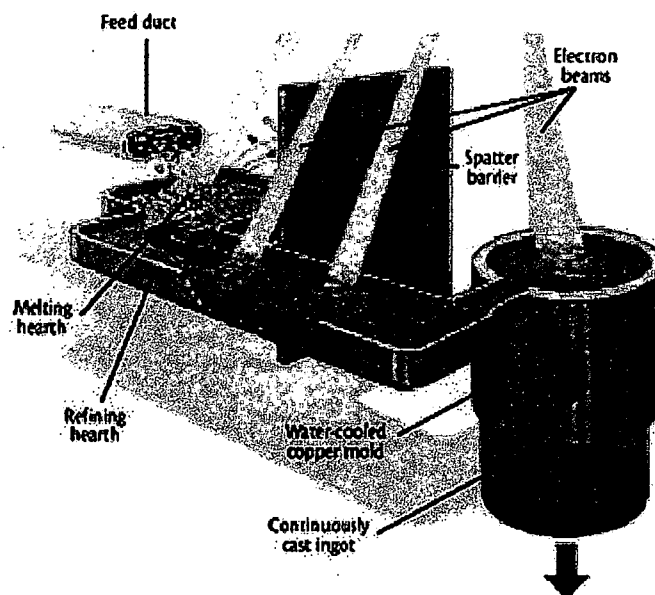


Figure 68. Schematic of the electron beam melting process [63].

There are several advantages and disadvantages of electron beam melting compared to the VAR process. The feedstock is less expensive to prepare for electron

beam since a consumable electrode is not needed. Both processes have low energy consumption and allow for a wide range of alloying. A variety of cast parts can be created via electron beam melting (slabs, ingots, and rods), while VAR produces only round ingots. High-density inclusions can be refined in electron beam melting, but the VAR process can only achieve limited refining. Also, capital cost of the furnace utilized in electron beam melting is very high. Material losses are also an issue with electron beam melting [61].

A.1.3 Plasma Arc Melting

Plasma arc melting (PAM) is another casting method utilized to produce ingots, slabs, castings, and powders. Like VAR, PAM requires use of an electric arc. The electric arc, however, is not used to melt alloy material directly as it would with a consumable electrode. Instead, the arc is used to produce plasma with sufficient thermal energy to melt the alloy material [64]. Similar to the other processes, the mold is water-cooled and the furnace contains a vacuum pump. The PAM process, however, is not usually conducted under vacuum. Typically, it is conducted around or just above atmospheric pressure. A vacuum is applied prior to backfilling the furnace. The plasma generator or plasma torch produces the plasma, which subsequently melts the feed material.

Some plasma cold-hearth melting furnaces utilize two (Figure 69) or more plasma torches. The alloy components are fed into a water-cooled copper hearth within the furnace. This hearth is similar to a water-cooled copper crucible, except it is much larger. Inside the hearth, a plasma torch is utilized to melt the solid feed material. The molten metal then moves over the trough edge and falls into a water-cooled crucible where it solidifies into the desired shape [64].

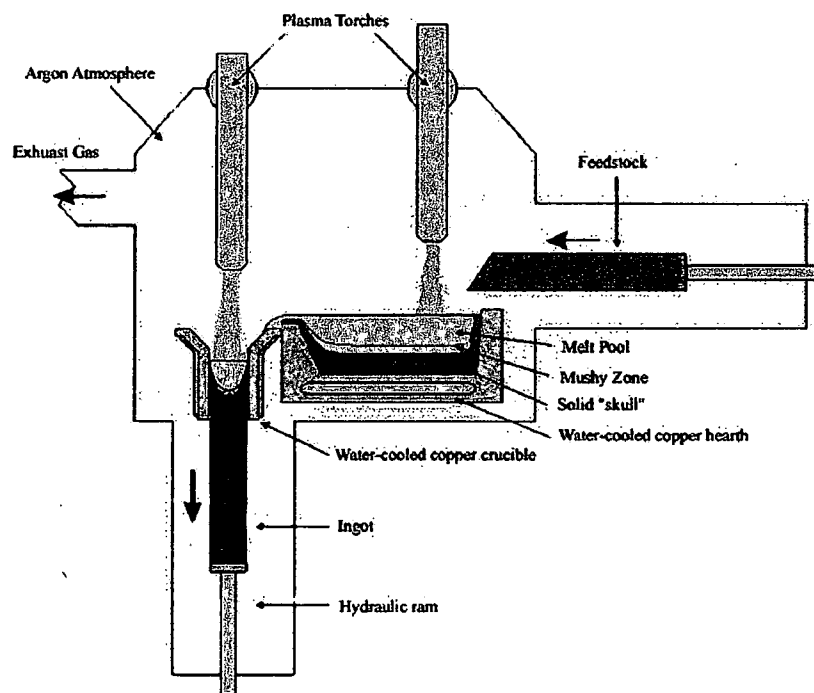


Figure 69. Schematic of a plasma arc furnace [65].

The PAM process has several advantages and disadvantages compared to VAR. One drawback is the possibility for oxygen and nitrogen to enter the PAM furnace if the vacuum seal is not tight. These inclusions can contaminate the resulting product. Another source of contamination is trapped wet gases in alloy feed material.

An alternative use of PAM is to produce a consumable electrode to be cast via the VAR process. This process prevents the presence of inclusions like titanium nitride in both the consumable electrode and VAR product. One disadvantage is complete melting may not be achieved due to the solid-liquid interface trapping solid material [66].

A.1.4 Induction Skull Melting

Induction skull melting is used to melt reactive metals like titanium alloys. Instead of an arc, an induction coil is used to melt alloy stock through application of a magnetic

field. The induction coil is wrapped around a segmented water-cooled copper crucible (Figure 70).

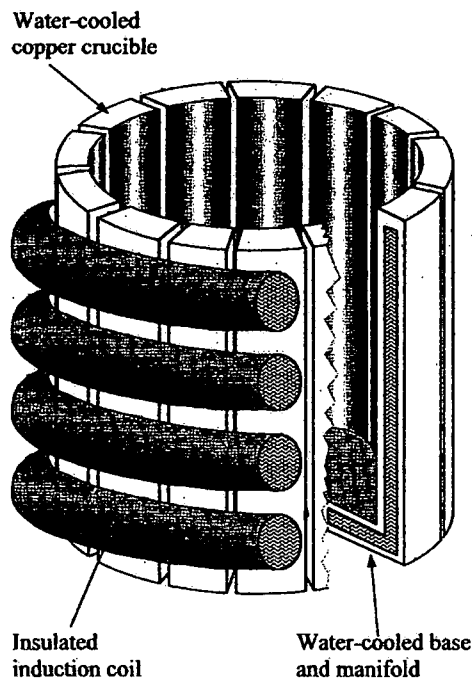


Figure 70. Schematic of a water-cooled crucible used for induction skull melting of investment castings [66].

Segments are added to prevent the crucible from being weakened or melted by the induction field in the coil [67]. The crucible is water cooled so that a shell or "skull" of metal forms on the inside of the crucible. The purpose of the skull is to prevent the crucible from contaminating the melt. A crucible with an existing skull can be used as long as the skull is compatible with the alloying material.

The melt stock; scrap, virgin, and revert, is added to the crucible. The size and shape of the stock is only limited by crucible size. Material can also be added to the molten metal during processing. The magnetic field also serves to stir the molten metal in the crucible. After alloying additions have been completed, the melt is poured into a mold. This process is conducted under vacuum or in an inert atmosphere.

One advantage of the ISM process is that oxygen content can be carefully controlled. The ISM process uses scrap and reverted titanium as melt stock which is less expensive than producing a consumable electrode [67]. Other advantages of ISM over VAR include more alloying freedom and easier production of non-standard titanium alloys. The ISM process can be scaled to meet research laboratory needs [67].

Disadvantages of the ISM process include difficulty filling thin molds and bubbles caused by rapid pouring [66]. The casting can be hot isostatically pressed (HIPped) to remove the entrapped bubbles, however, this process significantly increases production costs. Also, only small ingots can be produce via ISM (up to several hundred pounds), while VAR, PAM, and electron beam melting can produce much larger ingots (up to approximately 35, 000 pounds) [68].

A.2 Investment Casting

Investment casting is a multi-step process used to make complex aircraft components. The overall process steps include pattern-making, mold-making, casting, and post-casting operations. These major steps are summarized briefly.

The first step in investment casting is to produce a wax or plastic pattern. A pattern may be machined if only a small number of parts need be produced. Wax blends are most commonly used. The wax is blended to improve strength, rigidity, and/or dimensional stability [69]. Several types of waxes are used in the blends: paraffin, microcrystalline, ozocerite, candelilla, carnauba, and beeswax. The desired material is injected into a metal, plastic, rubber, or plaster mold in liquid, semi-solid, or solid form. The patterns are assembled after production using wax welding for wax patterns or solvent welding for plastic patterns.

A ceramic slurry is applied to the assembled pattern. The pattern is dipped into fine slurry, allowed to drain, stuccoed with coarse ceramic material, and hardened.

These steps are repeated to achieve the desired mold thickness. The pattern is then removed from its ceramic shell mold, and the mold is fired to remove moisture and residual pattern material.

The most common melting method for titanium is vacuum arc skull melting. This method is similar to the VAR process in that a consumable electrode is melted under vacuum into a water-cooled copper crucible. The difference is that the skull covers the inside of the crucible. A billet is usually used as the consumable electrode.

Post-casting or finishing operations may include knockout, cutoff, core removal, heat treatment, and abrasive cleaning. Hot isostatic pressing (HIP) is often completed as a post-casting step for titanium. This step is intended to eliminate porosity and improve mechanical properties and their distribution [69]. After finishing operations, testing and inspection procedures are conducted.

A benefit of investment casting is that complex parts can be created as well as those having very thin walls. A disadvantage of this process is the cost of post-casting operations, which can account for over fifty percent of production costs [69]. These operations are necessary, however, to ensure that quality standards are met.

A.3 Button Melting

Vacuum arc melting (VAM), PAM, and electron beam melting, are utilized to produce laboratory-scale button or cigar melts, named for their respective shapes. These melts usually range from approximately 50 to 250 g in size. Solid pieces of metal are placed in an open-cavity water-cooled copper mold. For VAM, an electric arc is utilized to melt the metallic pieces, under a vacuum. The buttons are rotated between subsequent melts in order to ensure chemical homogeneity. Button melts are utilized in the lab to mimic industrial practice and to determine the effects subsequent processing

has on an alloy created via VAM. VAR, PAM, or electron beam melting depending on the casting process used [68, 70].

APPENDIX B

NETZSCH INSTRUMENT MODEL STA 409 CD

B.1 Instrument Overview

The furnace in the Netzsch STA 409 CD is capable of outputting 5 kW. Two furnace tubes are available for use with the instrument. The aluminum oxide tube can withstand temperatures up to 1700°C and heating rates up to 40 K per minute. The carbon tube can withstand temperatures up to 2000°C and heating rates up to 100 K per minute. The carbon tube is rated to 2400°C, but the power supply in the University of Wisconsin-Madison lab is limiting. Furnace tubes are cleaned regularly.

The sample carrier is tungsten rhenium, and the thermocouple wires are tungsten-3 pct rhenium vs. tungsten-25 pct rhenium. Helium is the purge gas (purity 99.99999 pct), and it is run through a getter first to remove any oxygen that may have entered the stream during a tank change. The getter consists of three quartz tubes. After the getter, helium is bubble through vacuum oil to prevent any remaining impurities from entering the apparatus.

The apparatus is controlled via a Netzsch TASC 414/4 controller which is tuned with the instrument's software package. The instrument outputs the DTA trace, the thermogravimetric (TG) or mass change trace, and the temperature pattern. The DTA trace is measured in units of $\mu\text{V}/\text{mg}$. If calibration is completed prior to experimentation the trace can be measured in units of mW/mg . The TG trace is measured in mg and temperature pattern in degrees centigrade.



B.2 Operating Procedures

General operating procedures for operating the Netzsch STA 409 CD are outlined. These instructions are most applicable for a quick sample change after a completed run.

Place sample into container

- Place the prepared sample and reference into the DTA carrier with the sample in the front (make sure there is good contact between the crucibles and the sides of the holder).

System under vacuum

- Pull the top of the chamber around and gently close chamber. Turn the black knobs CCW until they are aligned L to R.
- Slowly open the sample/rough pump valve (red/black knob at back right).
- When the sample pressure is at a minimum (look at gauge → vacuum gauge shows numbers),  turn on turbo pump, button on the Pfeiffer vacuum display. If the pump stays at zero Hz,  button will clear the error. If the pump is not working, quickly open and close a valve to get air moving through the system. (Try the sample gas valve in the front.) Wait to start a run until the turbo pump vacuum reaches 5×10^{-5} torr.
- Now the furnace needs to be under vacuum. Turn the "Furnace Control Gas" knob to either vacuum or off. Make sure the furnace gas valve is closed, and then turn the red and black knob of the turbo pump. If this does not work check to see that the pump is switched to the on (up) position. The furnace vacuum should get down to about 20×10^{-6} atm (close to 20 is ok and the system usually reaches that by the time the turbo pump reaches 5×10^{-5}).
- On the L of the chamber, there is an overpressure valve that always needs to be in the closed position.

System inert gases and cooling water

- The furnace gas and the sample gas use separate helium tanks because the furnace requires a much higher flow rate than does the sample.
- Under the Omega controller shelf, the furnace gas must be turned to the 2 position. The middle is the off position. The flowmeters and controller switch is located under the furnace gas control valve. The flowmeters should be on for backfill, and the controller on for control of the system.
- Turn the sample and balance gases and flowmeters on (located on the Omega controller shelf). The sample gas needs to be at least 200 psi to complete a run. If the furnace gas appears low, ask someone if it will be ok.
- The getter furnace is never turned off.
- Turn all of the cooling water valves on at the same time. Turn on the boost pump switch (up position) and open the water supply and return valves. Turn the water on (under the computer desk on the R).
- The water chiller for the balance must always be on (usually no problems with this piece of equipment).

Shutting down the vacuum pumps

- After the turbo pump reaches 5×10^{-5} , the vacuum pumps need to be turned off. Close the rough pump valve, and turn off the turbo pump using the same button that was used to turn it on. (The turbo pump will still run but will eventually slow down. If the sample mass is of great concern, then do not close the turbo pump valve until it is under 1000 Hz → normal operation is 1500 Hz.)
- Close the turbo pump valve (turbo pump sticks → turn past the rough spot). (Sometimes when the turbo pump reaches 100 Hz, it will start shaking and disturb the balance. The balance is not an issue for the Ti64 samples). If the turbo pump stalls under vacuum, check to see that the furnace vacuum is also turned on.

Finalizing Set-up

- Make sure the gas is running → Inert Only Gas Flow Control IV program on PC. Click the switch to turn the system to manual control. Press the run button (horizontal arrow pointing to the right) to turn the system on.
- Open balance valve on the back and sample valve on the front.
- Let the sample pressure get to zero (will go over because oil in system) and open the red knob valve (outlet gas flow → previously only letting gas flow into the chamber) on the L side of the chamber. Switch from flowmeters to controller (under the Omega shelf). If sample pressure is skyrocketing, close the sample and balance valve.
- Close the furnace vacuum valve.
- Turn the "Furnace Gas Control" knob to fill. Open the furnace valve inlet (not red/black knob!) and when it reaches -0.5 bar flip to dynamic control. It will overshoot the target significantly then come back down.
- The green safety light will come on and the system will have red flashing light.
- The furnace gas flow needs to be at 3-4 bars (level measurement, not units). This level is most easily adjusted on the furnace gas tank. If gas flow is at 3-4 bars and the safety light does not turn on, flip Furnace Gas Control knob to fill and back to dynamic. If the system changes from red flashing to green, it is still okay to run a sample.

Running a Sample

- Tare the balance using the computer program STA 409CD. If you want to view (or close) the furnace temperature, just type "furnace" and it will pop up (or disappear).
- Program the temperature cycle (if not already completed) and click start. The measurement type is sample.

After the conclusion of a run

- The gas can be left on to keep the lines pressurized.
- DO NOT turn on the vacuum with open lines!
- Close sample, balance, and furnace inlet/outlet valves.
- Turn on the furnace vacuum to save time between runs.
- Open the furnace valve (sample pressure at atmospheric).
- The chamber can now be opened.

APPENDIX C

EXAMPLE DTA HEATING SCHEME

Table 8. Example DTA heating scheme.

Step	Description*	Temperature (°C)	Rate (K/min)	Duration (min)
1	↑	1625	20	na
2	→	1625	na	30
3	↓	1600	-10	na
4	↑	1705	5	na
5	↓	1620	-20	na
6	→	1620	na	1
7	↑	1695	5	na
8	→	1695	na	1
9	↓	1620	-5	na
10	↑	1690	5	na
11	→	1690	na	1
12	↓	1620	-5	na
13	↑	1685	5	na
14	→	1685	na	1
15	↓	1620	-5	na
16	↑	1680	5	na
17	→	1680	na	1
18	↓	1620	-5	na
19	↑	1675	5	na
20	→	1675	na	1
21	↓	1620	-5	na
22	↑	1670	5	na
23	→	1670	na	1
24	↓	1620	-5	na
25	↓	30	-20	na
26	→	30	na	20
* ↑ = heating, ↓ = cooling, → = isothermal				

APPENDIX D

DIFFERENTIAL THERMAL ANALYSIS PLOTS

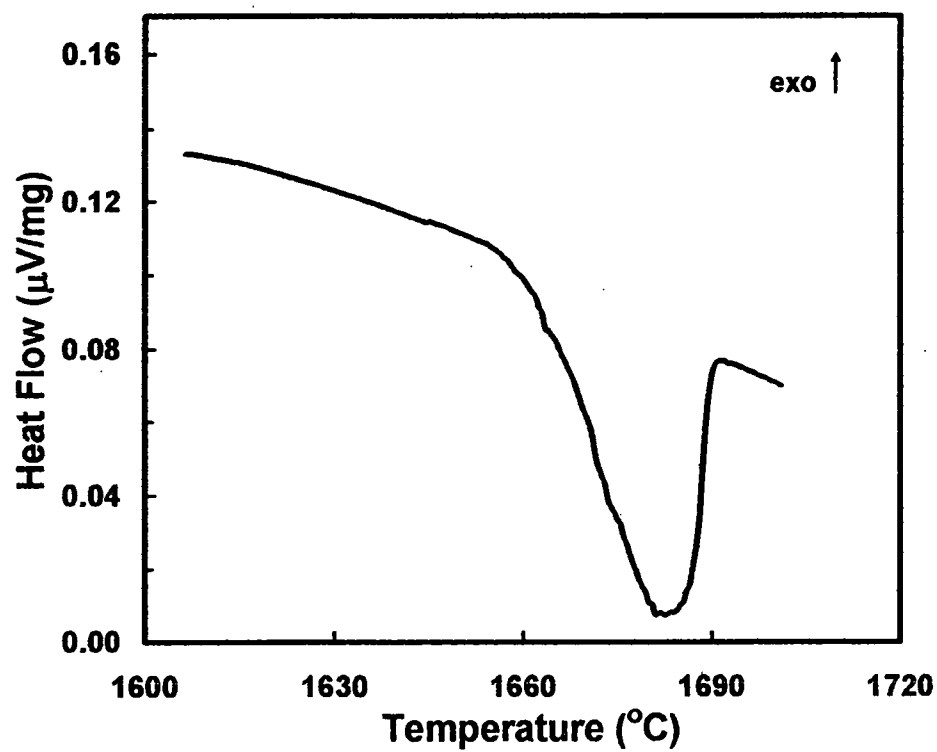


Figure 71. DTA trace used for solidus determination for alloy XB3040, trial 4.

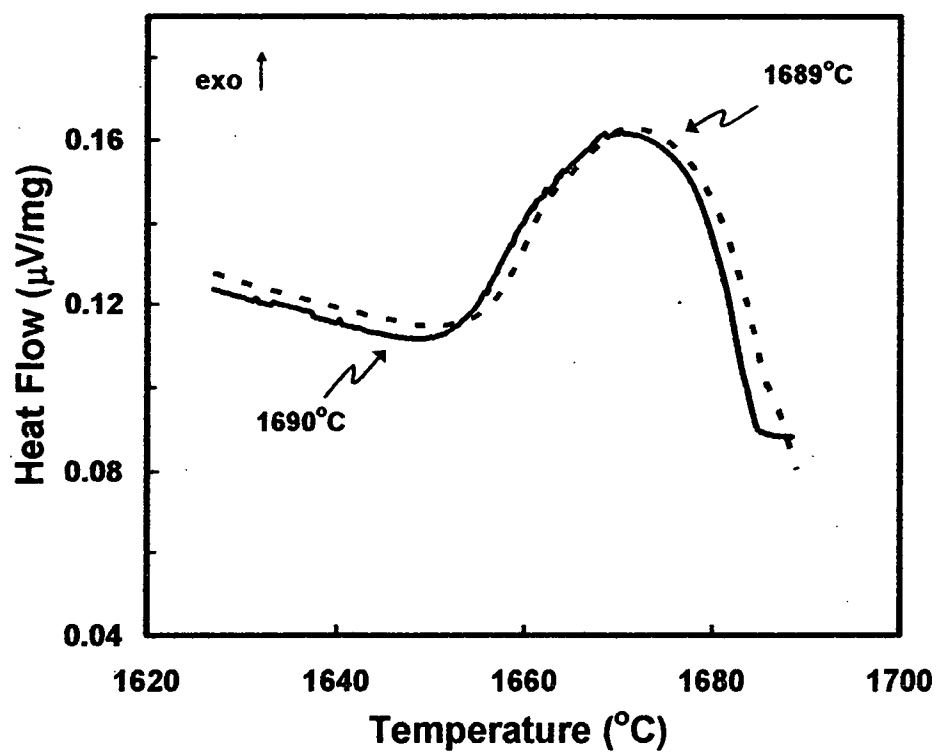


Figure 72. DTA trace used for liquidus determination for alloy XB3040, trial 4.

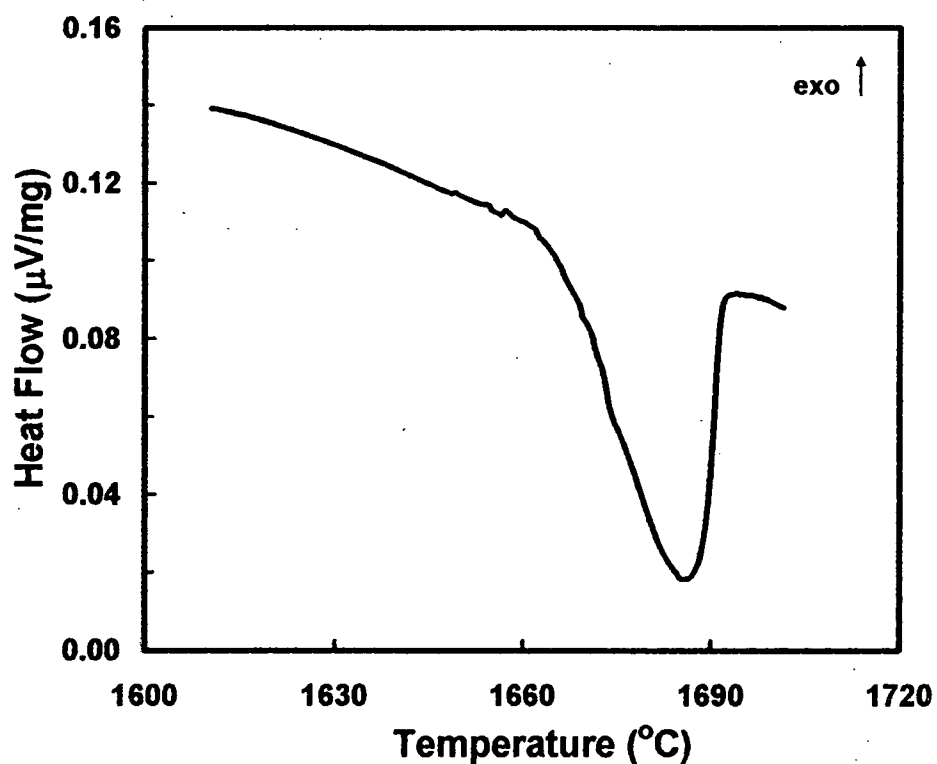


Figure 73. DTA trace used for solidus determination for alloy XB3041, trial 1.

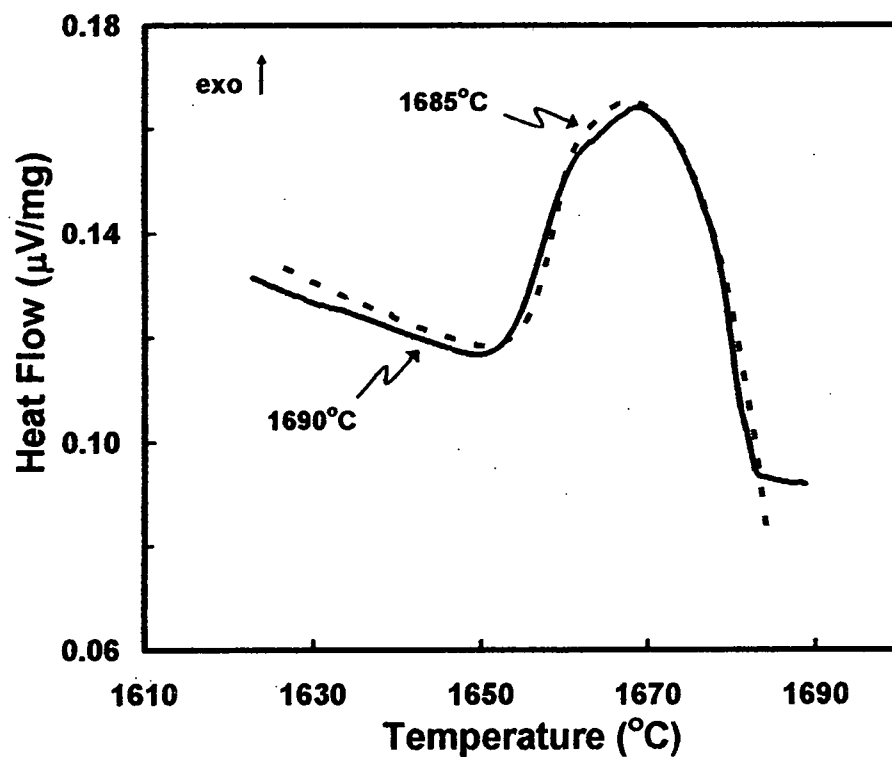


Figure 74. DTA trace used for liquidus determination for alloy XB3041, trial 1.

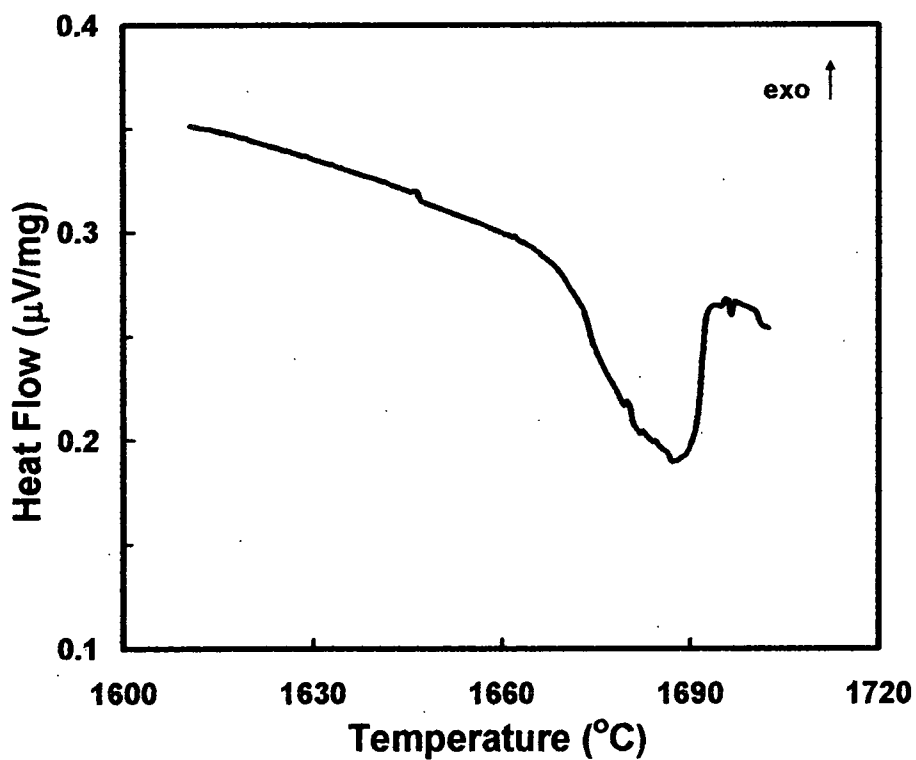


Figure 75. DTA trace used for solidus determination for alloy XB3041, trial 2.

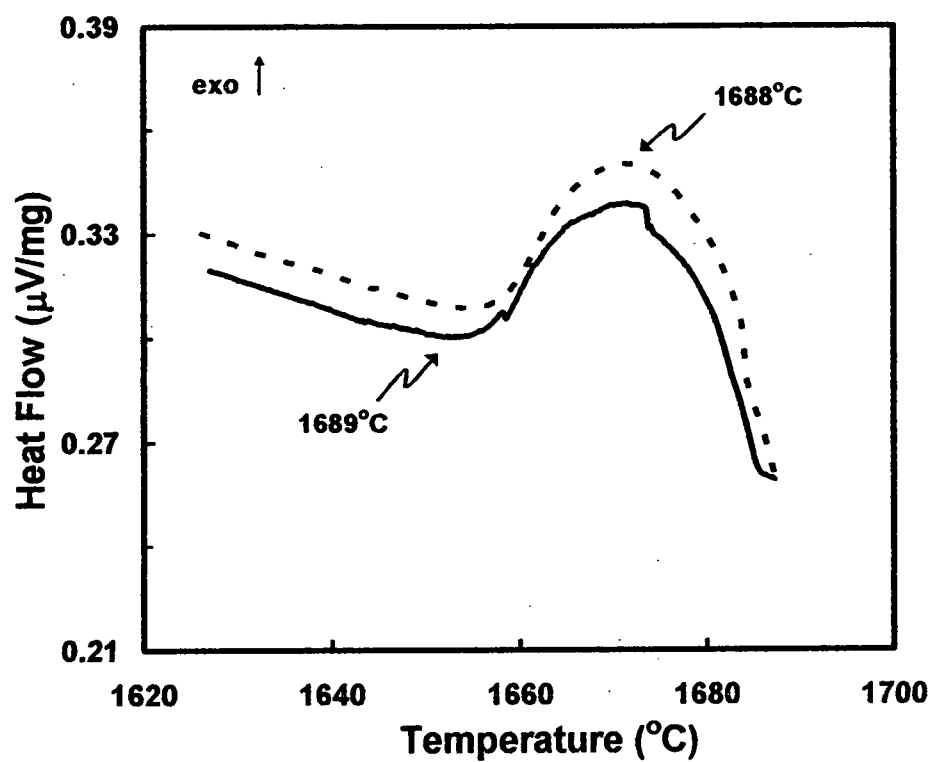


Figure 76. DTA trace used for liquidus determination for alloy XB3041, trial 2.

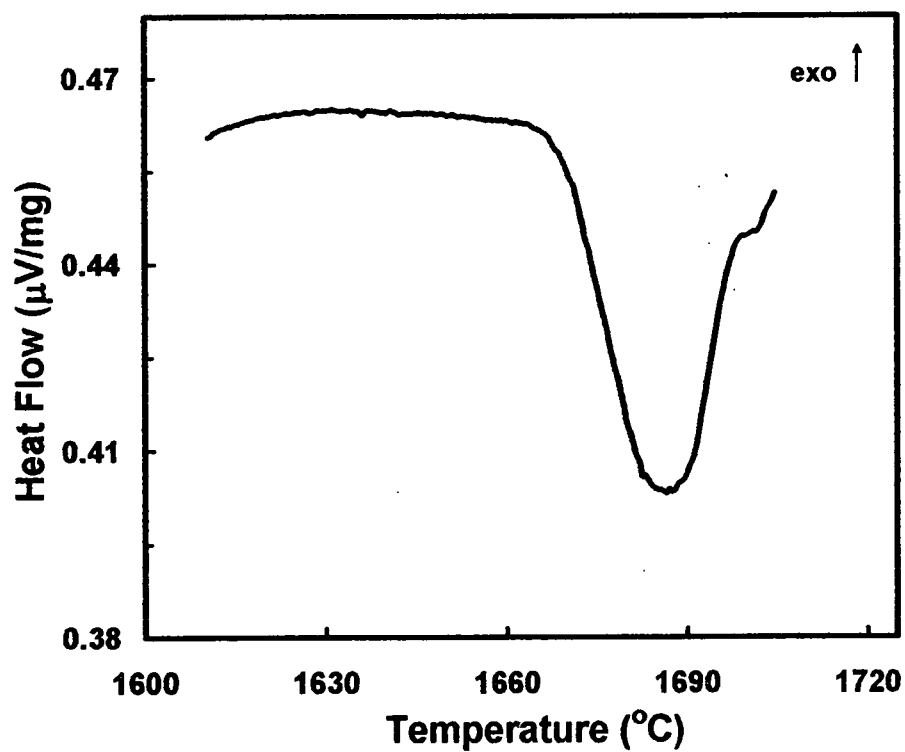


Figure 77. DTA trace used for solidus determination for alloy XB3043, trial 1.

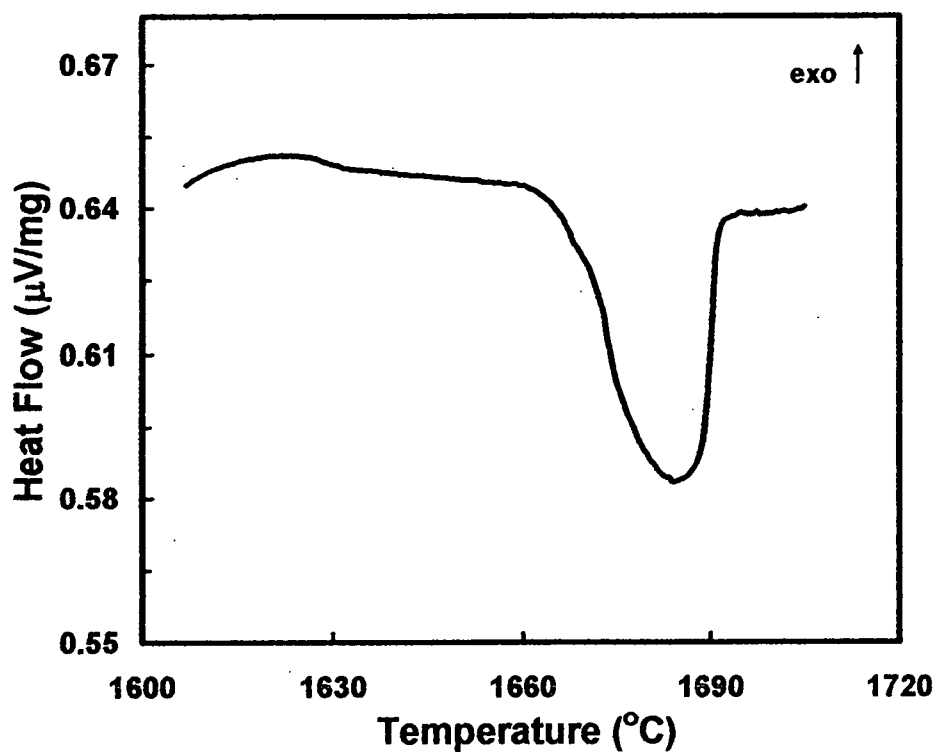


Figure 78. DTA trace used for solidus determination for alloy XB3043, trial 2.

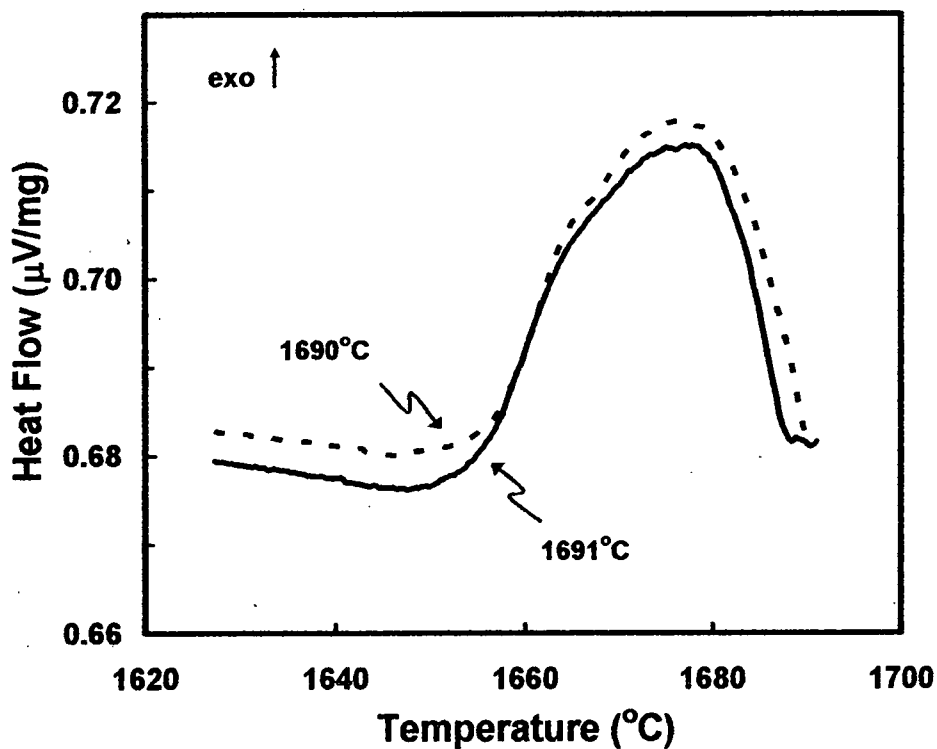


Figure 79. DTA trace used for liquidus determination for alloy XB3043, trial 2.

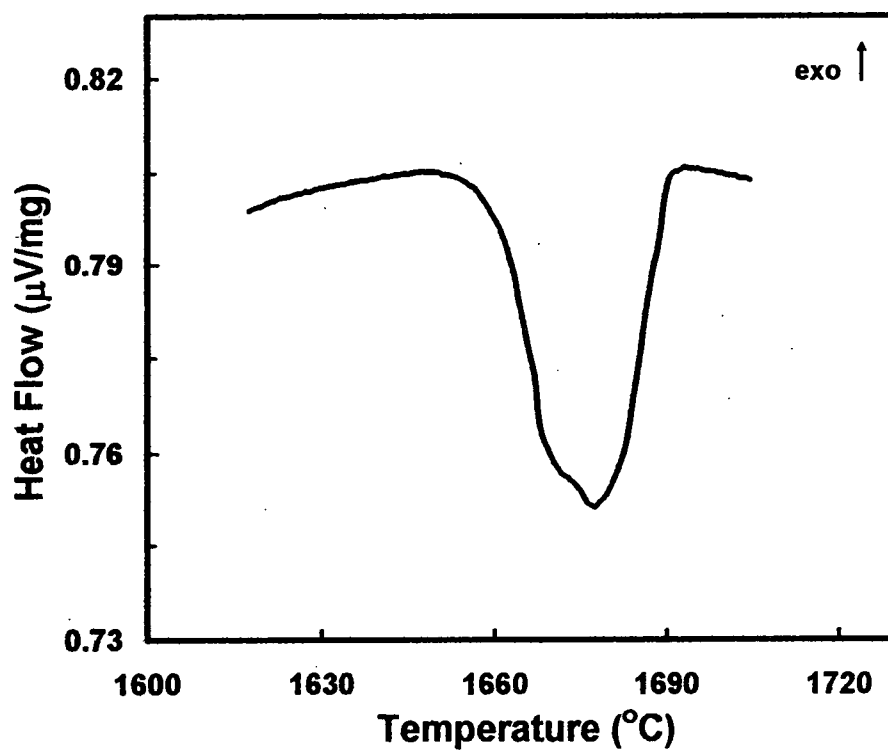


Figure 80. DTA trace used for solidus determination for alloy XB3045, trial 1.

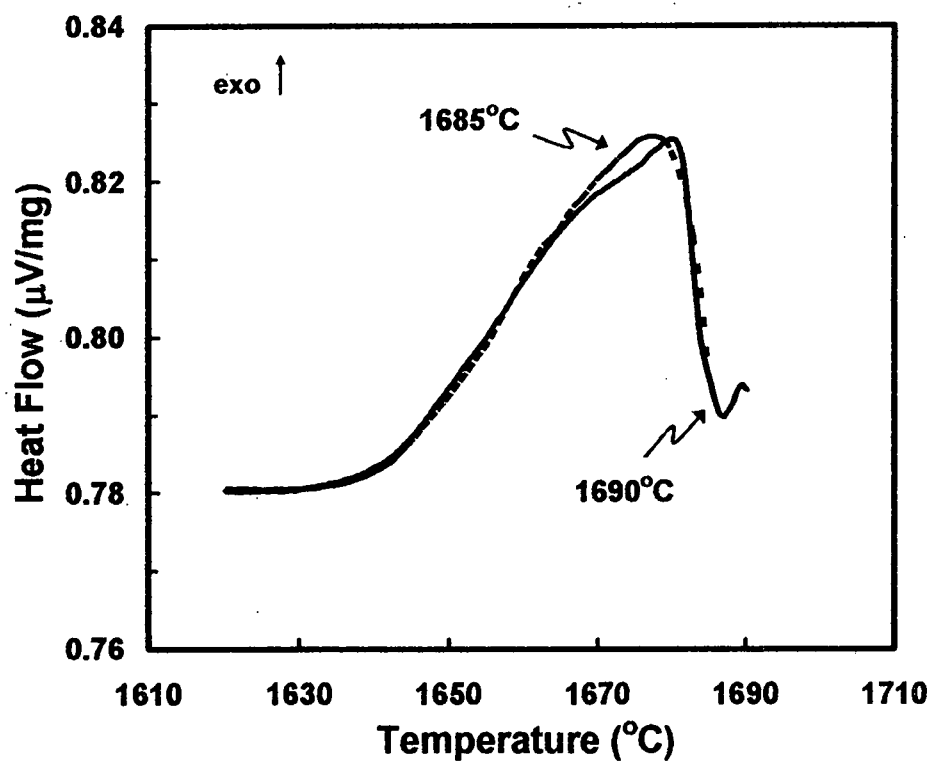


Figure 81. DTA trace used for liquidus determination of alloy XB3045, trial 1.

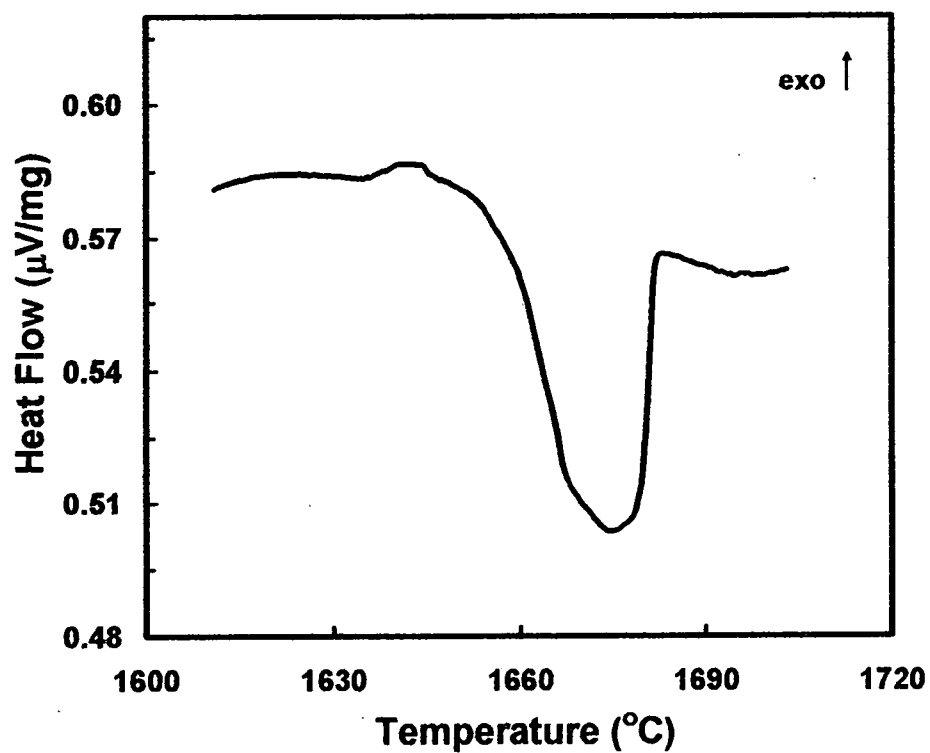


Figure 82. DTA trace used for solidus determination for alloy XB3045, trial 3.

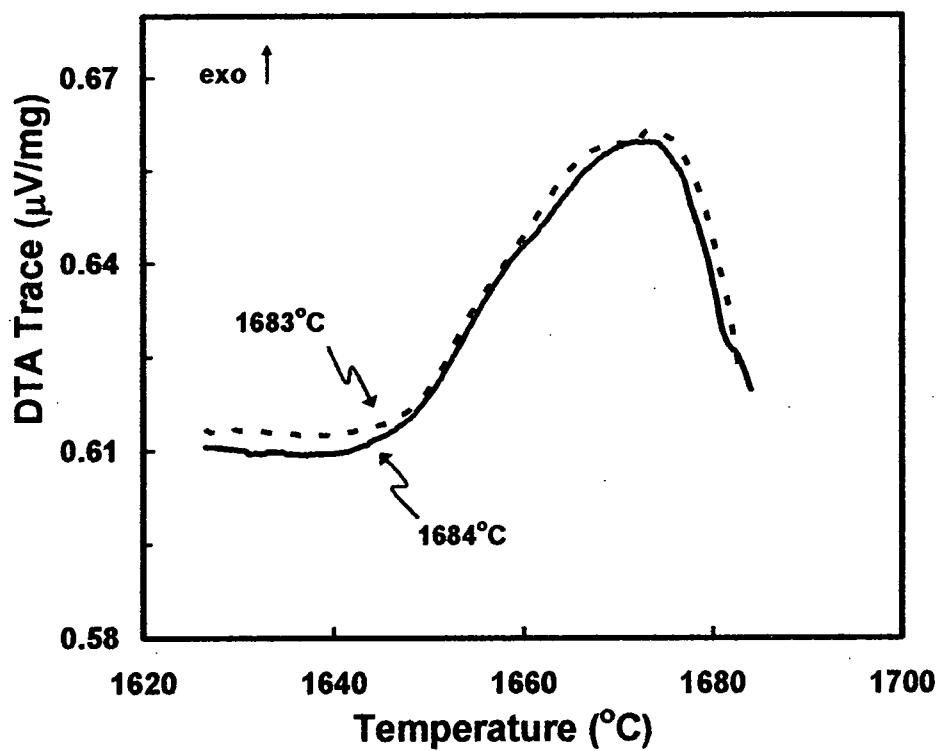


Figure 83. DTA trace used for liquidus determination of alloy XB3045, trial 3.

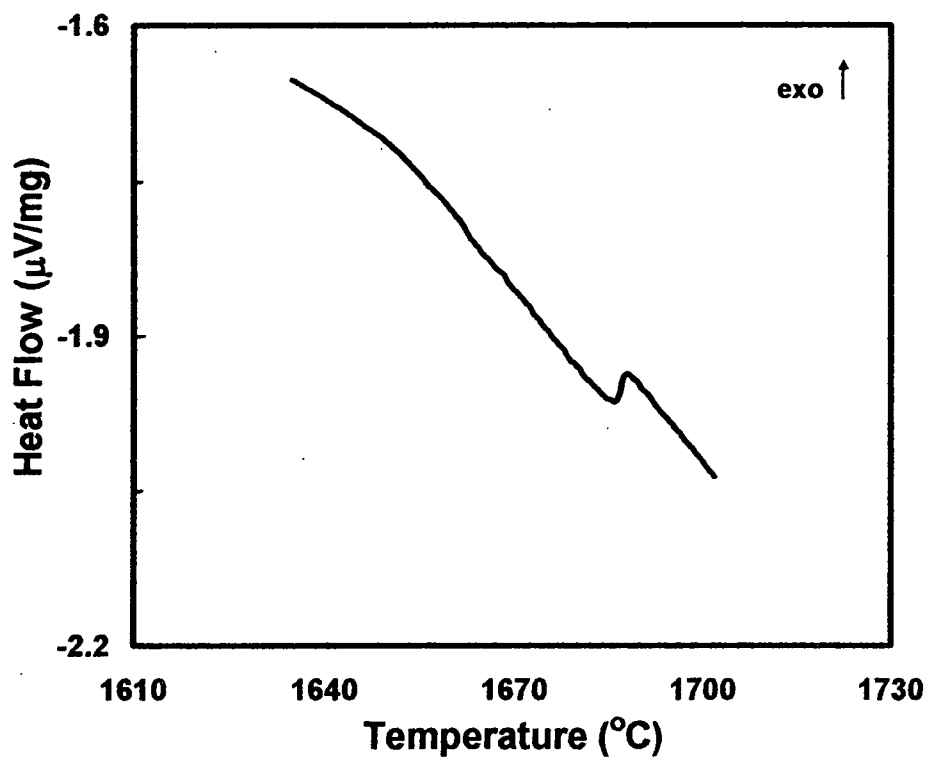


Figure 84. DTA trace used for solidus determination for alloy XB3048, trial 4.

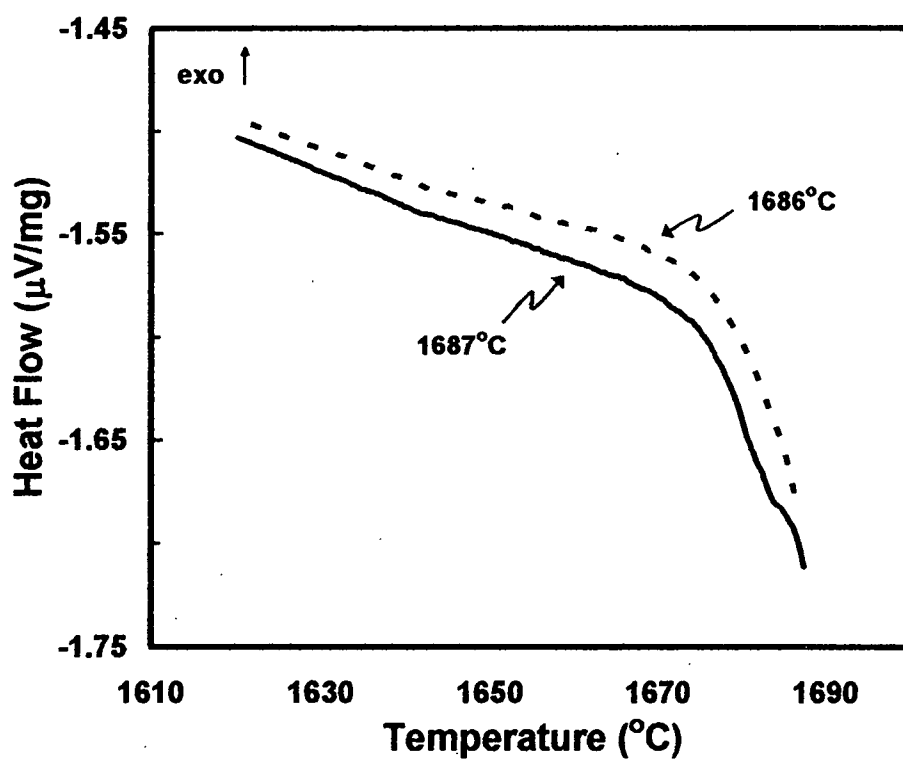


Figure 85. DTA trace used for liquidus determination of alloy XB3048, trial 4.

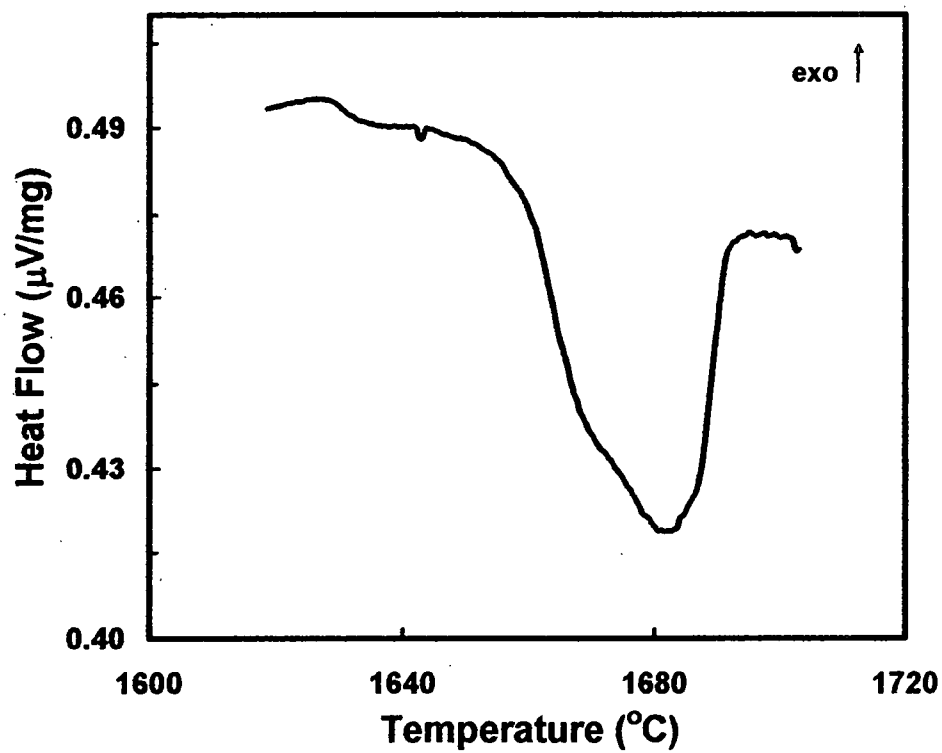


Figure 86. DTA trace used for solidus determination for alloy XB3049, trial 5.

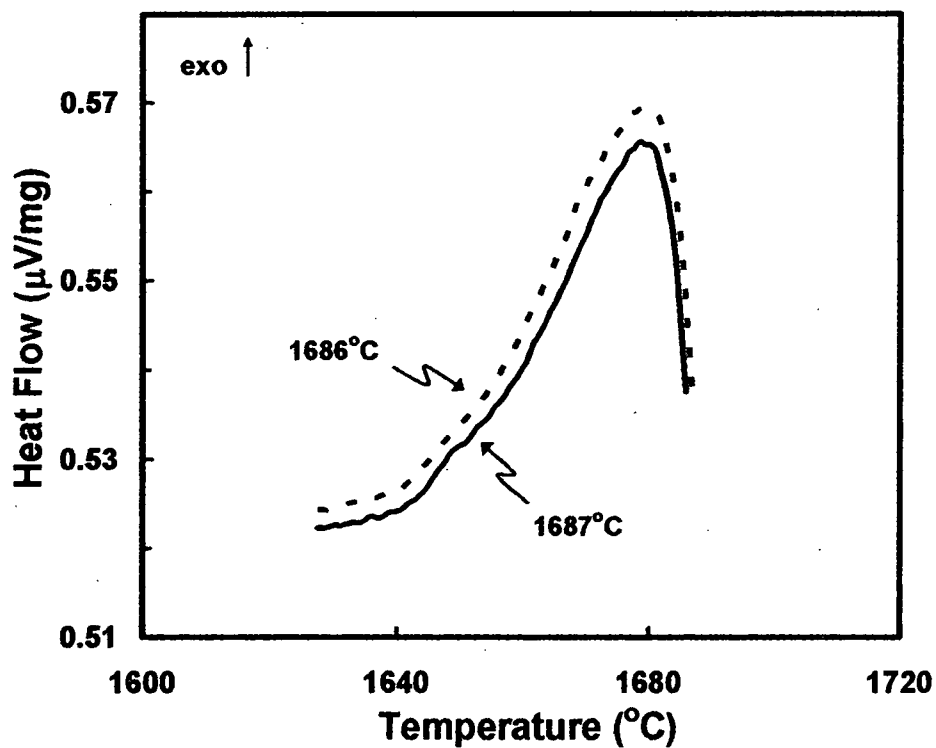
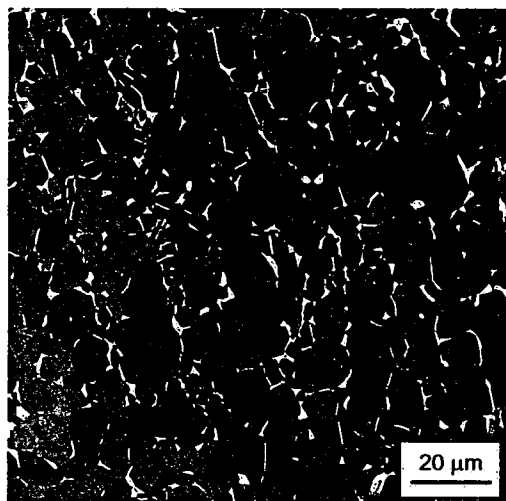


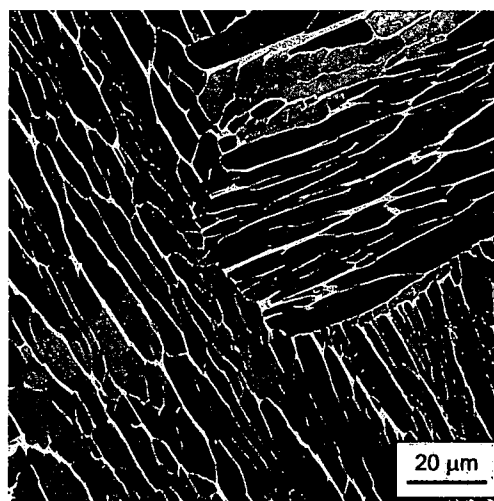
Figure 87. DTA trace used for liquidus determination of alloy XB3049, trial 5.

APPENDIX E

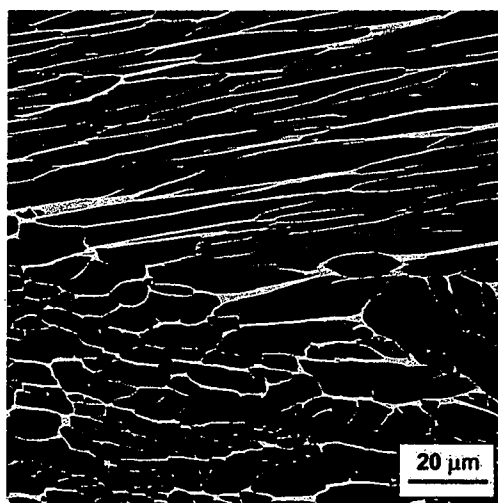
SEM BACKSCATTERED ELECTRON IMAGES



(a)

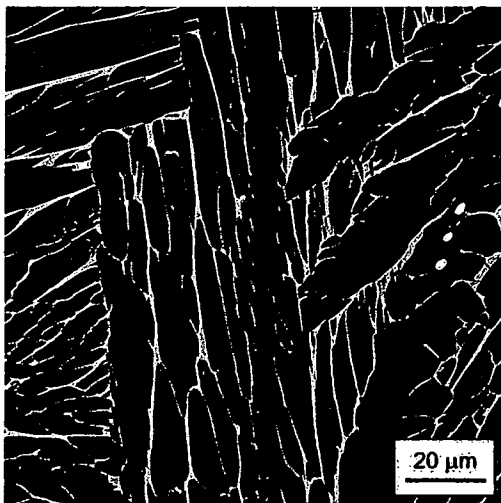


(b)

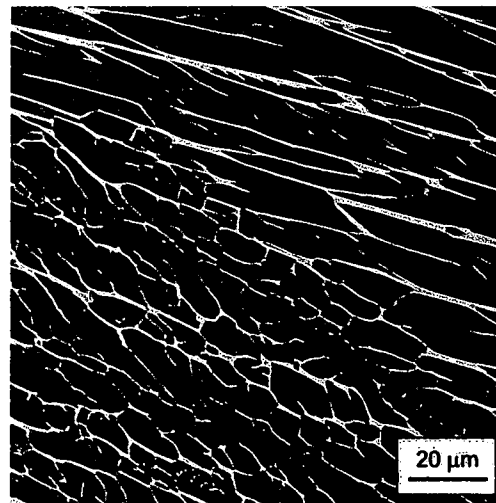


(c)

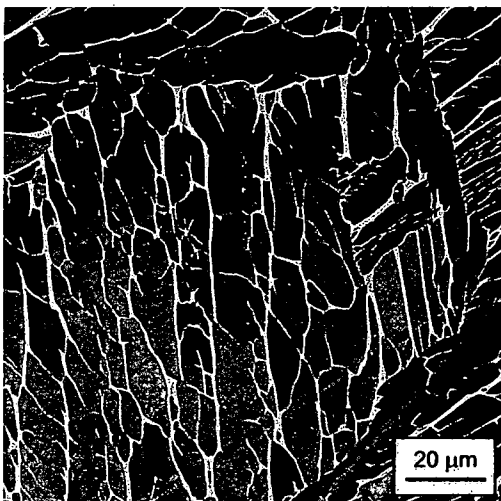
Figure 88. Microstructures of as-received (a) and post thermal analysis (b, c) samples of the baseline material. Images were taken at center (b) and edge (c) locations for baseline trial 3.



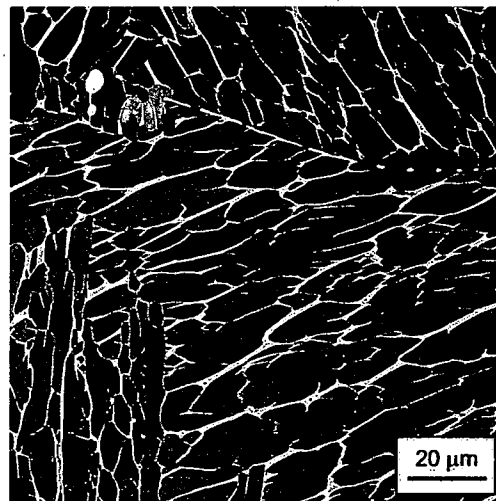
(a)



(b)

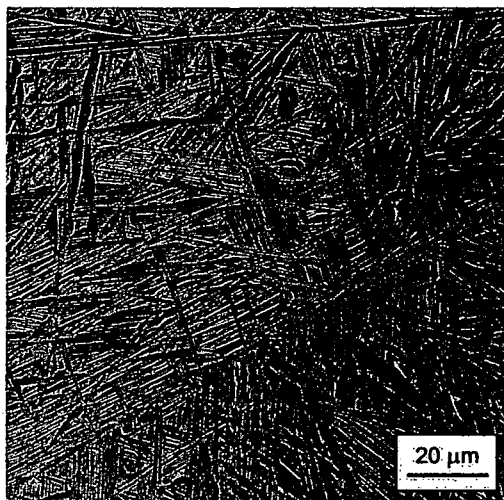


(c)

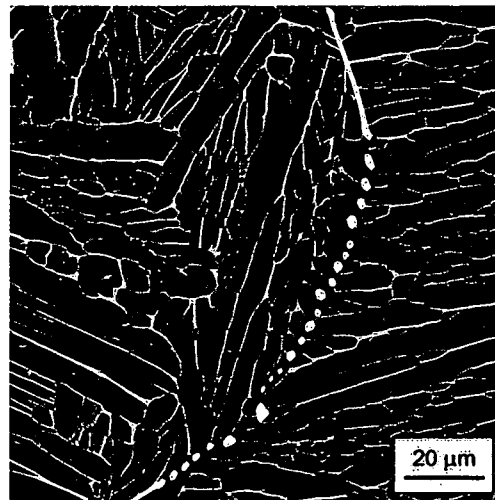


(d)

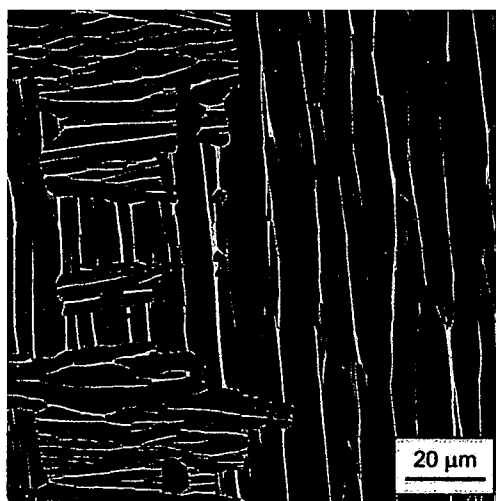
Figure 89. Microstructures of post-thermal analysis baseline samples. Images of trial 6 were taken at center (a) and edge (b) locations. Images of trial 7 were taken at center (c) and edge (d) locations.



(a)

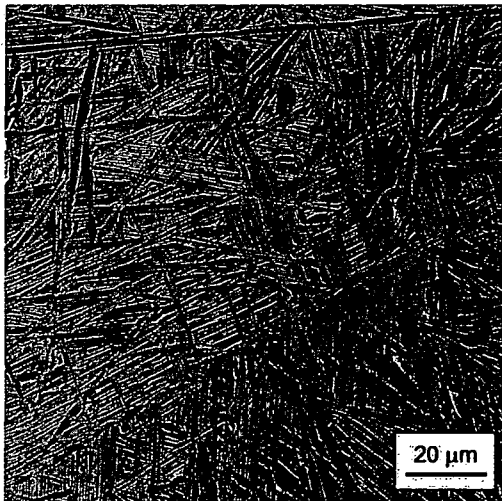


(b)

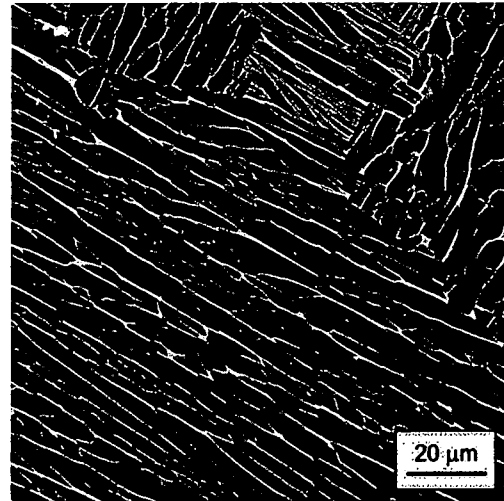


(c)

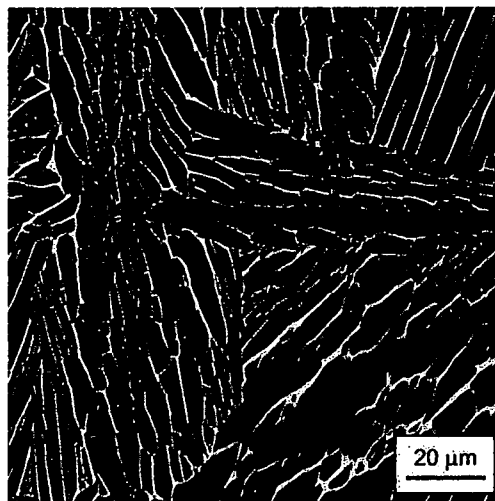
Figure 90. Microstructures of as received (a) and post-thermal analysis (b, c) samples of alloy XB3040. Images of trial 4 were taken at center (b) and edge (c) locations.



(a)

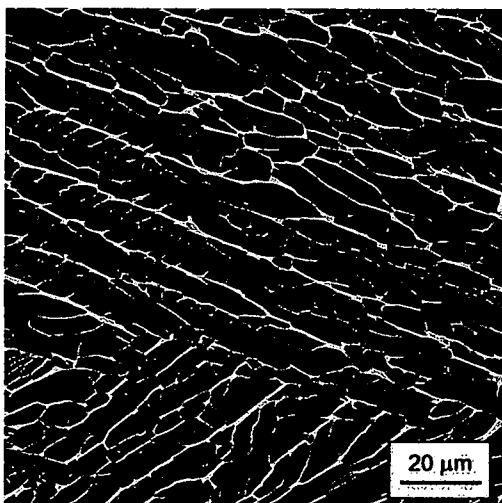


(b)

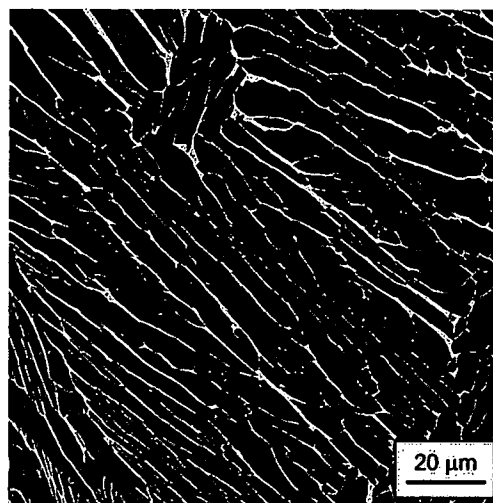


(c)

Figure 91. Microstructures of as-received (a) and post-thermal analysis (b, c) samples of alloy XB3041. Images were taken at center (b) and edge (c) locations for trial 1.

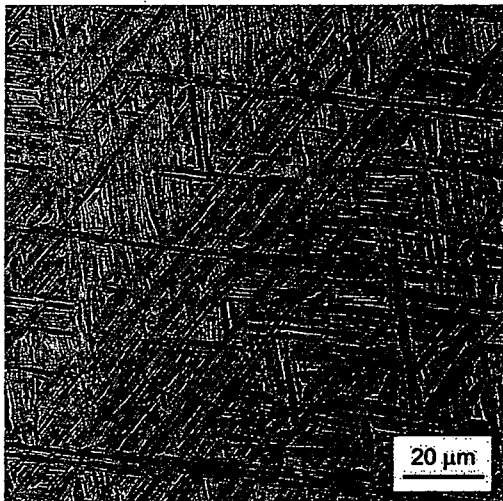


(a)

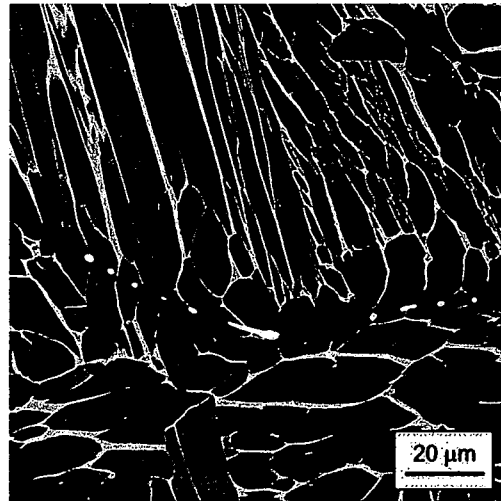


(b)

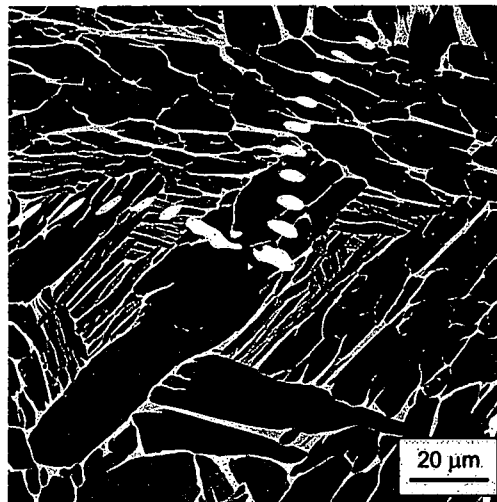
Figure 92. Microstructures of post-thermal analysis XB3041 alloy sample, trial 2. Images were taken at center (a) and edge (b) locations.



(a)

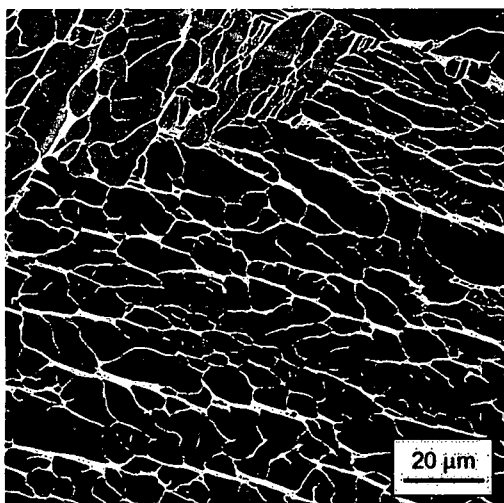


(b)

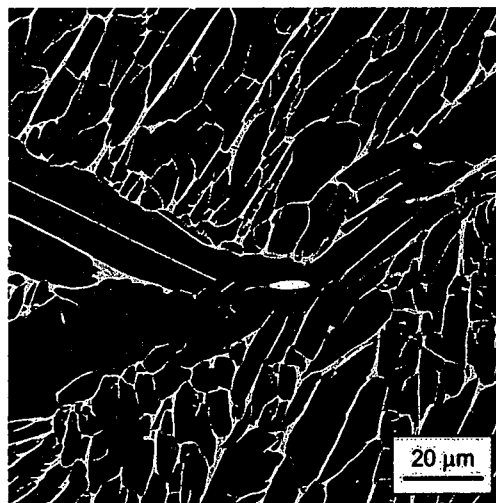


(c)

Figure 93. Microstructures of as-received (a) and post-thermal analysis (b, c) samples of alloy XB3043. Images were taken at center (b) and edge (c) locations for trial 1.

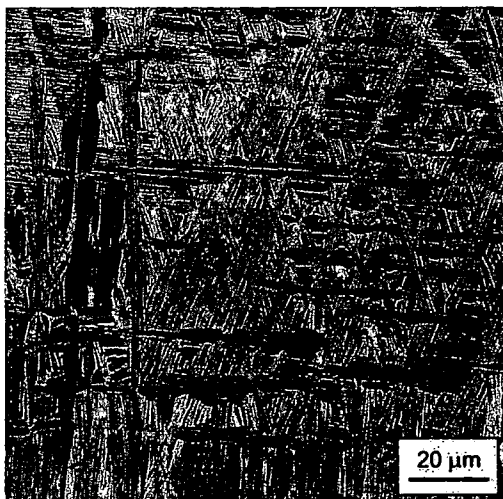


(a)

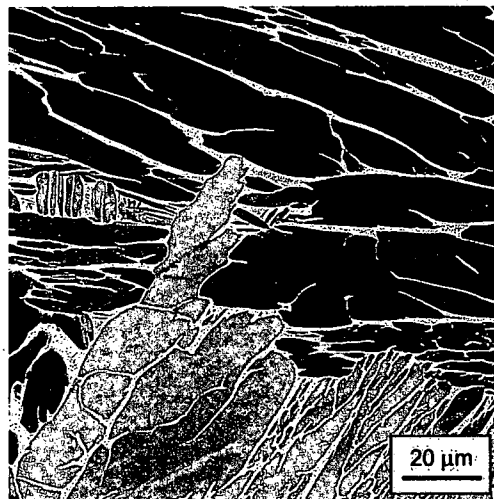


(b)

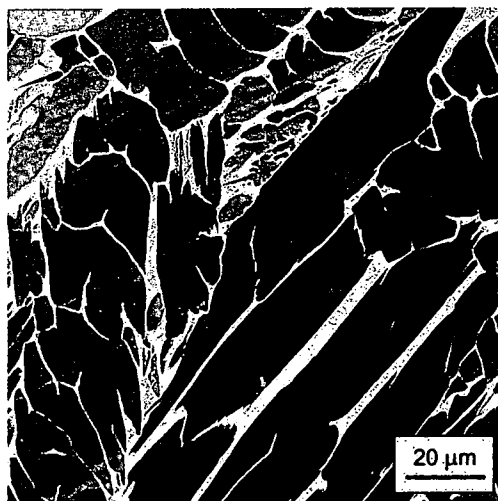
Figure 94. Microstructures of post-thermal analysis XB3043 alloy sample, trial 2. Images were taken at center (a) and edge (b) locations.



(a)

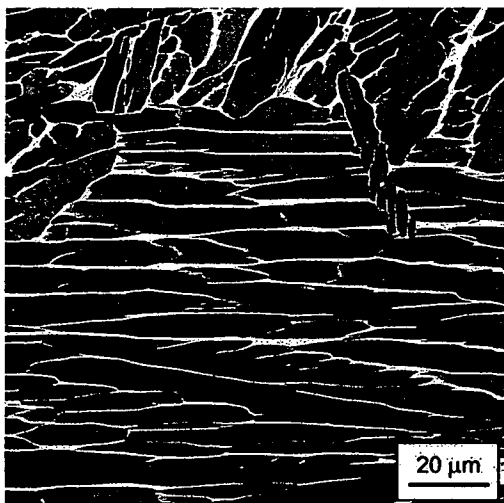


(b)

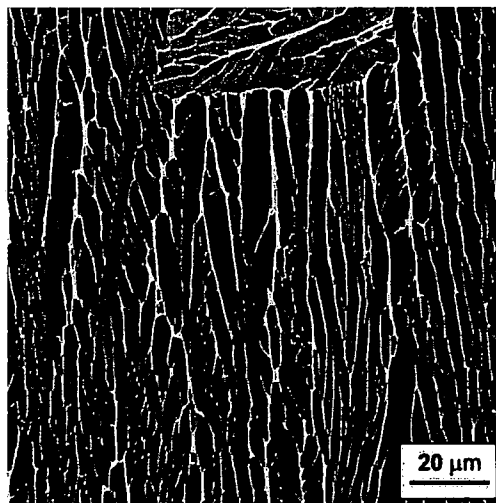


(c)

Figure 95. Microstructures of as-received (a) and post-thermal analysis (b, c) samples of alloy XB3045. Images were taken at center (b) and edge (c) locations for trial 1.

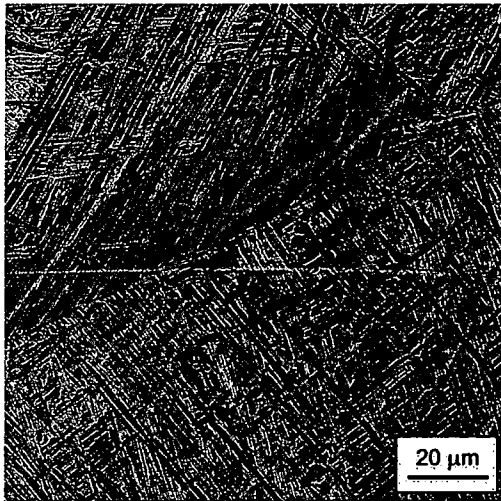


(a)

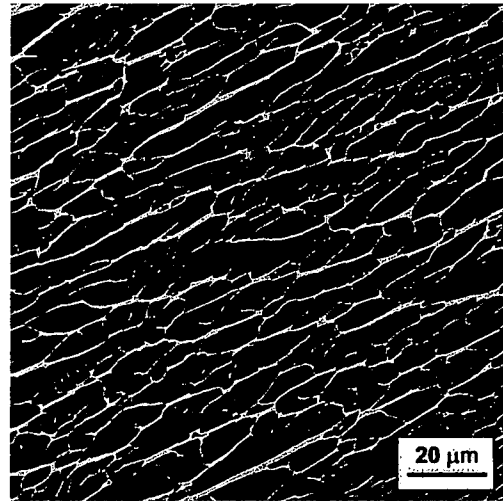


(b)

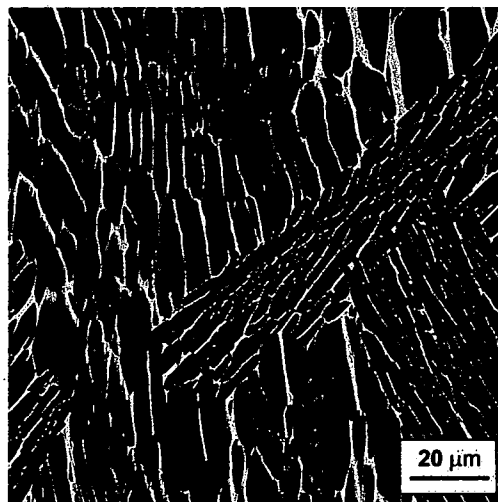
Figure 96. Microstructures of post-thermal analysis XB3045 alloy sample, trial 3. Images were taken at center (a) and edge (b) locations.



(a)

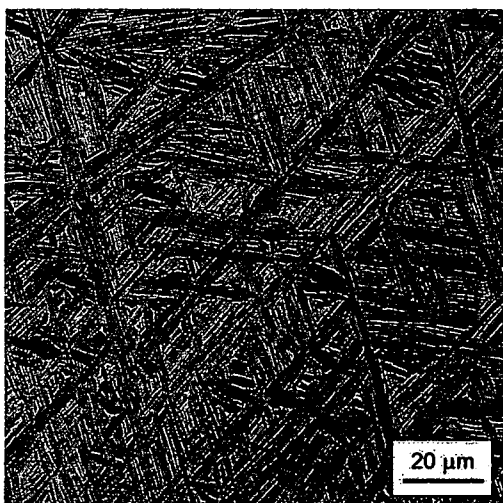


(b)

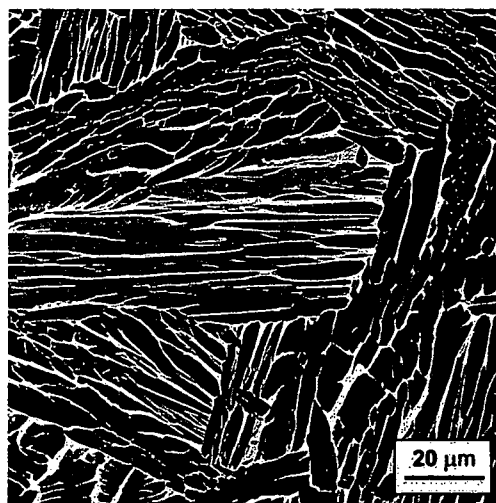


(c)

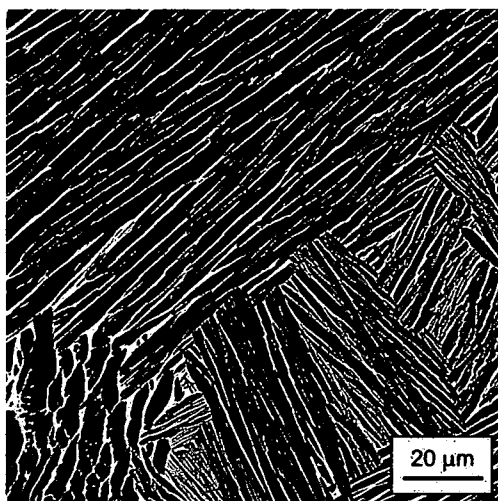
Figure 97. Microstructures of as-received (a) and post-thermal analysis (b, c) samples of alloy XB3048. Images were taken at center (b) and edge (c) locations for trial 4.



(a)



(b)



(c)

Figure 98. Microstructures of as-received (a) and post-thermal analysis (b, c) samples of alloy XB3049. Images were taken at center (b) and edge (c) locations for trial 5.

APPENDIX F

ELECTRON PROBE MICROANALYSIS

Table 9. Results of electron probe microanalysis of selected post-thermal analysis samples.

Sample ID	Al	Ti	V	Fe	Y
XB3040-4	4.48	91.89	3.57	0.00	0.06
XB3041-1	5.35	90.43	4.15	0.00	0.06
XB3041-2	5.54	89.83	4.54	0.02	0.07
XB3043-1	5.31	88.78	4.39	0.13	1.39
XB3043-2	5.25	90.33	4.24	0.10	0.08
XB3045-1	5.15	89.98	4.40	0.39	0.08
XB3045-2	5.68	90.57	3.53	0.16	0.06
XB3045-3	5.22	90.29	4.19	0.22	0.09
XB3048-4	5.02	90.37	4.09	0.40	0.11
XB3049-5	4.97	90.50	4.06	0.40	0.08

APPENDIX G

MICROINDENTATION HARDNESS MEASUREMENTS

Table 10. Results of microindentation testing on as-received and post-thermal analysis samples.

Sample ID	HK
Base AR	318.63
Base-3	351.14
Base-6	392.70
Base-7	402.11
XB3040 AR	298.88
XB3040-4	334.76
XB3041 AR	293.98
XB3041-1	360.77
XB3041-2	393.56
XB3043 AR	319.21
XB3043-1	405.99
XB3043-2	359.69
XB3045 AR	311.92
XB3045-1	394.08
XB3045-2	348.82
XB3045-3	411.18
XB3048 AR	316.06
XB3048-4	394.36
XB3048 AR	345.74
XB3049-5	420.23

APPENDIX H

INITIAL THERMODYNAMIC CALCULATIONS

Table 11. Results of initial thermodynamic calculations for the Ti-6Al-4V alloys [44].

Sample ID	Iron Content (wt pct)	Oxygen Content (wt pct)	Liquidus Temperature (°C)	Solidus Temperature (°C)	Freezing Range, ΔT_{L-S} (°C)
Baseline	0.15	0.2470	1719.0	1656.0	63.0
XB3040	0.02	0.1010	1715.0	1672.0	43.0
XB3041	0.02	0.1900	1719.5	1683.5	36.0
XB3043	0.10	0.2000	1718.0	1686.0	32.0
XB3045	0.22	0.1830	1714.5	1682.0	32.5
XB3048	0.44	0.0980	1709.5	1664.0	45.5
XB3049	0.44	0.2490	1715.0	1660.0	55.0
XB3042	0.09	0.0957	1714.0	1684.0	30.0
XB3044	0.21	0.0965	1711.0	1673.5	37.5
XB3046	0.33	0.0885	1709.0	1672.0	37.0
XB3047	0.32	0.1830	1715.5	1672.5	43.0

APPENDIX I

SEGREGATION MODELING

Table 12. Input parameters for segregation calculations for Ti-6Al-4V ingot slab "C" using the LSRE.

Parameter	Value
C_{0Al}	6.100
C_{0V}	3.740
C_{0Fe}	0.200
C_{0O}	0.229
ρ_s (kg/m ³)	4165.13
ρ_L (kg/m ³)	3899.6
μ (N s/m ²)	0.00325
ΔP (atm)	0.1
g_L	0.0 - 1.0
d_1 (m)	0.000778
g_r (m/s ²)	9.8
G (K/m)	225
ε (K/s)	30
Δx (m)	0.01

APPENDIX J

ADDITIONAL SENSITIVITY ANALYSIS PLOTS

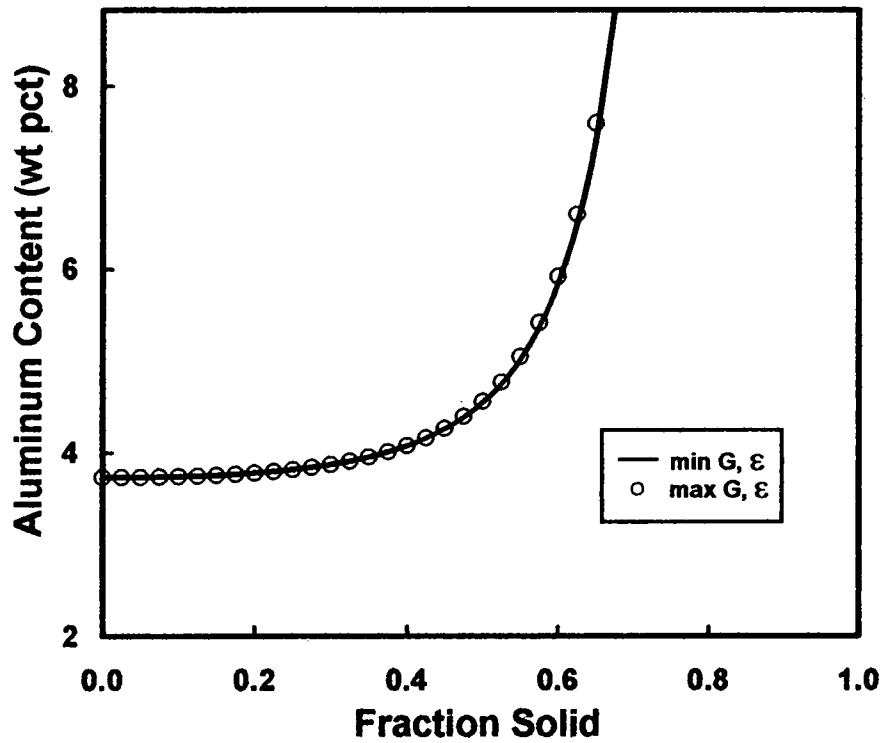


Figure 99. Predicted aluminum segregation, from the LSRE, using varied temperature gradients (G) and cooling rates (ϵ) for conditions of a fully columnar float-zone directionally-solidified casting.

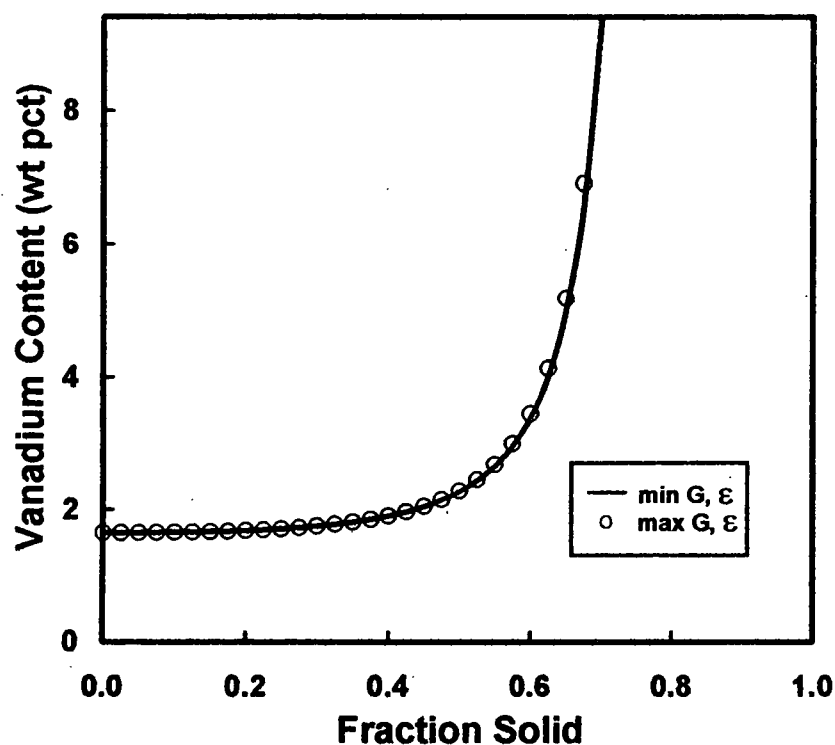


Figure 100. Predicted vanadium segregation, from the LSRE, using varied temperature gradients (G) and cooling rates (ϵ) for conditions of a fully columnar float-zone directionally-solidified casting.

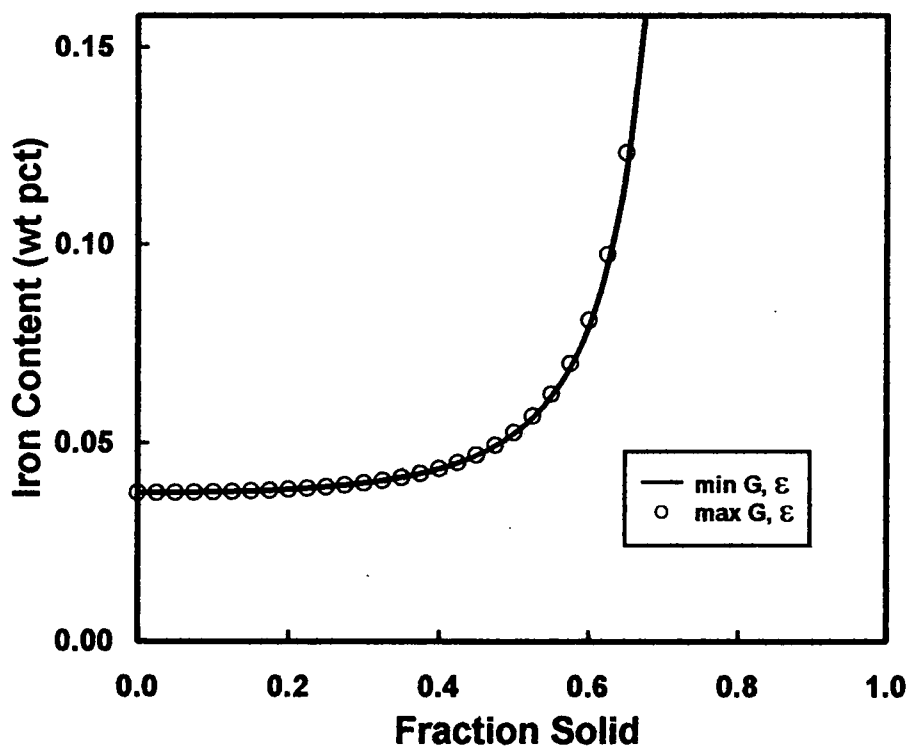


Figure 101. Predicted iron segregation, from the LSRE, using varied temperature gradients (G) and cooling rates (ϵ) for conditions of a fully columnar float-zone directionally-solidified casting.

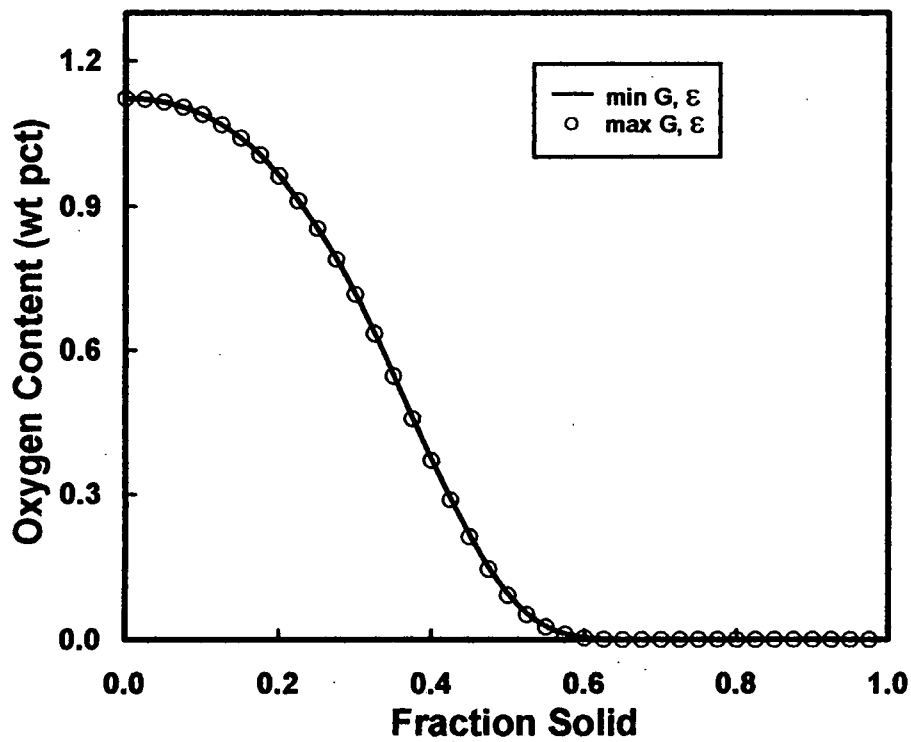


Figure 102. Predicted oxygen segregation, from the LSRE, using varied temperature gradients (G) and cooling rates (ϵ) for conditions of a fully columnar float-zone directionally-solidified casting.

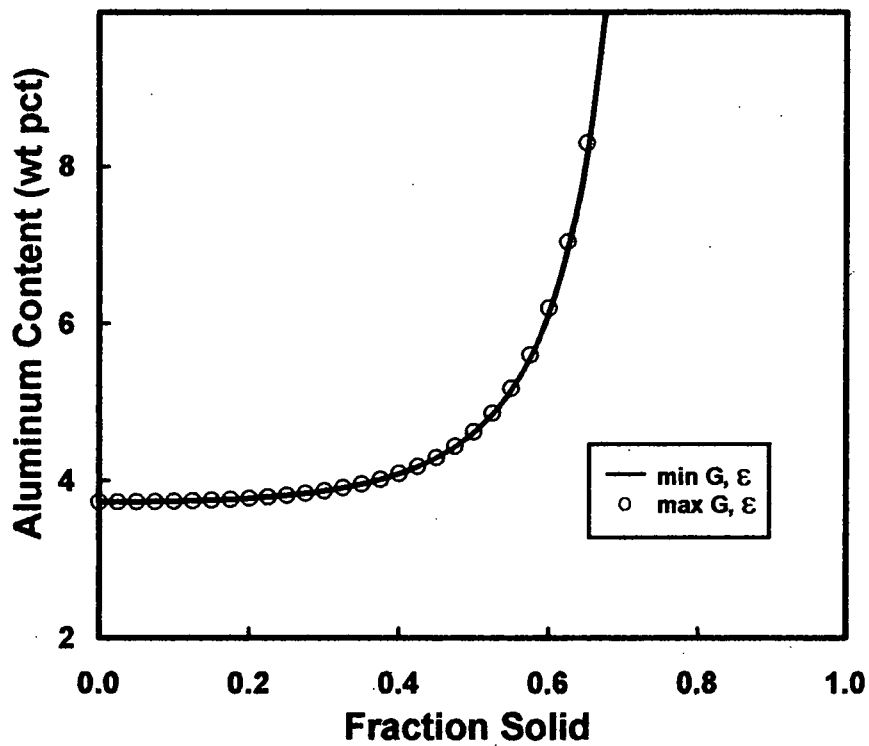


Figure 103. Predicted aluminum segregation, from the LSRE, using varied temperature gradients (G) and cooling rates (ϵ) for conditions of a fully equiaxed cylindrical casting.

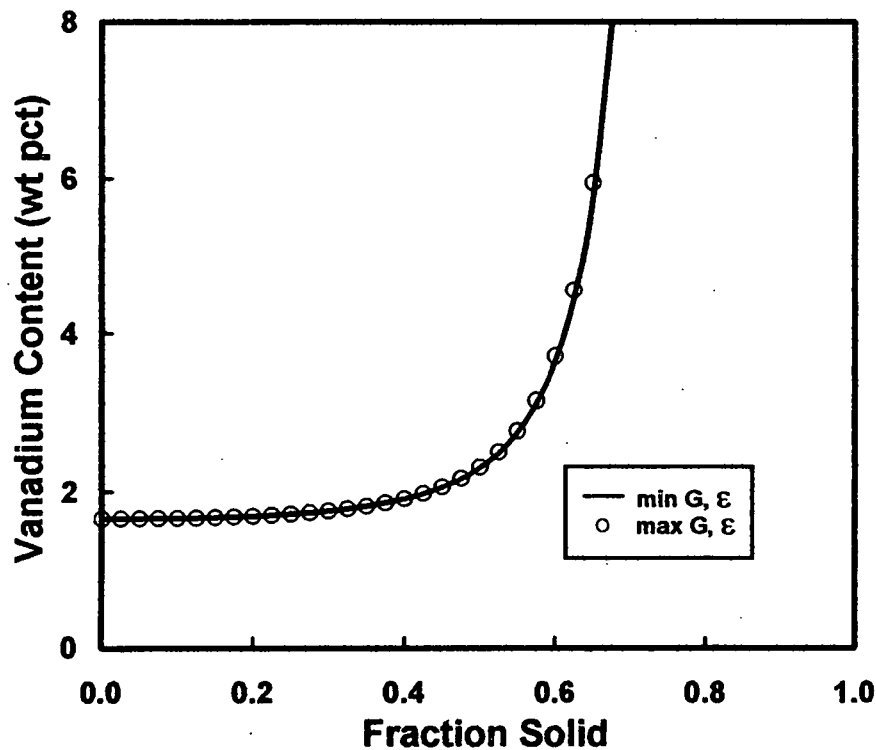


Figure 104. Predicted vanadium segregation, from the LSRE, using varied temperature gradients (G) and cooling rates (ϵ) for conditions of a fully equiaxed cylindrical casting.

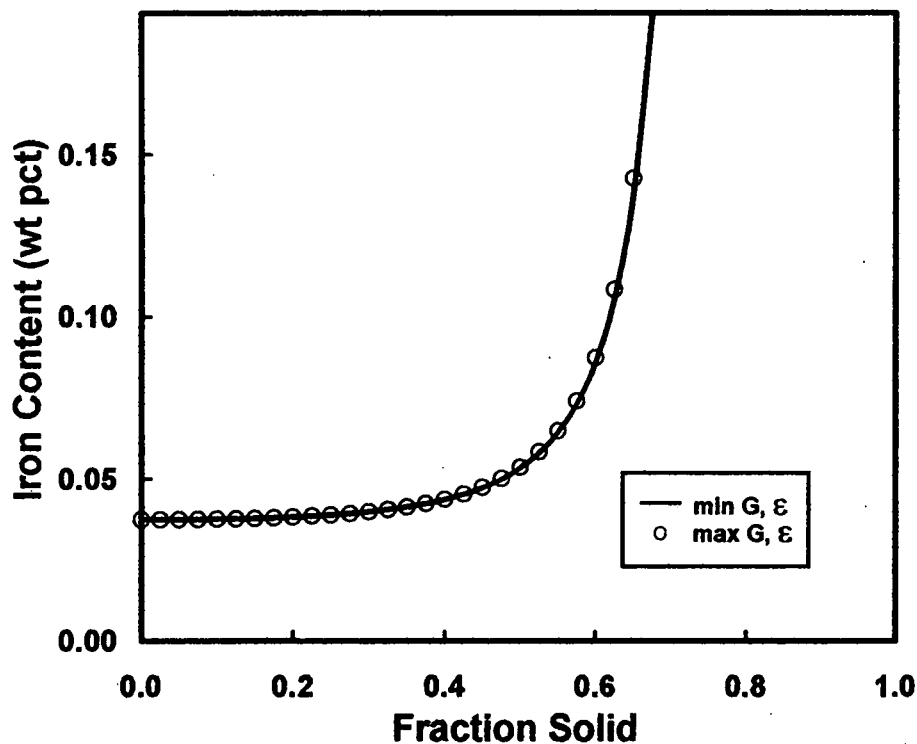


Figure 105. Predicted iron segregation, from the LSRE, using varied temperature gradients (G) and cooling rates (ϵ) for conditions of a fully equiaxed cylindrical casting.

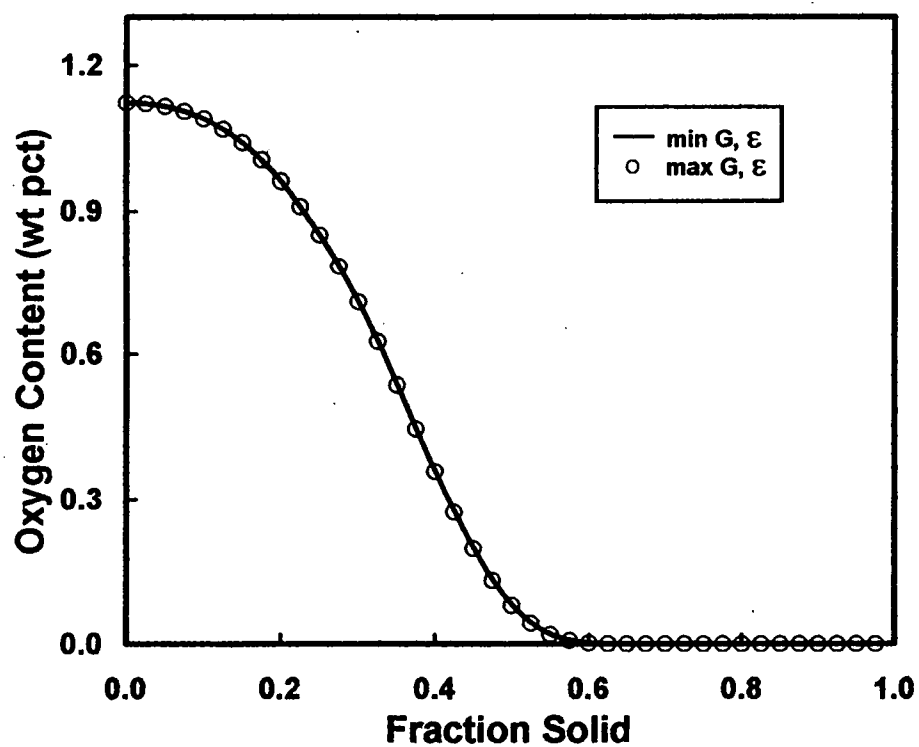


Figure 106. Predicted oxygen segregation, from the LSRE, using varied temperature gradients (G) and cooling rates (ϵ) for conditions of a fully equiaxed cylindrical casting.

REFERENCES

1. Beckermann, C., "Macrosegregation," Encyclopedia of Materials: Science and Technology, Elsevier Science, Ltd., 4733-4739, 2001.
2. Beckermann, C., "Modelling of Macrosegregation: Applications and Future Needs," *International Materials Reviews*, 47 (5): 243-261.
3. Zhang, B., J. Cui, and G. Lu, "Effect of Low-Frequency Magnetic Field on Macrosegregation of Continuous Casting Aluminum Alloys," *Materials Letters*, 57 (11): 1707-1711, 2003.
4. Khare, A.K., Committee Chairman, "Open-Die Forging," Metals Handbook, Ninth Edition, 14: 61-74, 1988.
5. RMI Titanium Company, "Titanium Alloy Guide," 2000.
6. Newman, J.R., D. Eylon, and J.K. Thome. "Titanium and Titanium Alloys," ASM Handbook, 15: p. 824-835, 1998.
7. Reynolds, J.E. and R.I. Jaffee, "The Diffusion of Interstitial and Substitutional Elements in Titanium," *Titanium Metallurgical Laboratory Report No. 21*, Battelle Memorial Institute, Columbus, Ohio, 1955.
8. Seagle, S.R., "The State of the USA Titanium Industry in 1995," *Materials Science and Engineering*, A213: 1-7, 1996.
9. Seagle, S.R. and P.A. Russo, "Principles of Alloying Titanium," A Lesson from Titanium and its Alloys, ASM-MEI Course 27, Lesson 3, ASM International, Metals Park, Ohio, p. 1,21, 1994.
10. Seagle, S.R. K.O. Yu, and S. Giangiordano, "Considerations in Processing Titanium," *Materials Science and Engineering*, A263: p. 237-242, 1999.
11. Semiatin, S.L., V. Seetharaman, and I. Weiss, "Hot Working of Titanium Alloys – An Overview," Advances in the Science and Technology of Titanium Alloy Processing, The Minerals, Metals and Materials Society, p. 4, 1997.
12. Wood, R.A. and E. Poulsen, "History and Extractive Metallurgy," A Lesson from Titanium and its Alloys, ASM-MEI Course 27, Lesson 1, ASM International, Metals Park, Ohio, p. 9, 1994.
13. Donachie Jr., M.J., ed., Titanium: A Technical Guide, Second Edition, ASM International, Materials Park Ohio, p. 25, 28, 2000.
14. Kurz, W. and D.J. Fisher, Fundamentals of Solidification, Fourth Revised Edition, Trans Tech Publications, Inc., New Hampshire, p. 21-22, 1998.
15. ASM, Solidification, p. 328, 1971.

16. Flemings, M.C., Solidification Processing. McGraw-Hill, Inc. New York, 1974.
17. Porter, D.A. and K.E. Easterling, Phase Transformations in Metals and Alloys, Second Edition, Chapman & Hall, New York, p. 185-198, 1992.
18. Bomberger, H.B. and F.H. Froes, "Solidification and Phase Diagrams," A Lesson from Titanium and its Alloys, ASM-MEI Course 27, Lesson 2, ASM International, Metals Park, Ohio, p. 3, 1994.
19. Ghosh, A. "Segregation in Cast Products," *Sādhanā*, 26 (1&2): 5-24, 2001.
20. Flemings, M.C. "Our Understanding of Macrosegregation: Past and Present," *ISIJ International*, 40 (9): 833-841, 2000.
21. Boettinger, W.J. "Solidification Structures of Solid Solutions." ASM Handbook, Volume 9: 611-617, 2000.
22. Fujii, T., D. R. Poirier, and M.C. Flemings. "Macrosegregation in a Multicomponent Low Alloy Steel," *Metallurgical Transactions B*, 10B: 331-339, 1979.
23. Ridder, S.D., S. Kou, and R. Mehrabian. "Effect of Fluid Flow on Macrosegregation in Axi-Symmetric Ingots," *Metallurgical Transactions B*, 12B: 435-447, 1981.
24. Hills, R.N., D.E. Loper, and P.H. Roberts. "A Thermodynamically Consistent Model of a Mushy Zone," *Q. J. Mech. Appl. Math*, 36 (4): 505-539.
25. Ganesan, S. and D.R. Poirier. "Conservation of Mass and Momentum for the Flow of Interdendritic Liquid during Solidification," *Metallurgical Transactions B*, 21B: 173-181, 1990.
26. Beckermann, C. and C.Y. Wang. "Multi-Phase/-Scale Modeling of Transport Phenomena in Alloy Solidification," Annual Review of Heat Transfer VI, ed. C.L. Tien, Begell House, New York, NY, Vol. 6, p. 115-198, 1995.
27. Poirier, D.R. and J.C. Heinrich. "Continuum Model for Predicting Macrosegregation in Dendritic Alloys," *Materials Characterization*, 32 (4): p. 287-298, 1994.
28. Schneider, M.C. and C. Beckermann. "A Numerical Study of the Combined Effects of Microsegregation, Mushy Zone Permeability and Flow, Caused by Volume Contraction and Thermosolutal Convection, on Macrosegregation and Eutectic Formation in Binary Alloy Solidification," *International Journal of Heat and Mass Transfer*, 38 (18): p.3455-3473, 1995.
29. Sung, P.K., D.R. Poirier, and S.D. Felicelli. "Sensitivity of Mesh Spacing on Simulating Macrosegregation during Directional Solidification of a Superalloy," *International Journal for Numerical Methods in Fluids*, 35: p. 357-370, 2001.

30. Frueh, C., D.R. Poirier, and S.D. Felicelli. "Effect of Computational Domain Size on the Mathematical Modeling of Transport Processes and Segregation during Directional Solidification," *Metallurgical and Materials Transactions A*, 31A: p. 3129-3135, 2000.
31. Felicelli, S.D., D.R. Poirier, and P.K. Sung. "A Model for Prediction of Pressure and Redistribution in Multicomponent Casting Alloys," *Metallurgical and Materials Transactions B*, 31B: p. 1283-1292, 2000.
32. Vreeman, C.J, M.J.M. Krane, and F.P. Incropera. "The Effect of Free-Floating Dendrites and Convection on Macrosegregation in Direct Chill Cast Aluminum Alloys, Part I: Model Development," *International Journal of Heat and Mass Transfer*, 43: p. 677-686, 2000.
33. Krane, M.J.M. "Macrosegregation Development during Solidification of a Multicomponent Alloy with Free-Floating Solid Particles," *Applied Mathematical Modelling*, 28: p. 95-107, 2004.
34. Wilson, A.F., A. Jardy, J. Hammel, S.P. Fox, and D. Ablitzer. "Implementation and Utilisation [sic] of a Mathematical Model to Simulate Vacuum Arc Remelting of Titanium Alloys," *Proceedings for the World Conference on Titanium*, 2003.
35. Baker, H. "Introduction to Alloy Phase Diagrams," *ASM Handbook*, 3: 1.1-1.30, 1999.
36. Chen, S.-L., F. Zhang, S. Daniel, F.-Y. Xie, X.-Y. Yan, Y.A. Chang, R. Schmid-Fetzer, and W.A. Oates. "Calculating Phase Diagrams Using PANDAT and PanEngine," *JOM*, 2003, p. 48-51.
37. Yan, X., L. Ding, S. Chen, F. Xie, M. Chu, and Y.A. Chang. "Predicting Microstructure and Microsegregation in Multicomponent Alloys," *Light Metals 2001*, ed. J.L. Anjier, TMS, p. 1091-1097, 2001.
38. Speyer, R.F. *Thermal Analysis of Materials*, Marcel Dekker, Inc., New York, p. 1, 35-39, 1994.
39. Hatakeyama, T. and F.X. Quinn. *Thermal Analysis, Fundamentals and Applications to Polymer Science*, Second Edition, John Wiley and Sons, Ltd., New York, 1999.
40. Wu, R.I. and J.H. Perepezko. "Liquidus Temperature Determination in Multicomponent Alloys by Thermal Analysis," *Metallurgical and Materials Transactions A*, 31A: p. 497-501, 2000.
41. Personal communication with J.H. Perepezko, Department of Materials Science and Engineering, The University of Wisconsin at Madison, March 16, 2005.
42. Internet: Central Michigan University, Department of Geology, Electron Microscope Facility (<http://www.cst.cmich.edu/units/gel/probe/whtcndo.htm>), September 25, 2003.

43. Chandler, H., ed. Hardness Testing, Second Edition, ASM International, Metals Park, Ohio, p. 39-41, 53-59, 63-87, 1999.
44. Xie, F.-Y., PanTitanium User Manual, Version 1. CompuTherm LLC, Madison, WI; 2004.
45. Kobryn, P.A. "The Effect of Interface Heat Transfer on Solidification, Microstructure Evolution, and Mold Wear in Permanent Mold Casting of Ti-6Al-4V," Ph.D. Thesis, OSU, Cols., OH, 1999.
46. Akhonin, S.V., N.P. Trigub, V.N. Zamkov, and S.L. Semiatin. "Mathematical Modeling of Aluminum Evaporation During Electron-Beam Cold-Hearth Melting of Ti-6Al-4V Ingots," *Metallurgical and Materials Transactions B*, 34B: p. 447-454, 2003.
47. Flemings, M.C. and G.E. Nereo, "Macrosegregation: Part I," *Transactions of the Metallurgical Society of AIME*. 239, p. 1449-1461, 1967.
48. Poirier, D.R., "Permeability for Flow of Interdendritic Liquid in Columnar-Dendritic Alloys," *Metallurgical Transactions B*. 18B, p. 245-255, 1987.
49. Murray, J.L., "Al-Ti (Aluminum-Titanium)," Binary Alloy Phase Diagrams (Second Edition), 1: 225-227, 1990.
50. Murray, J.L., "Ti-V (Titanium-Vanadium)," Binary Alloy Phase Diagrams (Second Edition), 3: 3494-3495, 1990.
51. Murray, J.L., ed., "The Fe-Ti (Iron-Titanium) System," Phase Diagrams of Binary Titanium Alloys, ASM International, Ohio, p. 100, 1987.
52. Schofield, T.H. and A.E. Bacon, "The Constitution of the Titanium-Oxygen Alloys in the Range 0-35 Weight Per Cent. Oxygen," *Journal of the Institute of Metals*. 84 (2): p. 47-53, 1955.
53. Mills, K.C., Recommended Values of Thermophysical Properties for Selected Commercial Alloys, ASM International, Ohio, 2002.
54. Brooks, R.F, A.P. Day, K.C. Mills, and P.N. Quested, "Physical Property Measurements for the Mathematical Modeling of Fluid Flow in Solidification Processes," *International Journal of Thermophysics*. 18 (2), p. 471-480.
55. Poirier, D.R. and P.K. Sung, unpublished research, 2005.
56. Personal communication with D.R. Poirier, Department of Materials Science and Engineering, The University of Arizona, February 14, 2005.
57. Sung, P.K., R.G. Erdmann, and D.R. Poirier, unpublished research, 2004.

58. Kobryn, P.A. and S.L. Semiatin, "Microstructure and Texture Evolution During Solidification Processing of Ti-6Al-4V," *Journal of Materials Processing Technology*, 135, p. 330-339, 2003.
59. Choudhury, A. and E. Weingärtner, "Vacuum Arc Remelting (VAR)," ASM Handbook, 15: 406-410, 1998.
60. ALD Vacuum Technologies, Inc. "Vacuum Arc Remelting (VAR)," (http://www.ald-vt.com/home/pdf/var_eng.pdf) June 16, 2004.
61. Dietrich, W. and H. Stephan, "Electron Beam Melting and Casting," ASM Handbook, 15: 410 - 419, 1992.
62. Sims, C.T. and W.C. Hagel, eds., The Superalloys, John Wiley and Sons, Inc. New York, p. 392, 1972.
63. Shamblen, C.E. and A.P. Woodfield, "Progress in Titanium-Alloy Hearth Melting," *Industrial Heating*, p. 49-52, January 2004.
64. Pannen, H. and G. Sick, "Plasma Melting and Casting," ASM Handbook, 15: 419 - 425, 1998.
65. Internet: IRC in Materials Processing (<http://www.irc.bham.ac.uk/theme1/plasma/furnace.htm>), March 10, 2004.
66. Harding, R.A. and M. Wickins. "Temperature Measurements during Induction Skull Melting of Titanium Aluminide," *Materials Science and Technology*, 19: 1235-1246, 2003.
67. Reed, S. and J. Narayan. "Investment Casting of Titanium Using the Induction Skull Melting Process," *Aluminum International Today*, 16 (3): F1& - F18, 2004.
68. Personal Communication with K.O. Yu of RMI Titanium Company, November 2, 2005.
69. Horton, R.A. "Investment Casting," ASM Handbook, 15: 253 - 269, 1998.
70. Personal communication with D.R. Barker of U.E.S., Inc., February 25, 2004.

R002592376

HECKMAN

BINDERY, INC

T 022382 F 7 00



1/5/2006

VITA

January 10, 1981	Born- Dayton, Ohio
2003	B.S. Chemical Engineering University of Dayton
2005	M.S. Chemical Engineering University of Dayton

PUBLICATIONS

S.L. Semiatin, S.L. Knisley, P.N. Fagin, F. Zhang, and D.R. Barker,
"Microstructure Evolution during Alpha-Beta Heat Treatment of Ti-6Al-4V," Metallurgical
and Materials Transactions A, Vol. 34A, p. 2377 (2003).